Eur. Phys. J. A **26**, 441–478 (2005)
DOI 10.1140/epja/i2005-10173-4

THE EUROPEAN PHYSICAL JOURNAL A

Reactions with fast radioactive beams of neutron-rich nuclei

T. Aumann[a]

Gesellschaft für Schwerionenforschung mbH (GSI), Planckstraße 1, D-64291 Darmstadt, Germany

Received: 22 June 2005 / Revised version: 7 November 2005 /
Published online: 12 January 2006 –
Communicated by R. Krücken

Abstract. The neutron dripline has presently been reached only for the lightest nuclei up to the element oxygen. In this region of light neutron-rich nuclei, scattering experiments are feasible even for dripline nuclei by utilizing high-energy secondary beams produced by fragmentation. In the present article, reactions of high-energy radioactive beams will be exemplified using recent experimental results mainly derived from measurements of breakup reactions performed at the LAND and FRS facilities at GSI and at the S800 spectrometer at the NSCL. Nuclear and electromagnetically induced reactions allow probing different aspects of nuclear structure at the limits of stability related to the neutron-proton asymmetry and the weak binding close to the dripline. Properties of the valence-neutron wave functions are studied in the one-neutron knockout reaction, revealing the changes of shell structure when going from the beta-stability line to more asymmetric loosely bound neutron-rich systems. The vanishing of the $N = 8$ shell gap for neutron-rich systems like ^{11}Li and ^{12}Be, or the new closed $N = 14, 16$ shells for the oxygen isotopes are examples. The continuum of weakly bound nuclei and halo states can be studied by inelastic scattering. The dipole response, for instance, is found to change dramatically when going away from the valley of stability. A redistribution of the dipole strength towards lower excitation energies is observed for neutron-rich nuclei, which partly might be due to a new collective excitation mode related to the neutron-proton asymmetry. Halo nuclei, in particular, show strong dipole transitions to the continuum at the threshold, being directly related to the ground-state properties of the projectile. Finally, an outlook on future experimental prospects is given.

PACS. 25.60.-t Reactions induced by unstable nuclei – 24.50.+g Direct reactions – 24.30.-v Resonance reactions – 21.10.Jx Spectroscopic factors

1 Introduction

The investigation of nuclei near the driplines via scattering experiments at intermediate and high energies has attracted significant interest in the past decade due to the availability of fast radioactive beams produced by fragmentation [1]. Such relatively high beam energies (ranging from about 50 MeV/nucleon to 1 GeV/nucleon) are advantageous both from an experimental point of view as well as from theoretical considerations. The high beam energies result in short interaction times and small scattering angles, which allow the use of certain approximations and thus enable a quantitative description of the underlying reaction mechanisms. Experimental merits are the possibility of using relatively thick targets (in the order of g/cm^2) and kinematical forward focussing, which makes full-acceptance measurements feasible with moderately sized detectors. Thus nuclear-structure investigations of very exotic nuclei at the driplines are possible even if such beams are produced with very low rates in the order of one ion per second.

The story of reactions with relativistic radioactive beams started more than two decades ago with the first production and identification of radioactive beams by fragmentation of ^{40}Ar and ^{48}Ca primary beams with around 200 MeV/nucleon kinetic energy at the Bevalac in Berkeley [2,3]. The first results from scattering experiments using secondary beams of neutron-rich He and Li isotopes produced by fragmentation of 800 MeV/nucleon ^{11}B and ^{20}Ne projectiles were obtained by Tanihata *et al.* in 1985 [4–6]. They measured total interaction cross-sections by a transmission method from which they deduced the radii of the isotopes, see fig. 1. A strong increase of the radii with neutron excess is observed, much stronger than expected from the $A^{1/3}$-dependence known for stable nuclei. The sharp increase of the radii for some isotopes compared to its near neighbors, *e.g.*, for ^{11}Be and ^{11}Li, is explained by a low-density tail of the valence-neutron(s) wave function, called nuclear halo [7]. Meanwhile, several such light halo nuclei were observed at the

[a] e-mail: t.aumann@gsi.de

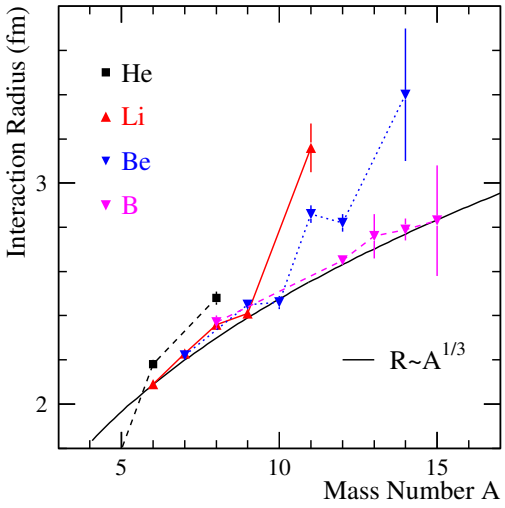

Fig. 1. Neutron halo at the dripline. Radii deduced from measurements of total interaction cross-sections [6].

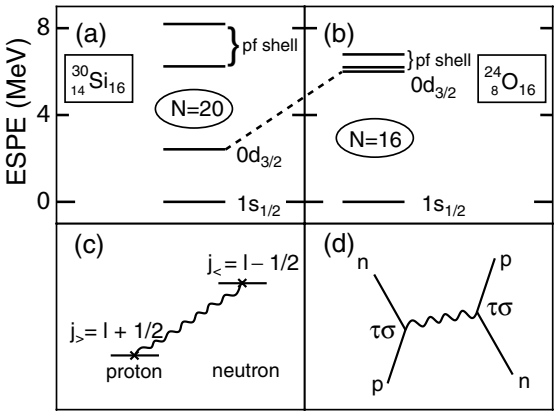

Fig. 2. Change of shell gaps and single-particle relative energies for $N = 16$ nuclei comparing stable (^{30}Si) and dripline (^{24}O) nuclei. Reprinted with permission from Otsuka *et al.* [26]. Copyright (2001) by the American Physical Society.

neutron dripline, see the review articles [8–17] for a detailed discussion. An overview on measurements of interaction cross-sections and extracted radii can be found in the article by Ozawa *et al.* [18]. The conclusion that the large radii are indeed related to an extended neutron density distribution was confirmed by measurements of the quadrupole moments [19] and the charge-changing cross-sections [20] for the Li isotopes: both are similar for the two isotopes ^{9}Li and ^{11}Li, while the interaction cross-section increases by about 30%. Such an extended matter distribution for weakly bound nuclei was also found and confirmed in proton elastic-scattering experiments for He and Li isotopes [21,22]. The occurrence of halo states is predicted theoretically also for heavier nuclei [23,24]. If low-angular-momentum states are filled with neutrons being weakly bound, halo structures involving many neutrons might develop [23,24].

A halo-like low-density tail of the neutron wave function, as discussed above, has a definite impact on the observables in breakup reactions. These are, for example, the large cross-sections and narrow momentum distributions observed in the nuclear one-neutron removal channel, see sect. 3.3, and most striking in the Coulomb breakup reaction leading to huge dipole transition strength at the threshold directly related to the spatial extension of the wave function, see sect. 3.3.4.

Recently, reactions such as the one-neutron removal channel in nuclear or electromagnetic scattering of high-energy beams were developed towards being a quantitative tool to study the single-particle properties of unstable nuclei. Similar to transfer reactions, established at lower beam energies as a spectroscopic tool for stable nuclei [25], spectroscopic factors and angular-momentum assignments can be obtained. One important aspect of radioactive beam physics which can be addressed by these reactions is the evolution of the shell structure when going to largely proton-neutron asymmetric and weakly bound nuclei. As already observed experimentally, the shell closures known for stable nuclei might disappear when going away from the valley of β-stability, and new shell closures might appear. An example, which will be discussed in sect. 3 is the vanishing of the $N = 8$ closed neutron shell at the dripline. Another is the appearance of new sub-shell closures at $N = 14$ and $N = 16$ for the neutron-rich oxygen isotopes [27,28,26,29–32] rather than at $N = 20$, which is a closed shell for stable nuclei. A change of shell closures as a function of isospin might have several origins: one is the change of the mean field, being more dilute for neutron-rich nuclei, and thus leading to a reduced spin-orbit splitting [33,34]. From such an effect, a rearrangement of single-particle levels towards a harmonic-oscillator–like ordering could be expected [34]. Another effect discussed by, *e.g.*, Otsuka *et al.* [26] is related to the properties of the nucleon-nucleon interaction. Here, in particular, the attractive spin-isospin flip part $V_{\sigma\tau}$ of the interaction changes when adding or removing nucleons. For the case of the $N = 16$ neutron shell discussed, it is the emptying of the $d_{5/2}$ proton level when moving from ^{30}Si to the neutron-rich oxygen isotope ^{24}O which causes the change in the relative energies of the single-particle levels, as illustrated in fig. 2. The lack of the attractive interaction of the $d_{3/2}$ neutrons with the $d_{5/2}$ protons pushes the $d_{3/2}$ level up causing a shell gap for neutron number $N = 16$ [26,35].

The successful development of the methods involving reactions with high-energy secondary beams as a quantitative tool to extract nuclear-structure observables for short-lived nuclei was possible not only due to the tremendous experimental improvements in the past years but also due to the development of the associated reaction theory. Here, we refer the reader to recent review articles giving an overview on the relevant theories [36–39].

The second class of reactions discussed in the present paper (sect. 4) deals with the multipole response of exotic nuclei studied by inelastic scattering of high-energy secondary beams. The question here is how the excitation spectra change for weakly bound nuclei with asymmetric proton-to-neutron ratios, which causes a separation of neutrons and protons energy-wise due to the filling of different single-particle orbits, but also spatially (halos and

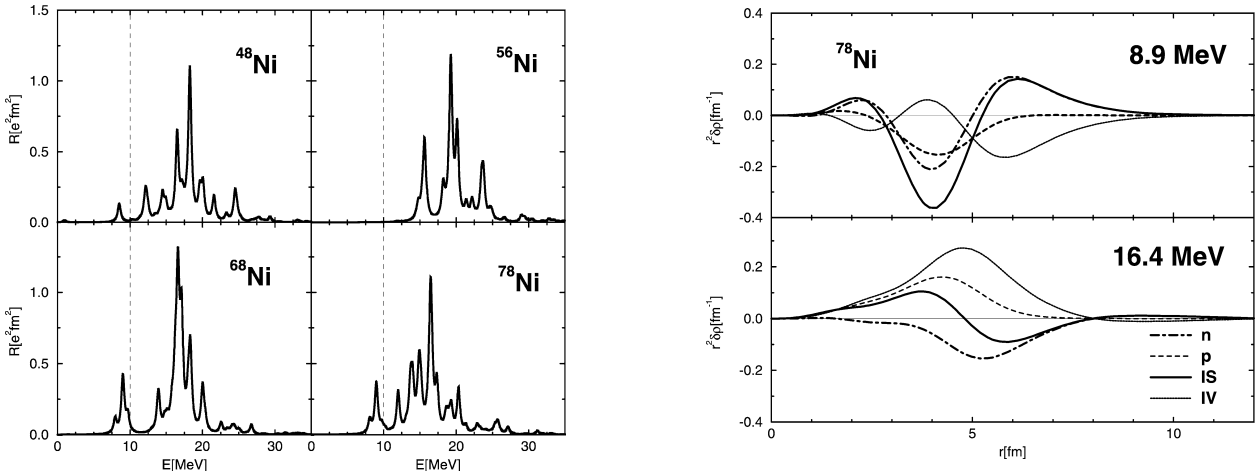

Fig. 3. Strength functions (left) and transition densities (right) resulting from relativistic mean-field calculations [40] for dipole transitions in Ni isotopes. The transition densities are shown separately for the GDR region (lower right frame) and for the low-lying resonance around 9 MeV (upper right panel). Reprinted from Vretenar *et al.* [40], Copyright (2001), with permission from Elsevier.

neutron skins). A decoupling of the more weakly bound valence neutrons should manifest itself in the excitation spectra, and new collective excitation modes are expected. For stable nuclei, the continuum response is dominated by the various giant resonances. Giant resonances are collective nuclear excitation modes exhausting a large fraction of the respective sum rules. Microscopically, they are understood as a coherent superposition of many particle-hole states across one or two major shells. The isovector giant dipole resonance (GDR) was the first discovered experimentally, about 50 years ago, and has been interpreted as the collective vibration of neutrons against protons. Systematic studies involving almost all stable nuclei available as target material yielded a large data basis and have shown that nearly the complete dipole strength given by the classical energy-weighted Thomas-Reiche-Kuhn (TRK) dipole sum rule is absorbed into this excitation mode. The ultimate proof of the vibrational character of the GDR, however, came only recently with the observation of the second phonon state [41], demonstrating that the GDR is essentially a harmonic vibration. With the advent of radioactive beams, the possibility of giant-resonance studies with unstable nuclei came into reach. Again, it is the GDR which is studied first, also due to experimental reasons.

The question of how the multipole strength functions evolve when going away from stable nuclei, towards unstable nuclei with large neutron or proton excess has been studied theoretically in the past few years by various approaches, see, *e.g.*, [40,42–51]. Concerning the dipole-strength function, a stronger fragmentation of the strength, in particular a redistribution of the strength towards lower excitation energies, has been predicted consistently by calculations of different kind. Experimentally, such a redistribution of strength was observed recently at GSI for the oxygen isotope chain [52], as will be discussed in sect. 4.1. Dipole excitations are most effectively studied using the electromagnetic excitation process at high energy, yielding rather large cross-sections. In principle, also magnetic dipole and quadrupole excitations can be investigated, the cross-sections being, however, much smaller. A precise angular distribution and/or beam-energy dependence has to be measured with good statistics in order to disentangle such contributions from the dominant dipole excitations.

The study of the dipole-strength function for exotic nuclei has different aspects. Giant-resonance parameters were used in the past for stable nuclei to determine effective interactions used in the mean-field calculations. As pointed out by Reinhard [44], the predicted giant-resonance strength in exotic nuclei is particularly sensitive to the isospin- and density-dependent parts of the effective interaction, which are not well determined from studies with stable nuclei. In turn, the measurement of the strength functions for exotic nuclei might help constraining such effective forces. Another aspect is the appearance of new coherent modes, *e.g.*, the collective dipole vibration of excess neutrons against the core for neutron-rich nuclei. Such a soft-dipole mode was predicted by various calculations; fig. 3 shows as an example the results of a relativistic mean-field calculation from the work of Vretenar *et al.* [40]. The left panel shows their dipole-strength functions obtained for various Ni isotopes. For the neutron-rich isotopes, a peak-like structure is observed around 9 MeV excitation energy, well below the GDR energy region. Many particle-hole configurations are calculated to contribute to the 9 MeV resonance exhausting 4.4% of the TRK sum rule, thus having the character of a collective soft mode (sometimes also referred to as Pygmy resonance). The right panel displays the transition densities for the low-lying peak and the GDR region for ^{78}Ni from the same calculation. One can see that, while for the GDR vibration the protons and neutrons are out of phase, the transition strength for the low-lying states appears to be rather different, showing to a large extent isoscalar character and involving in particular neutrons up to very large radii. The calculated transition strength thus shows the characteristic behavior expected for a vibration

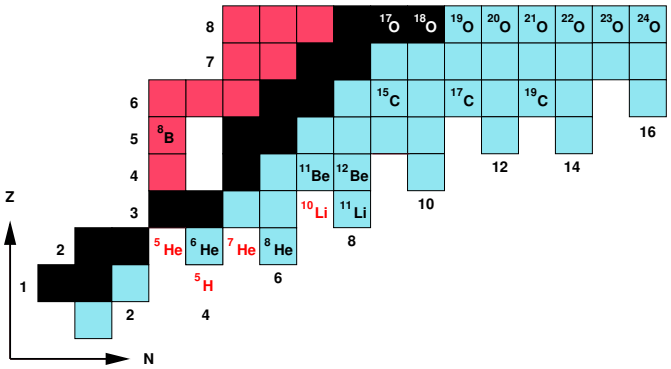

Fig. 4. Lower part of the chart of nuclides showing the region up to the oxygen isotopes, the heaviest element for which the location of the neutron dripline is known experimentally today. The labelled isotopes indicate the nuclei for which experiments are discussed in the present paper.

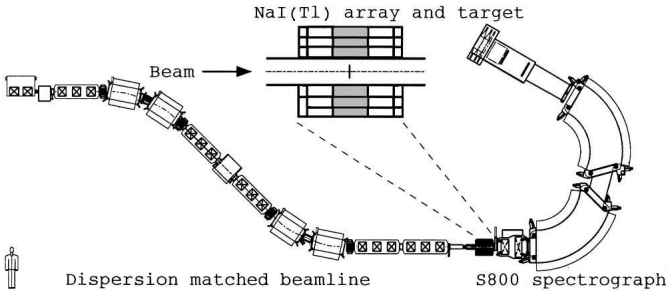

Fig. 5. Experimental setup used at the NSCL to measure one-neutron knockout reactions. Shown are the dispersion-matched beam line, the S800 spectrograph, and the NaI array surrounding the target. The figure is reprinted from Maddalena *et al.* [63]. Copyright (2001) by the American Physical Society.

of the less bound valence nucleons against the core, the soft-dipole vibrational mode.

So far, experimental information on the multipole response of unstable nuclei is rather limited. Low-lying dipole strength was observed in particular for nuclei exhibiting a halo structure, see, *e.g.*, the $E1$ strength distributions measured for the two-neutron halo nuclei ^{6}He [53] and ^{11}Li [54–56], and for the one-neutron halo nuclei ^{11}Be [57–59] and ^{15,19}C [60,61]. The question of the resonant character of this low-lying strength is to our understanding still open for the two-neutron halo nuclei, while for the one-neutron halo nuclei the strength can be attributed to non-resonant dipole transitions to the continuum and is solely related to the single-particle properties of the weakly bound neutron. Such non-resonant transitions, however, are found to be a promising spectroscopic tool [57,60,62], as will be discussed in sect. 3.3.4.

The neutron dripline was reached experimentally to date for the lightest elements up to the oxygen isotopes only. In the present paper, scattering experiments in this mass region performed in the past few years are exemplified. The nuclei discussed are indicated in fig. 4, which shows a chart of nuclides up to $Z = 8$.

The paper is organized in the following way: After a brief introduction into the experimental techniques used (sect. 2), the different types of reactions are discussed. They fall into two groups: i) direct reactions to study the single-particle properties (sect. 3), and ii) continuum (collective) excitations by inelastic nuclear and electromagnetic scattering (sect. 4). Section 5 contains some brief remarks on the astrophysical aspects. Finally an outlook on future experimental developments is given.

2 Experimental techniques

Two detection principles are of relevance for the reactions discussed in this paper: i) the precise measurement of the recoil momentum after one-nucleon removal reactions, and ii) the kinematically complete measurement of the decay from continuum states. For the first type of reactions, the setup used at the NSCL at MSU is described, where most of the knockout experiments discussed in sect. 3.3.2 were performed. The experiments involving neutron decay from continuum states ii), which are discussed in sects. 3.3.3, 3.3.4, and 4, were performed using the LAND detection setup at GSI. Both experiments make use of radioactive beams produced by fragmentation of intermediate or high-energy beams on light, *e.g.*, Be targets with thicknesses ranging from $\approx$ 100 mg/cm^2 to a few g/cm^2 depending on beam energy and projectile. Typical primary-beam energies are 80 MeV/nucleon at the NSCL, and up to $\approx$ 1 GeV/nucleon at GSI. Due to the high beam momenta, the fragmentation products are kinematically forward focussed and can be separated efficiently in flight by using large-acceptance zero-degree magnetic spectrometers like the A1200 separator [64] at MSU or the fragment separator FRS [65] at GSI. Such a selection on magnetic rigidity provides beams containing a mixture of isotopes with similar mass-over-charge ratio and velocities close to the beam velocity. A purification of the beam can be achieved by placing degraders at the dispersive midplane of the separators. A mixed secondary beam is often advantageous, however, since several nuclei can be studied in one experiment, thus making the method very efficient. In such cases, the projectiles are identified on an even-by-event basis using time-of-flight and energy loss measurements. A detailed description of the production and separation of fragmentation beams can be found, *e.g.*, in ref. [65].

Figure 5 shows a drawing of the experimental scheme used at the NSCL to study one-nucleon knockout reactions populating bound states in the $A-1$ daughter nucleus. The fragments produced in the secondary target are momentum analyzed in the S800 spectrograph [66, 67]. In order to achieve a resolution significantly better than the rather large momentum spread of the secondary beam of typically about one percent, the S800 and the beam line are operated in a dispersion-matched mode. Here, the target is located at a dispersive focus of the beam line, while the S800 spectrograph is set to compensate this dispersion. As a result, the position at the final focal plane does not depend on the initial momentum, but only on the momentum change generated by the reaction

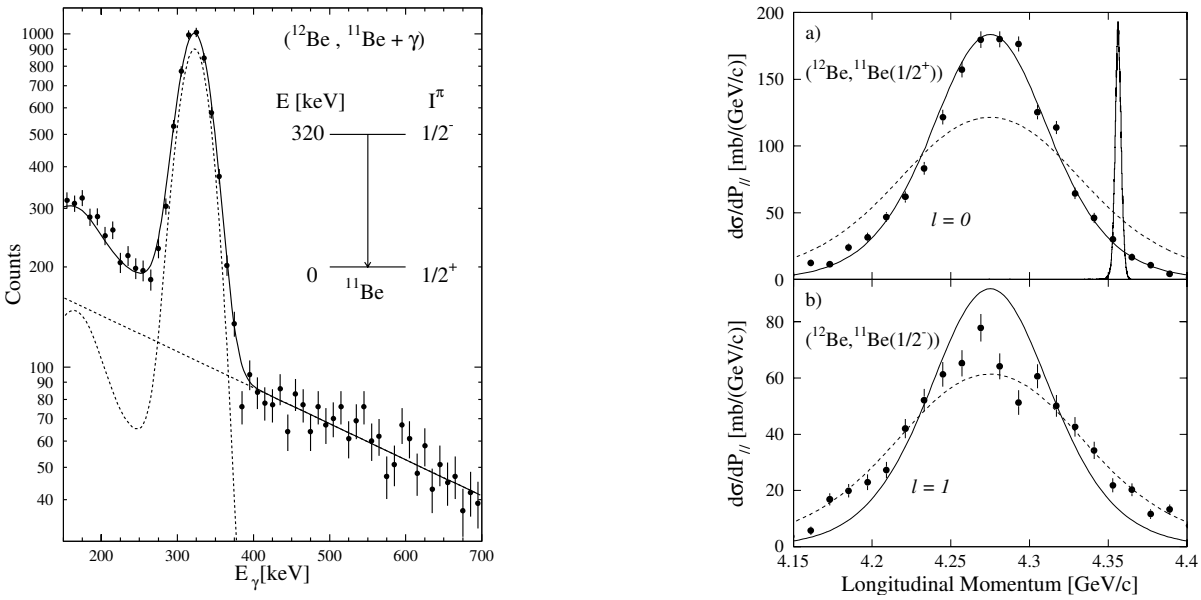

Fig. 6. One-neutron removal reaction from ^{12}Be (78 MeV/nucleon) impinging on a Be target as measured with the S800 spectrometer at the NSCL. Left: Doppler-corrected γ spectrum recorded in coincidence with ^{11}Be fragments. Right: parallel momentum distributions of the ^{11}Be fragments in the laboratory frame populating the ground state (top) and the first-excited state (bottom) of ^{11}Be. Reprinted with permission from Navin *et al.* [68], Copyright (2000) by the American Physical Society.

in the target. In this case, it is possible to measure the recoil momentum of the reaction products with a relative momentum resolution of 0.025%. An example is given in fig. 6: the right panels show the measured momentum distributions of ^{11}Be fragments produced in a one-neutron removal reaction of ^{12}Be on a beryllium target [68]. The upper (lower) part shows the distribution if the ^{11}Be fragments are produced in their ground (first-excited) state. The narrow line in (a) illustrates the resolution obtained for the momentum measurement, which is significantly better than the typical widths of recoil momentum distributions (≈ 100 MeV/c). The figure also shows the longitudinal momentum acceptance of the spectrograph ($\pm 2.5\%$), which allowed a full-acceptance measurement of the momentum distributions in one setting for the case shown. The acceptances in transverse direction amount to $\pm 5^\circ$ ($\pm 3.5^\circ$) in the (non-)dispersive plane. In cases of wide momentum distributions (high ℓ values), corrections for the acceptance have to be applied to obtain the cross-sections (see refs. [69,63] for a discussion).

The target is surrounded by a cylindrical array of NaI detectors, which allow the measurement of coincident γ decays of the fragments. A back-transformation of the Doppler-shifted γ energy to the projectile rest frame can be achieved based on the position information measured with the NaI array [70]. An example of a Doppler-corrected γ spectrum is shown in the left frame of fig. 6, where the decay of the first (and only) excited state at 320 keV in ^{11}Be, populated in the one-neutron removal reaction from ^{12}Be, is visible.

The experimental method applied by the LAND Collaboration at GSI consists of producing high-energy radioactive beams (with typically a few hundred MeV/nucleon kinetic energy) and of a kinematically complete measurement of breakup reactions in secondary targets. The excitation energy prior to decay is reconstructed by utilizing the invariant-mass method. The measurement is exclusive or kinematically complete in the sense that all reaction products with velocities close to the beam velocity and γ-rays are detected. Reaction products stemming from the target are not measured (with the exception of γ-rays). A schematic drawing of the detection setup is shown in fig. 7. Details of the experiment can be found, *e.g.*, in ref. [57]. Here, we give only a very brief description of the method.

The experimental results exemplified in the next sections utilized radioactive beams, which were produced by fragmentation of primary ^{40}Ar and ^{18}O beams delivered by the synchrotron SIS at GSI, Darmstadt. Typical primary-beam intensities are around 10^{10} ions per second. Fragment beams were selected by the Fragment Separator FRS according to their magnetic rigidity only, thus mixed secondary beams containing isotopes with similar mass-over-charge ratio were transported to the experimental area. The incident projectiles, however, were uniquely identified on an event-by-event basis by utilizing energy loss and time-of-flight measurements. An example is shown in the upper left inset in fig. 7, where the composition of a mixed beam produced by fragmentation of ^{40}Ar can be seen, where the settings of the FRS and the beam line were optimized for the transport of ^{22}O.

In a similar manner, the fragments produced in the reaction target are identified. Here, the magnetic rigidity is determined from three position measurements defining the trajectories of the charged projectile residues in the magnetic field of a large-gap dipole magnet (ALADIN) placed behind the target (see refs. [57,71] for details). Additional energy loss and time-of-flight measurements allow unique

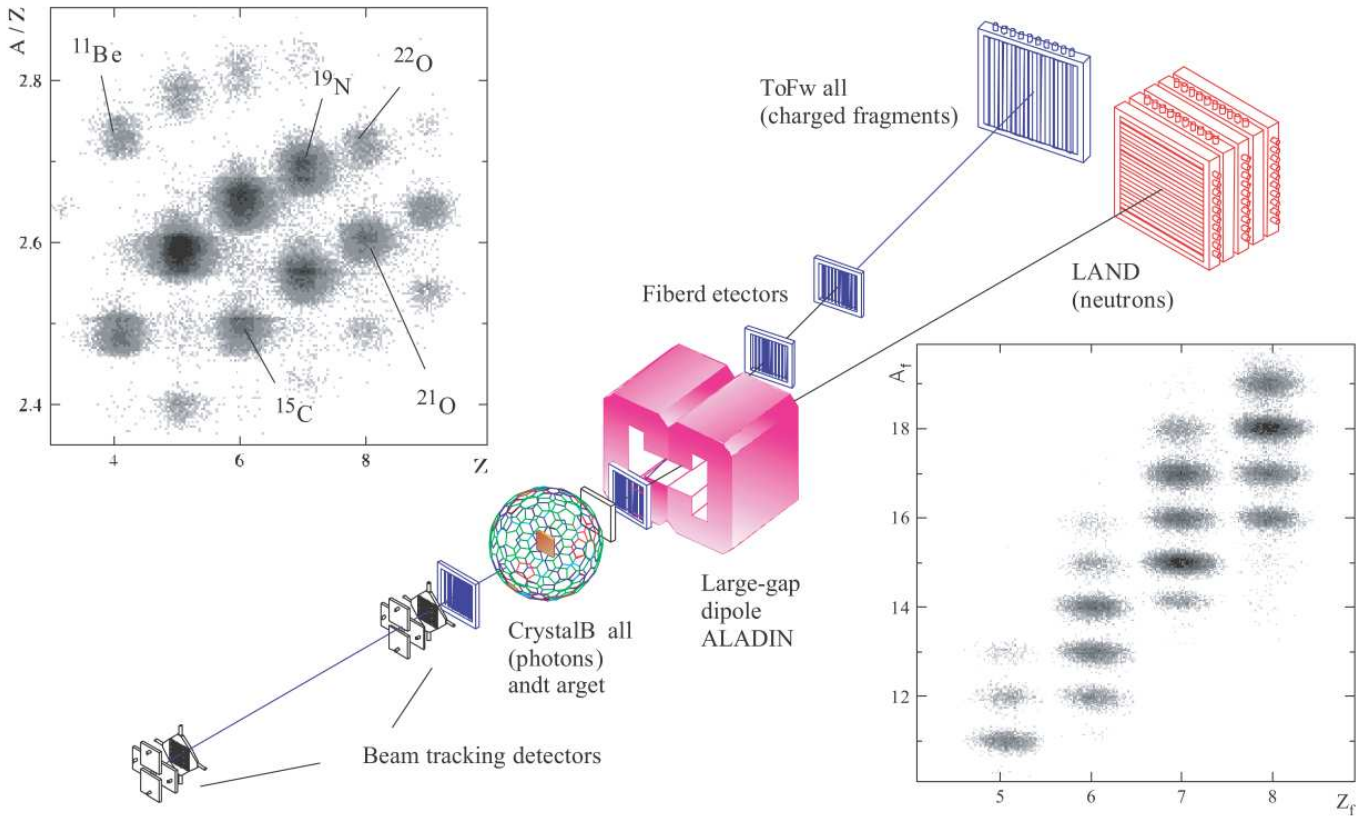

Fig. 7. Schematic drawing of the LAND detection setup (not to scale). Shown are the beam and fragment detectors, the Crystal Ball photon spectrometer, the dipole magnet ALADIN, and the neutron detector LAND, placed about 11 m downstream from the target. The upper left inset shows the composition of a mixed radioactive beam impinging onto the secondary targets, which are inserted at the center of the Crystal Ball. The lower right inset displays the fragment identification for reactions of ^{20}O on a carbon target.

identification of the outgoing fragments and determination of their momenta. The lower right panel of fig. 7 shows an example of identified fragments produced in reactions of ^{20}O on a carbon target [72].

Neutrons emitted from the excited projectile or excited-projectile–like fragments are kinematically focussed in the forward direction and detected with high efficiency ($\sim$ 90%) in the LAND neutron detector [73]. The momenta of the neutrons are determined from the time-of-flight and position information. The angular range for fragments and neutrons covered by the detectors corresponds to a 4π measurement of the breakup in the rest frame of the projectile for fragment-neutron relative energies up to 5.5 MeV (at 500 MeV/nucleon beam energy).

At the high beam energies used, the γ-rays need to be detected with good angular resolution in order to minimize Doppler-broadening effects. Two detectors are used alternatively: the Crystal Ball spectrometer [74], which consists of 160 NaI detectors covering almost the full solid angle, or a CsI array consisting of 144 submodules. The latter covers only the forward hemisphere, but with better angular resolution. Still, the resolution is limited by the Doppler broadening.

The excitation energy prior to decay is obtained by reconstructing the invariant mass combining the measurements described above. The resolution in excitation energy depends on the relative fragment-neutron kinetic energy and the resolution for measuring the γ sum energy (in the projectile rest frame) in case of the population of excited states. It changes from about 200 keV close to the threshold to a few MeV in the region of the giant dipole resonance (at excitation energies around 15 MeV). In order to extract the electromagnetic excitation cross-section from the measurement with the lead target, the nuclear contribution is determined from a measurement with a carbon target and scaled accordingly before subtraction.

3 Direct reactions and single-particle properties

3.1 Spectroscopy with radioactive beams

Direct reactions have played an important role in the past to study the single-particle properties of stable nuclei. The reactions used are transfer reactions, quasi-free scattering, mainly of the $(p, 2p)$ type, as well as $(e, e'p)$ knockout reactions using electron beams. Among these "classical" direct reactions, mainly the transfer reactions were applied to radioactive beams so far. However, new tools were developed, which are applicable to high-energy low-intensity

secondary beams, namely nuclear one-nucleon removal reactions, and Coulomb breakup. Those two types of reactions will be discussed in more detail. Transfer reactions are only sketched very briefly in the next section, and the results will be compared at the end to those obtained from knockout and Coulomb breakup.

3.2 Transfer reactions

A widely used class of reactions to study the single-particle properties of stable nuclei are transfer reactions. The most simple ones are the one-nucleon stripping and pickup reactions of the type $^AX(d,p)^{A+1}X$ and $^AX(p,d)^{A-1}X$, respectively. The single-particle configurations are identified by determining the angular momentum ℓ of the transferred nucleon from the measured angular distribution, while the final state of the residual nucleus is identified using a magnetic spectrometer. From the partial cross-sections to given states, spectroscopic factors are deduced, which provide a measure of the overlap of initial- and final-state wave functions in terms of an expansion in single-particle states (observed in the experiment).

The theory usually used to describe the reaction and to extract the above quantities is the distorted-wave Born approximation (DWBA). The calculation involves potential parameters, which are deduced from systematic studies (of stable nuclei) yielding optical potentials valid for certain mass and energy regions. Effects of breakup and inelastic excitations are also sometimes included, see [75, 76] for a discussion.

The optimum beam energy to study transfer reactions is defined by matching the momentum transfer to the momentum of the valence nucleons, typically around 100–200 MeV/c, corresponding to beam energies of about 10–20 MeV/nucleon. Applying the transfer reaction to short-lived nuclei implies the use of inverse kinematics, which means shooting a radioactive beam ($\sim$ 20 MeV/nucleon) on, *e.g.*, a proton target. The experimental challenges are to achieve high enough angular and energy resolution, and sufficient beam intensities. Fortier *et al.* [77,78] succeeded in performing such a transfer reaction in inverse kinematics using a 35 MeV/nucleon ^{11}Be secondary beam (3×10^4 ions/s) provided by the GANIL accelerator facility. The measured position spectrum of the ^{10}Be fragments at the focal plane of the spectrometer is shown in fig. 8 (left panel) without (upper frame) and with (lower frame) coincidences of deuterons emerging from the $(CH_2)_n$ target. The different states in ^{10}Be populated in the reaction are clearly visible. The 6 MeV peak arises from a group of non-resolved states, most probably negative-parity states populated after removal of $p_{3/2}$ neutrons from the ^{10}Be core. The angular distributions (right panel) for the population of the ground and first-excited (2^+) state of ^{10}Be reveal the typical pattern for angular momenta $\ell = 0$ and $\ell = 2$, respectively. From the DWBA analysis, spectroscopic factors for these two single-particle components were extracted [77,78]. The results are discussed in comparison with the results obtained from other reactions, namely the nuclear one-neutron removal reaction (sect. 3.3.2) and the Coulomb breakup (sect. 3.3.4).

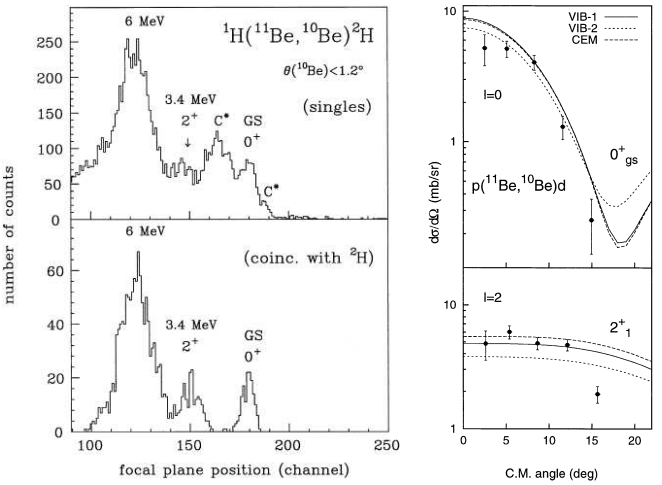

Fig. 8. Transfer reaction utilizing a 35 MeV/nucleon ^{11}Be beam impinging on a $(CH_2)_n$ target. Left: position distribution of ^{10}Be fragments at the focal plane of the spectrometer. Right: angular distributions for transitions to the ^{10}Be ground state (upper panel) and to the first-excited 2^+ state (lower frame). The curves denote results from DWBA calculations. Figures reprinted from Fortier *et al.* [77], Copyright (1999), with permission from Elsevier.

3.3 Knockout and neutron removal reactions

3.3.1 Reaction mechanisms

Key aspect of reactions using high-energy radioactive beams is the fact that the reaction occurs fast, fast compared to the time scale of the internal motion of nucleons inside the nucleus. At beam energies above a few tens of MeV/nucleon, the internal degrees of freedom can be considered to a very good approximation as "frozen" during the collision, the so-called "sudden approximation" or "adiabatic approximation" [75,37]. In this approximation, the momentum of the recoiling fragment after one-nucleon removal provides a direct measure of the wave function of the removed nucleon. Sauvan *et al.* [79,80] studied systematically one-neutron removal reactions for neutron-rich nuclei in the *psd* shell. Figure 9 summarizes their measured inclusive momentum distributions of the $A-1$ fragments [79]. Pronounced changes in nuclear structure are clearly visible from this figure for some nuclei: The shape and width of momentum distributions changes dramatically for neutron-rich isotopes when moving across the $N = 8$ or $N = 14$ neutron shells. The narrow momentum distributions observed in these cases, *e.g.*, for ^{15}C and ^{23}O, provide a signature for the development of a halo-like extended neutron wave function. This is explained by a large spectroscopic factor for s single-particle states in conjunction with low separation energies. The structure of these nuclei will be discussed in more detail together with exclusive measurements of the electromagnetic and nuclear induced one-neutron removal reactions later in this section. The sensitivity of the momentum distributions to nuclear structure even in inclusive experiments is clearly demonstrated in fig. 9.

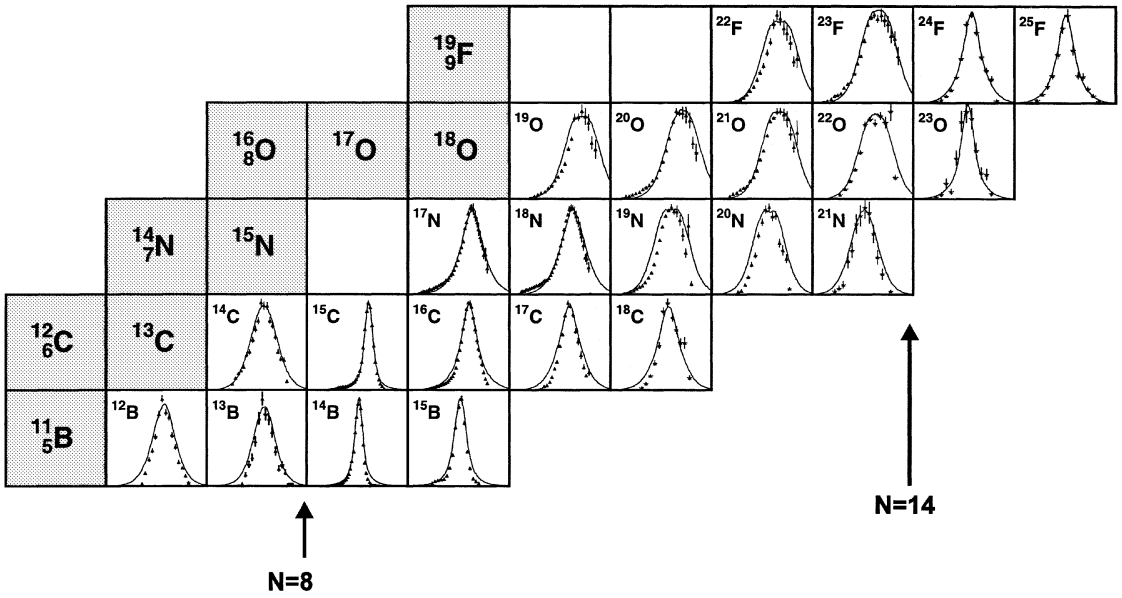

Fig. 9. Inclusive longitudinal momentum distributions of the $A-1$ fragments after one-neutron removal from various projectiles as indicated. The measurements were performed at GANIL using beam energies around 60 MeV/nucleon [79]. The figure is taken from the work of Sauvan *et al.* [79], Copyright (2000), with permission from Elsevier.

Another important approximation, the eikonal approximation, can be applied at high beam energies since the scattering process is concentrated to forward angles. This makes the theoretical treatment of the reaction much simpler and the extraction of nuclear-structure observables more reliable, since reaction and structure are disentangled.

Depending on the target used, different reaction mechanisms are important. For light targets, *e.g.*, Be or C targets, the reaction is dominated by the nuclear interaction, while for heavy targets such as lead, the electromagnetic interaction will dominate the process. Not only the valence or halo neutron can be removed in the reaction, but also more deeply bound neutrons might be removed from an inner shell, *i.e.*, from a core state. Commonly, three different reaction mechanisms are considered to contribute to the one-neutron removal channel:

i) Knockout of a neutron from the projectile (inelastic breakup). The knockout reaction may be viewed as a quasi-free scattering of the neutron off the target. The neutron-target reaction will result in a relatively large momentum transfer to the neutron. As a consequence, the neutron will be scattered to large angles or even be absorbed by the target and will thus not appear as a projectile-like fragment in the forward direction (with a velocity close to the beam velocity). In the literature, this process is sometimes referred to as absorption or stripping.
ii) Nuclear inelastic scattering into the resonant or non-resonant continuum. In case of halo nuclei, this process is often considered as a diffractive dissociation or diffraction of the neutron, analogous to Fraunhofer diffractive scattering of light on a black sphere. Since this process corresponds to an elastic scattering of the neutron off the target, this reaction mechanism is frequently referred to as elastic breakup.
iii) Electromagnetic dissociation (Coulomb breakup) due to the rapidly varying electromagnetic field of a high-Z target experienced by the fast moving projectile. The inelastic electromagnetic scattering may populate resonant states (*e.g.*, the giant dipole resonance), or cause non-resonant transitions into the continuum. The latter process is especially important for weakly bound nucleons yielding large dipole transition matrix elements close to the neutron threshold ("threshold strength"). Due to the smaller effective charge for higher multipolarities [81], the cross-section is dominated by dipole excitations.

3.3.2 Nuclear one-neutron removal reactions

Cross-sections. The cross-sections for the nuclear induced one-neutron removal reaction can be calculated using the eikonal approximation, which is well justified at the high beam energies of interest here. The single-particle cross-sections $\sigma_{\rm sp}^{\rm knock}$ and $\sigma_{\rm sp}^{\rm diff}$ for the two contributing reaction mechanisms, knockout and diffraction, respectively, can be calculated separately [82,83]:

$$\sigma_{\rm sp}^{\rm knock} = \int {\rm d}\boldsymbol{b}\ \langle (1-|S_n|^2)|S_c|^2\rangle, \tag{1}$$

$$\sigma_{\rm sp}^{\rm diff} = \int {\rm d}\boldsymbol{b}\ [\langle |(1-S_cS_n)|^2\rangle - |\langle (1-S_cS_n)\rangle|^2]. \tag{2}$$

Here $\langle\ \rangle$ denotes a ground-state expectation value and S_c and S_n the profile functions for the core-target and

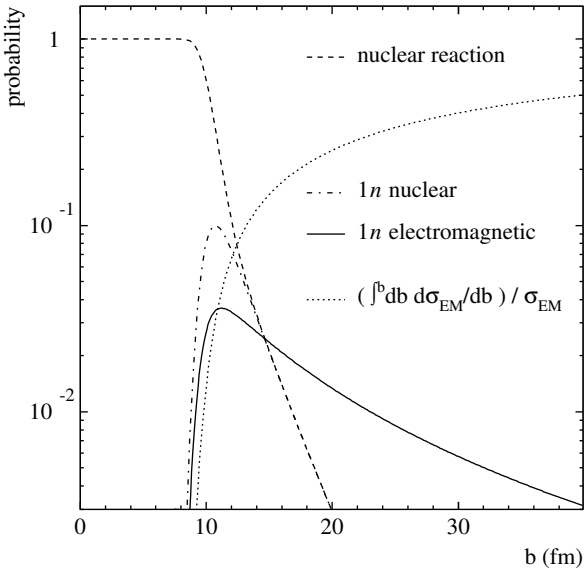

Fig. 10. Dissociation probabilities for 520 MeV/nucleon ^{11}Be on lead as a function of impact parameter b. The dashed curve displays the total nuclear reaction probability, while the dash-dotted and solid curves show the one-neutron removal probability for nuclear and electromagnetic dissociation, respectively. The dotted curve indicates the cross-section for electromagnetic dissociation as a function of the upper integration limit b, normalized to its asymptotic value. This value reaches 50% for $b = 40$ fm. Reprinted with permission from Palit *et al.* [57], Copyright (2003) by the American Physical Society.

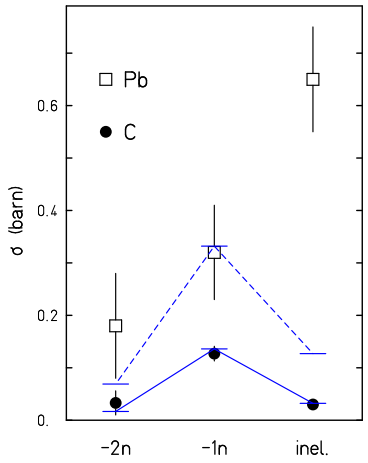

Fig. 11. Cross-sections for breakup reactions of 240 MeV/nucleon ^{6}He into α plus neutrons on carbon and lead targets. The solid and dashed lines connect the values from calculations in an eikonal model (see text). Reprinted with permission from ref. [53], Copyright (1999) by the American Physical Society.

neutron-target systems, respectively. The quantities S_c and S_n are expressed as functions of their individual impact parameters and are calculated in the eikonal approximation using density distributions for the target and the core with parameters reproducing measured cross-sections. As an approximation, we make use of the "no-recoil limit" [83], in which the impact parameter of the core is assumed to coincide with the impact parameter b of the projectile. In this case the core-target profile function can be taken outside the expectation value and the probability, *e.g.*, for the one-neutron knockout, reduces to

$$P_{\rm sp}^{\rm knock}(\boldsymbol{b}) = S_c^2(\boldsymbol{b})\langle 1 - S_n^2(\boldsymbol{b}_n)\rangle = S_c^2(\boldsymbol{b}) \int {\rm d}^3r \; |\phi_{n\ell lj}(\boldsymbol{r})|^2 (1 - S_n^2(\boldsymbol{b}_n)), \quad (3)$$

where $\phi_{n\ell j}(\boldsymbol{r})$ denotes the single-particle wave function with quantum numbers $n\ell j$ expressed in terms of the relative core-neutron distance $\boldsymbol{r}$. In this representation, S_n and S_c have a very clear meaning: $\langle 1 - S_n^2\rangle$ yields the reaction probability of the neutron with the target, while S_c guarantees the survival of the core ("shadowing effect"). The result is a surface-peaked reaction probability as displayed in fig. 10 (dash-dotted curve) for the knockout of the $2s_{1/2}$ neutron from ^{11}Be on a lead target. The total probability for a nuclear reaction of ^{11}Be with the target is shown as a function of the impact parameter by the dashed curve. The neutron-core relative-motion wave functions $\phi_{n\ell j}$ are calculated in a Woods-Saxon potential with radius $r_0 = 1.25$ fm and diffuseness $a = 0.7$ fm.

A similar intuitive expression as for the knockout (eq. (3)) can be found for diffractive breakup by making use of the no-recoil limit. In that case, eq. (2) reduces to

$$P_{\rm sp}^{\rm diff}(\boldsymbol{b}) = S_c^2(\boldsymbol{b})\langle|(1 - S_n(\boldsymbol{b}_n))|^2\rangle - |\langle(1 - S(\boldsymbol{b}))\rangle|^2. \quad (4)$$

The first term describes the elastic scattering of the neutron off the target with the S_c in front ensuring the core survival, while the second term subtracts the part where the projectile is not excited (elastic scattering of the projectile with scattering function $S = S_c S_n$). This corresponds to the view of the breakup caused by diffraction of the neutron at the target. The fact that the difference between the results using eqs. (2) or (4) is small (20% in case of ^{11}Li [83]) tells us that the neglected contribution, corresponding to elastic scattering of the core (or both neutron and core) followed by breakup is small, contributing mainly to the elastic channel. The expression for the diffractive scattering contains also excitations to bound states in the projectile. Calculating the one-nucleon removal cross-sections by using eq. (2) thus implies the assumption that the projectile has no bound excited states, which is a good approximation for very loosely bound nuclei. The relative contribution of the two components depends on the beam energy but also on the single-particle properties. At high energies (few hundred MeV/nucleon), the dominant process to the one-neutron removal channel is knockout. At lower energies (50 MeV/nucleon), the process cannot be described by the forward imaginary scattering amplitude only, and an optical potential including a real part has to be considered [84,82] accounting for most of the rise of the cross-section for diffractive breakup at lower energies. In particular for loosely bound neutrons in low-angular-momentum states, the diffraction cross-section becomes larger, *e.g.*, about one half of the neutron removal cross-section for the ^{11}Be breakup at 50 MeV/nucleon [69], and $\sim$ 20% at 500 MeV/nucleon.

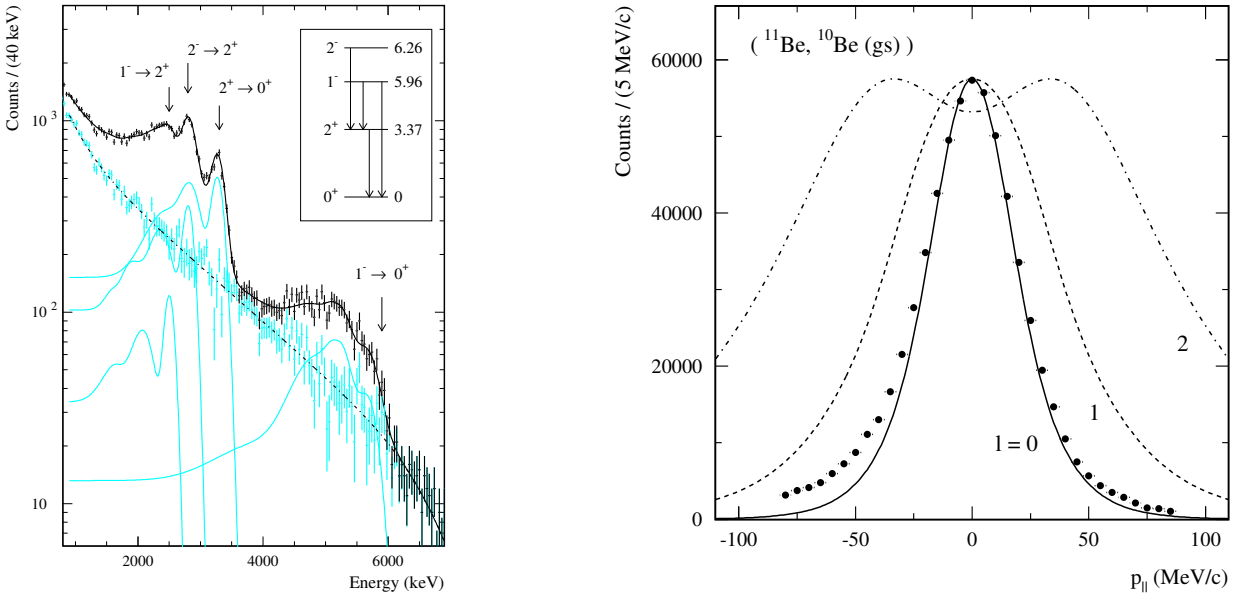

Fig. 12. One-neutron removal reaction of ^{11}Be (60 MeV/nucleon) on a Be target measured with the S800 spectrometer at the NSCL. Left: Doppler-corrected γ spectrum measured in coincidence with ^{10}Be. Right: parallel momentum $p_{\|}$ distribution of the ^{10}Be fragments in the rest frame of the projectile. Only the contribution leading to the ground state of ^{10}Be is shown. The data are compared to calculations assuming different ℓ values as indicated demonstrating the sensitivity of the $p_{\|}$ distribution to the angular momentum ℓ of the removed nucleon. Reprinted with permission from Aumann *et al.* [69], Copyright (2000) by the American Physical Society.

For more deeply bound nucleons, the knockout process becomes dominant also at lower energies, justifying the approximation discussed above. For the breakup of 240 MeV/nucleon ^{6}He in a carbon target the cross-section ratio $\sigma^{\rm diff}/\sigma^{\rm knock}$ was measured amounting to about 1/4 [53], see fig. 11 and the discussion in the next section.

The treatment of the nuclear inelastic-scattering (diffractive) cross-section as described above neglects the neutron-core final-state interaction (see the related discussion in the context of Coulomb breakup in sect. 3.3.4) and ignores energy conservation. Despite a small effect (an excitation energy of a few MeV has to be compared to the beam energy), the latter can explain the small deviations between the measured momentum distribution after ^{11}Be breakup and the eikonal calculation visible in fig. 12. A more elaborated treatment of the reaction was performed by Tostevin *et al.* using a coupled-channels approach with discretized continuum [85]. The authors obtained an excellent description of the data including the slight asymmetry of the distribution. The excitation of the projectile causes a slowing-down and thus a shift of the core momentum towards negative values (in the rest frame of the projectile). At higher energy, the eikonal approximation becomes very accurate as shown recently by Esbensen and Bertsch [86]: their result from calculations solving numerically the time-dependent Schrödinger equation agrees within one percent with the eikonal result for beam energies of several hundred MeV/nucleon. For a more detailed discussion of non-eikonal theories and the limitations and accuracy of the description we refer to the article by Esbensen and Bertsch [86], the coupled-channels calculations by Tostevin *et al.* [85], and the review article by Hansen and Tostevin [39], as well as to references cited therein.

The partial theoretical cross-sections are calculated separately for the (observed) core state I_c^π and is commonly assumed to be a product of a spectroscopic factor C^2S and a single-particle cross-section $\sigma_{\rm sp}$ given by the sum of eqs. (1) and (2) [84] (plus a Coulomb breakup part, which is usually negligible in case of light targets, see the next section):

$$\sigma_{1n}(I_c^\pi) = \sum_{n\ell j} C^2S(I_c^\pi, n\ell j)\sigma_{\rm sp}(I_c^\pi, n\ell j). \qquad (5)$$

The total (inclusive) one-neutron removal cross-section can be evaluated by summing over all contributing configurations populating final core states (I_c^π).

Momentum distributions. The interest in one-neutron removal reactions using fast radioactive beams was triggered by the study of halo nuclei. In the sudden approximation, the recoiling momentum of the $A-1$ fragment (in the rest frame of the projectile) is equal to the momentum of the removed nucleon (with opposite sign). The momentum distribution of the recoiling fragment thus corresponds to the Fourier transformation of the nucleon's wave function. Indeed, for halo nuclei, much narrower momentum distributions were found in breakup reactions [87] reflecting the spatial extension of the halo (see, *e.g.*, the review of Orr [14]). The simple picture of a Fourier transformation of the wave function, corresponding to the transparent limit of the Serber model [88], however, failed in reproducing the data quantitatively. The reaction channel requires that the core survives the collision. Consequently, the reaction probability is surface peaked, and the momentum distribution reflects only part of the wave function.

This was already realized in the analysis of fragmentation data of stable beams from the Bevalac, see, *e.g.*, the paper by Hüfner and Nemes, *Relativistic heavy ions measure the momentum distribution on the nuclear surface* [89]. In case of halo nuclei, the effect is less pronounced, though. It became most important when trying to understand the narrow momentum distribution of the one-proton halo nucleus ^{8}B [90]. Here, the surface localization of the reaction yields a rather large effect on the observed width of the momentum distribution since the proton is in a p state. The centrifugal barrier together with the Coulomb barrier confines the wave function. The effect of surface localization is much more pronounced in this case since only a small part of the wave function is probed by the reaction resulting in a width of the momentum distribution much narrower than expected from a Fourier transformation of the wave function. By taking this effect into account properly, Esbensen [91] and Hansen [92] could quantitatively reproduce the width of the measured distribution.

Since the asymptotic decay of the wave function outside the nuclear potential depends only on the separation energy and the angular momentum of the nucleon (apart from the Coulomb barrier), one can directly determine the ℓ value of the removed nucleon from the shape of the measured momentum distribution (assuming the separation energy is known). This sensitivity is demonstrated in fig. 12 (right panel), where the experimental distribution is compared to calculations assuming different ℓ values for the knocked-out neutron. Usually, the distributions in longitudinal momentum $p_{\parallel}$ (parallel to the beam direction) are analyzed because they are not distorted by other effects like Coulomb deflection. Such effects are, however, small for light targets and in particular at high energies. For a detailed theoretical analysis of longitudinal and transverse momentum distributions and their differences we refer to the articles by Sauvan *et al.* [80], Carstoiu *et al.* [93], and Bertulani and Hansen [94].

Coincident measurement of γ-rays. Another assumption which was made in the early (inclusive) measurements of breakup reactions was neglecting nucleon removal from more deeply bound states. Although such contributions turn out to be small for halo nuclei, they can contribute significantly in particular to the tails of the momentum distributions. Figure 12 shows results from an experiment performed at MSU with a ^{11}Be beam [69]. The left part of the figure shows the γ spectrum in coincidence with ^{10}Be fragments produced from a 60 MeV/nucleon ^{11}Be beam impinging on a Be target. Several excited states are observed, the group at 6 MeV stems from the decay of negative-parity levels in ^{10}Be populated after removal of a p neutron from the ^{10}Be core, while the halo s neutron acts as a spectator. The coincident measurement of γ-rays allows to differentiate the momentum distributions according to the different states populated, and thus to disentangle the contributions of different single-particle components to the reaction. From the resulting partial cross-sections, spectroscopic factors may be obtained by comparing to theoretical cross-sections (see previous paragraph). In the example shown, the momentum distribution solely related to the knockout of the halo s neutron of ^{11}Be was extracted (after subtracting contributions from excited states) [69], which exhibits a very small width reflecting the large spatial extension of the ^{11}Be neutron halo. From the cross-sections, spectroscopic factors for the $\nu 2s_{1/2}\otimes^{10}\mathrm{Be}(0^+)$ and the $\nu 1d_{5/2}\otimes^{10}\mathrm{Be}(2^+)$ single-particle configurations were extracted [69]. The spectroscopic factor of 0.87(13) for the s component is in good agreement with the shell-model prediction, as well as with a measurement [95] of the magnetic moment at ISOLDE, and the transfer reaction experiment discussed in the previous section.

In summary, the method of nuclear nucleon removal reactions as a spectroscopic tool consists of a measurement of the states populated in the $A-1$ nucleus by means of γ coincidences, plus a measurement of the recoil momentum of the $A-1$ fragments differentiated according to the final core states yielding the ℓ values of the removed nucleons (in general, these can be configurations with mixed angular momenta). Finally, spectroscopic factors are derived from the partial cross-sections by comparing to theoretical single-particle cross-sections.

3.3.3 Knockout to continuum states

Reaction mechanisms. Among the halo nuclei observed at the neutron dripline, two-neutron halo nuclei have attracted particular interest due to their three-body character with its two-body subsystems being both unbound [8, 96]. Because of this property they were named "Borromean" nuclei [8]. Examples are the neutron halo nuclei ^{6}He, ^{11}Li, and ^{14}Be, or ^{17}Ne on the proton-rich side. The one-nucleon removal reaction discussed above populates in this case unbound states in the $A-1$ systems, which decay in flight. Considering only reactions where the core remains intact, the following reaction mechanisms may be distinguished for high-energy beams: i) A one-nucleon knockout reaction followed by the decay of the $A-1$ unbound system. While the nucleon knocked out by the target will be scattered to large angles or even be absorbed, the second nucleon will be emitted from the decay in flight with small core-nucleon relative energy, thus it will be detectable in the forward direction. ii) Both nucleons might react with the target, corresponding to a simultaneous two-nucleon knockout reaction. In that case none of the nucleons will be observed in the projectile rapidity domain. iii) Inelastic excitation to the continuum of the projectile by nuclear or electromagnetic interaction with subsequent decay. In that case, both nucleons will have a velocity close to the beam velocity.

Cross-sections. As an example, breakup reactions of a 240 MeV/nucleon ^{6}He beam on carbon and lead targets studied with the LAND reaction setup at GSI (see fig. 7) [53] shall be discussed. Since the structure of ^{6}He is well understood, we consider the fragmentation of ^{6}He as a test case to study the interplay between nuclear structure and reaction mechanisms. In the analysis of ref. [53], the different reaction mechanisms were characterized according to the apparent neutron multiplicity m_n in the LAND

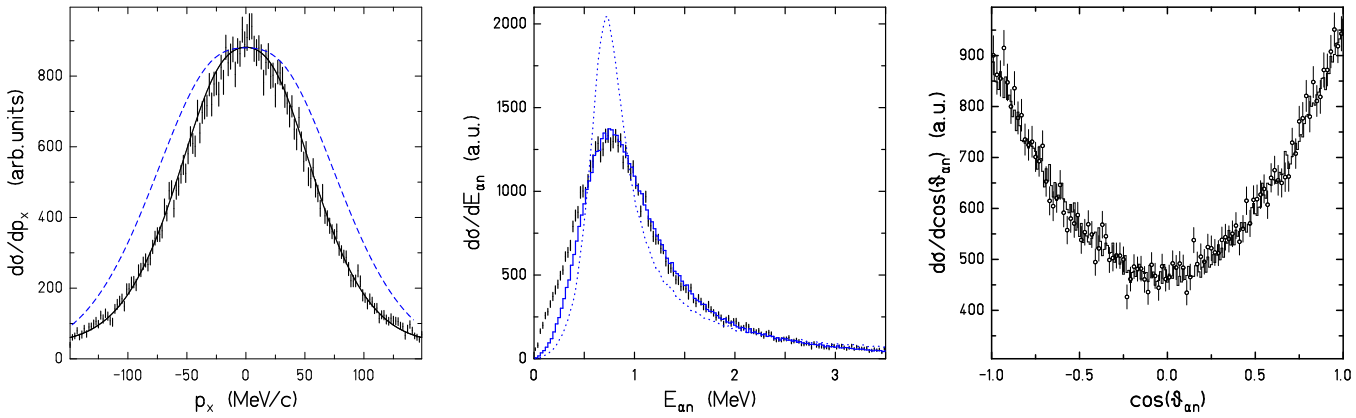

Fig. 13. One-neutron removal reaction from ^{6}He (240 MeV/nucleon) on a C target measured with the LAND reaction setup at GSI [97,98]. Left panel: transverse momentum distribution of ^{5}He compared to calculations with (solid curve) and without (dashed curve) taking into account the peripheral nature of the reaction. Middle panel: α-n relative-energy distribution. The dotted curve shows the ^{5}He ground-state resonance, which after convolution with the instrumental response (solid histogram) accounts for most of the measured cross-section. Right panel: angular correlations in the decay of ^{5}He (see text). Figures reprinted with permission from ref. [99]. Copyright (1998) by the American Physical Society.

neutron detector placed at zero degree covering angles of up to ± 70 mrad. The resulting cross-sections are displayed in fig. 11 for reactions with carbon (full symbols) and lead (open symbols) targets. The labels "$-2n$" (two-neutron knockout), "$-1n$" (one-neutron knockout) and "inel." (inelastic excitation) correspond to apparent neutron multiplicities of $m_n = 0, 1, 2$, respectively. Although there is no well-defined division line between the different reaction mechanisms discussed above in terms of the angular distribution of the neutrons in the laboratory frame, the distributions are sufficiently different to separate the contributions. The angular distribution of neutrons after reacting with a carbon target was estimated by Zinser *et al.* [56] for 280 MeV neutrons using the intra-nuclear cascade code Isabelle [100] showing that very little intensity falls within the acceptance of LAND. The distribution is very broad and peaks around 30°, while the neutrons stemming from a decay of resonant or non-resonant states in the continuum are detected with good efficiency up to 7 MeV excitation energy (see ref. [53] for details). The cross-sections differentiated according to the measured neutron multiplicity as shown in fig. 11 are thus expected to resemble the different reaction mechanisms. This is corroborated by the fact that the distribution of the breakup cross-section among the three reaction channels, $2n$ knockout, $1n$ knockout, and inelastic excitation (diffraction) can be perfectly well reproduced by the eikonal calculation [83] for the carbon target, see bars connected by solid lines in fig. 11. For the lead target, the experimental (open symbols) $1n$ and $2n$ knockout cross-sections are reproduced by the eikonal calculation (bars connected by dashed lines) within the experimental errors as well, but a considerable excess for the experimental inelastic cross-section is found, which can be attributed to electromagnetic excitations [53].

Momentum distributions. In case of nucleon knockout reactions to the continuum, the momentum distribution of the core fragment is not directly related to the intrinsic momentum of the knocked nucleon as discussed in the previous section. Both the fragment and the neutron distributions are influenced by the final-state interaction between the neutron and the fragment [101–105]. By taking such final-state interactions into account, the measured momentum distributions [97] could be reproduced [88]. The sensitivity on the original wave function, however, seems to be partially lost, since different wave functions [106,107,101] yield good agreement with the experimental distributions. The center-of-mass motion of the (fragment + neutron) system, however, is not influenced by final-state interactions, and thus can directly be compared to the model calculations as pointed out in ref. [88]. The width of the momentum distribution is governed by the asymptotic decay of the wave function and thus by the ℓ value and the separation energy.

The transverse momentum distribution of the recoiling unbound ^{5}He after one-neutron knockout from 240 MeV/nucleon ^{6}He projectiles in a carbon target (as reconstructed from α and neutron momenta) is displayed in the left panel of fig. 13. The dashed curve corresponds to the full Fourier transformation of the three-body wave function from ref. [108]. After introducing a radial cutoff in order to account for the peripheral nature of the reaction process, perfect agreement with the experimental data was achieved [88] (solid curve). The method outlined by Hansen [92] was used, but applied to a two-neutron halo nucleus. Therefore, the asymptotic of the three-body wave function was approximated by a Hankel function for $\ell = 1$. A good fit to the three-body wave function is achieved for a one-neutron separation energy of 1.75 MeV [88], very close to the value of 1.86 MeV [109] expected for the binding energy of ^{6}He ($S_{2n} = 0.97$ MeV) relative to the separation in ^{5}He (g.s. at 0.89 MeV) and the neutron. The difference of the two curves visualizes the influence of the reaction mechanism. The second observable being sensitive to the asymptotic of the wave function and thus to the separation energy is the cross-section. By applying

eq. (1) using a single-particle wave function for $\ell = 1$ and a separation energy of $S_n = 1.86$ MeV, a cross-section of 66 mb is obtained. By comparing to the experimental cross-section of 127(14) mb [53], a spectroscopic factor of 1.9(2) is obtained in good agreement with the expectation of 2 for a $\alpha + n + n$ three-body structure of ^{6}He.

Invariant-mass spectroscopy. Similar to the γ coincidence measurement after one-nucleon removal as discussed in the previous section, the states populated in the daughter nucleus may be identified in the case of population of unbound states by the invariant-mass method. The invariant-mass spectrum of ^{5}He (α-n relative-kinetic-energy distribution) after one-neutron knockout from ^{6}He in a carbon target is displayed in the middle frame of fig. 13 [97]. A prominent peak coinciding with the energy of the known $p_{3/2}$ ^{5}He ground-state resonance is visible. A Monte Carlo calculation starting from a Breit-Wigner parametrization of this resonance with parameters taken from the literature (dotted curve) can reproduce the data very well for energies larger than 0.5 MeV (solid histogram). Contributions involving excited states of ^{5}He are not evident. Additional evidence for the dominance of this resonance is obtained by inspecting the correlation function deduced by dividing the experimental spectrum with a randomized one (see ref. [97] for details). Moreover, the momentum distributions of the neutron and the α-particles can be reproduced by assuming a two-step process: one-neutron knockout leading to the unbound ^{5}He resonance (with a comparatively long lifetime of about 300 fm/c), which subsequently decays into $\alpha+n$ (far away from the reaction zone) [97].

Angular correlations. The presence of the intermediate ^{5}He resonance can also be seen in the angular correlation observed between the direction of the ^{5}He momentum and the α-n relative momentum $\boldsymbol{p}_{\alpha n} = \frac{m_n m_\alpha}{m_n+m_\alpha}(\frac{\boldsymbol{p}_\alpha}{m_\alpha} - \frac{\boldsymbol{p}_n}{m_n})$ [98]. The distribution on this angle $\vartheta_{\alpha n}$ is shown in the right panel of fig. 13 exhibiting an anisotropy characteristic for a relative angular momentum $\ell_n = 1$. The solid histogram, which describes the data very well, results from a Monte Carlo calculation assuming an angular-correlation function $W \sim 1 + 1.5\cos^2(\vartheta_{\alpha n})$. Experimental effects are taken into account in the Monte Carlo procedure. A two-step process involving only the $p_{3/2}$-resonance, however, would yield a correlation function $W \sim 1+3\cos^2(\vartheta_{\alpha n})$, an anisotropy twice as large as the observed one. Chulkov and Schrieder [110] have shown that the experimental result can quantitatively be understood by assuming a 7% admixture only of the higher-lying $p_{1/2}$-resonance in ^{5}He. In turn, the presence of the angular correlation between the ^{5}He momentum and the decay direction (or momentum of the second neutron) shows that the $(\alpha+n)$ center-of-mass motion indeed is correlated to the initial momentum of the halo neutron prior to the knockout reaction, and thus carries the information on the projectile wave function.

In summary, the breakup reaction of $2n$ halo nuclei on light targets is dominated by a two-step process: knockout of one of the halo neutrons populating states in the unbound $A-1$ nucleus, which subsequently decay into core + n. A small fraction of the nuclear breakup cross-section can be attributed to inelastic excitation of the projectile, see sect. 4 for further discussion. A differentiation of the various reaction mechanisms can be achieved according to the neutron multiplicity apparent in forward direction. The states populated in the daughter nucleus are identified by the invariant-mass method, the angular momentum ℓ of the knocked-out neutron is determined from the momentum distribution of the core + n recoiling system. Further information on the quantum numbers of the states involved is obtained from the angular correlations.

3.3.4 Coulomb breakup

The electromagnetically induced one-nucleon removal reaction may be utilized as a spectroscopic tool in a similar manner as the nuclear reaction discussed in the previous section. Again, a coincident measurement of the $A-1$ fragment and γ-rays yields the partial cross-sections from which the spectroscopic factors are deduced. In this case, the observable being sensitive to the angular momentum of the removed nucleon is the dipole-strength distribution which is extracted from the differential cross-section for electromagnetic excitation.

The large cross-sections observed for the electromagnetic dissociation of halo nuclei can be explained by non-resonant transitions to the continuum due to a large overlap between the tail of the neutron wave function and continuum wave functions with large wavelength, *i.e.*, small relative momenta q (direct-breakup model). Since the effective charge $Z_{\rm eff} \sim A^{-\lambda}$ (with λ being the multipolarity) gets smaller for higher multipolarities, the breakup process is dominated by dipole transitions. Typel and Baur [81] estimated the $E2$ contribution for the Coulomb breakup of ^{19}C, for instance, to be more than three orders of magnitude smaller than the $E1$ cross-section. Quadrupole and higher multipolarities can thus safely be neglected and the differential cross-section can be factorized into the number $N_{E1}(E^*)$ of equivalent dipole photons with energy E^* associated with the rapidly varying Coulomb field of the target, and the square of the dipole matrix elements [111, 112]:

$$\frac{\mathrm{d}\sigma}{\mathrm{d}E^*}(I_c^\pi) = \left(\frac{16\pi^3}{9\hbar c}\right) N_{E1}(E^*) \sum_{nlj} C^2 S(I_c^\pi, n\ell j) \times \sum_m |\langle \boldsymbol{q}|(Ze/A) r Y_m^1 |\phi_{n\ell j}(r)\rangle|^2. \quad (6)$$

$N_{E1}(E^*)$ is calculated using the semiclassical approximation [113] with a minimum impact parameter $b_{\rm min}$ obtained, *e.g.*, from the parametrization given in ref. [114]. The influence of this particular choice for $b_{\rm min}$ is not very important for halo nuclei and can be verified by a calculation making use of the eikonal approach which avoids using this parameter resulting in a smooth cutoff when the strong absorption sets in [115] (see also the calculated probability for Coulomb breakup as a function of the impact parameter b, shown by the solid curve in fig. 10).

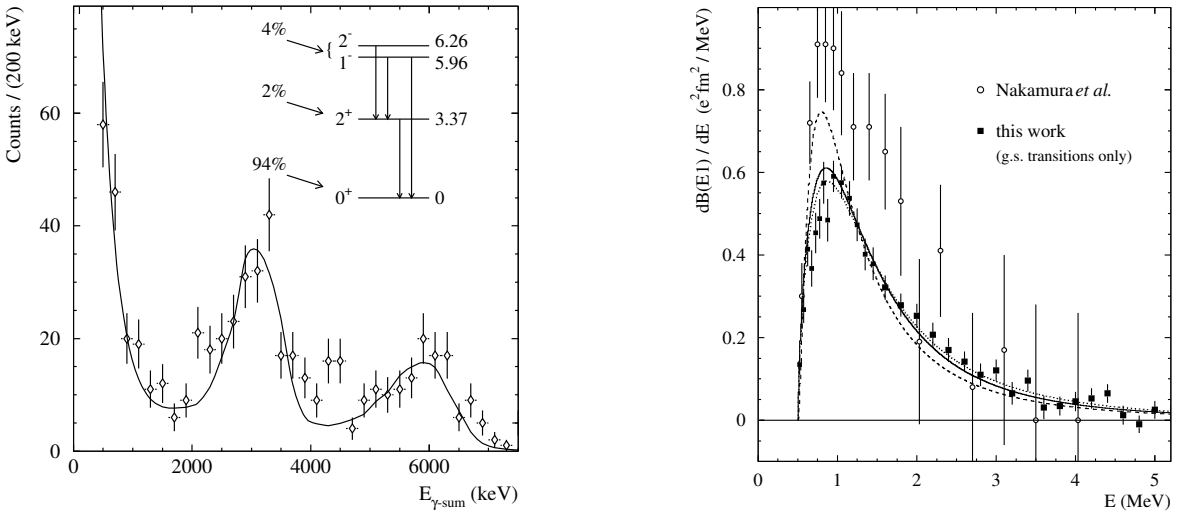

Fig. 14. Breakup of 520 MeV/nucleon ^{11}Be into ^{10}Be and one neutron measured with a lead target [57]. Left: Doppler-corrected γ-sum energy spectrum measured with the Crystal Ball in coincidence with a ^{10}Be fragment and a neutron. The solid curve is a fit to the experimental spectrum using response functions generated by GEANT Monte Carlo simulations. The inset shows a partial level scheme for ^{10}Be [116] indicating the observed transitions and the population after breakup. The energy of the levels is given in MeV. Right: dipole-strength distribution of ^{11}Be deduced from the measurement of the differential cross-section $\mathrm{d}\sigma/\mathrm{d}E^*$ for electromagnetic breakup yielding the ^{10}Be fragment in its ground state (filled symbols). The open symbols display the result obtained by Nakamura *et al.* [58] from a Coulomb breakup experiment at lower beam energies. In the latter case, excited-state contributions were not subtracted. The dashed and solid curves display the result of the direct-breakup model before and after convoluting with the instrumental response, respectively, and after multiplying by a spectroscopic factor of 0.61. The dotted curve results from a calculation using the plane-wave approximation. Reprinted with permission from Palit *et al.* [57], Copyright (2003) by the American Physical Society.

Similar to the eikonal calculation for the nuclear cross-sections, the Coulomb breakup cross-sections are calculated for individual single-particle ground-state configurations of the neutron with a relative-motion wave function $\phi_{n\ell j}(r)$ and corresponding core state (I_c^π). In general, more than one configuration can contribute, and the cross-section involving the core state (I_c^π) is calculated by summing over the respective configurations. In that case, the differential cross-section might be used to disentangle the different contributing ℓ values [60]. The associated spectroscopic factors $C^2S(I_c^\pi, n\ell j)$ are obtained experimentally by the ratio of the measured partial cross-sections for the population of core states (I_c^π) obtained from the γ coincidences, and the theoretical cross-section with unity spectroscopic factor. The final state $|\boldsymbol{q}\rangle$ in the continuum might be approximated by a plane wave [117,118]. The final-state interaction between the neutron and the core can be taken into account by using an appropriate optical potential with parameters taken from the literature.

As an example, the results obtained for the halo nucleus ^{11}Be [57] are shown in fig. 14. The γ-ray sum energy spectrum as recorded in coincidence with ^{10}Be fragments and a neutron (left panel) reveals contributions to the breakup cross-section involving the 2^+ first-excited state at 3.37 MeV but also higher-lying states of ^{10}Be at around 6 MeV excitation energy, very similar to the nuclear one-neutron removal reaction [69] and the transfer reaction [77] discussed in sects. 3.3 and 3.2, respectively. The high-energy transitions result from the removal of more deeply bound core neutrons from the p shell populating 1^- and 2^- states. The solid curve describing the measured spectrum results from a fit to the data involving response functions generated by Monte Carlo simulations for the observed transitions (as indicated in the partial level scheme shown as insert) and a low-energy background arising from atomic interactions in the target. After subtracting the excited-state contributions, the differential cross-sections $\mathrm{d}\sigma/\mathrm{d}E^*$ for ground-state transitions, *i.e.*, excitations solely related to the $2s_{1/2}\otimes^{10}\mathrm{Be}(0^+)$ halo state, are obtained.

After subtracting the nuclear contribution of the measured cross-section with the lead target, the dipole-strength distribution is derived from the resulting differential cross-section for electromagnetic excitation by dividing out the number of equivalent photons. The experimental dipole-strength function for transitions to the ^{10}Be ground state is shown in the right panel of fig. 14 (symbols). The result of the calculation with the direct-breakup model (eq. (6)) is displayed by the dotted and solid curves for the plane-wave and distorted-wave calculations, respectively. The distorted continuum waves were calculated with an optical potential adopting parameters from ref. [119]. The normalization of the theoretical curve was adjusted by multiplying by a spectroscopic factor of 0.61(5) as derived from the ratio of experimental to calculated cross-sections for electromagnetic breakup. First, we note a remarkable agreement of theory and experiment concerning the shape. Only minor differences can be observed in the peak region. The shape is not very sensitive to the optical potential used, as can be seen by the

comparison with the result for plane waves (dotted curve). The small dependence on the parameters used for the optical potential is incorporated in the error for the deduced spectroscopic factor of 0.61(5) for the halo neutron in the $2s_{1/2}$ orbital coupled to the 0^+ ground state of the ^{10}Be core. From the integrated dipole strength, a corresponding root-mean-square radius for the s neutron halo density distribution of 5.7(4) fm is deduced [57].

An independent extraction of the spectroscopic factor from the diffraction dissociation cross-section measured with a carbon target and an eikonal calculation for this cross-section yields an occupancy of 0.77(4) [57], in good agreement with the result of 0.87(13) deduced from the one-neutron removal cross-section measured at lower incident energy [69]. We note that the two results extracted from electromagnetic and nuclear breakup differ by 20%. The difference might reflect the systematic uncertainties inherent in the methods and models used. A theoretical model avoiding the choice of parameters for the optical potential, which are often uncertain in case of exotic nuclei, was recently developed by Typel and Baur [120]. In their effective-range approach the only free parameter is a reduced scattering length describing the core-neutron interaction, which can be deduced from a fit of the calculation to the measured differential cross-section. From the analysis of the data discussed above [57] they obtain a spectroscopic factor of 0.70(5) [120] in agreement with the shell-model prediction of 0.74 by Brown *et al.* [69], and also with the ones derived from the nuclear breakup discussed above.

The Coulomb breakup of $2n$ halo nuclei was measured for ^{11}Li [54–56], ^{6}He [53,121] and ^{8}He [122,123] exhibiting large dipole transition strength just above the threshold. The dipole-strength function as extracted from the electromagnetic excitation cross-section for 240 MeV/nucleon ^{6}He projectiles impinging on a lead target [53] is displayed in fig. 15 (solid curve). The experimental strength distribution is compared to results from three-body calculations of Danilin *et al.* [124] (dashed curve) and Cobis *et al.* [125] (dotted curve). The differences between the two theoretical results may reflect the different interactions being used. To which extent the dipole strength is of resonant origin is currently being investigated theoretically [124, 126,127]. Further investigations concerning the analysis of three-body correlations in the decay of ^{6}He after electromagnetic excitation [128] may give deeper insight into the characteristics of the three-body continuum excitations.

The integrated strength of the experimentally derived distribution (up to 5 MeV excitation energy) exhausts the energy-weighted (EW) Thomas-Reiche-Kuhn (TRK) sum rule $S_{\rm TRK}$ [129] to $(10 \pm 2)\%$ [53]. In a halo nucleus like ^{6}He, the most interesting comparison of the electromagnetic $E1$ strength function is provided by its relation to cluster sum rules [130–132]. This is connected with the fact that the main mode of motion at low energies only contains the α-particle and two neutrons.

The energy-weighted "cluster" sum rule [130,131] is obtained by splitting the strength of the dipole motion into that of the core, that of the halo nucleons, and that of the relative motion between core and halo. For a neutron halo, one obtains

$$S_{\rm clus}^{\rm EW} = \frac{9}{4\pi} \frac{N_h Z_c^2 e^2}{A A_c} \frac{\hbar^2}{2m} \tag{7}$$

or the ratio

$$\frac{S_{\rm clus}^{\rm EW}}{S_{\rm TRK}} = \frac{Z_c N_h}{A_c N}, \tag{8}$$

where indices c and h refer to core and halo, respectively. The $E1$ non–energy-weighted (NEW) cluster sum rule [133,134] (see also [135]) reads

$$S_{\rm clus}^{\rm NEW} = \frac{3}{4\pi} Z_c^2 e^2 \langle r_c^2 \rangle = \frac{3}{4\pi} Z_c^2 e^2 \left(\frac{N_h}{A_c} \right)^2 \langle r_h^2 \rangle \,, \tag{9}$$

where r_c (r_h) describes the distance between the center-of-mass of the core (halo neutrons) to that of the whole nucleus.

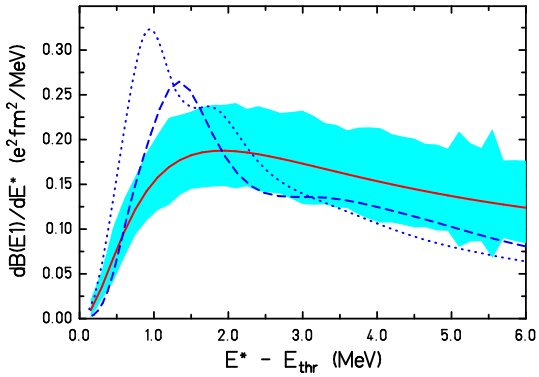

Fig. 15. Dipole-strength distribution in ^{6}He. The shaded area reflects the experimental result obtained from a Coulomb breakup experiment [53], the dashed and dotted curves display results from the three-body models of refs. [124] and [125], respectively. Figure reprinted with permission from Aumann *et al.* [53], Copyright (1999) by the American Physical Society.

The experimental energy-weighted $E1$ strength integrated up to 10 MeV excitation energy is very close to the cluster sum rule limit. The experimental value for the non–energy-weighted strength in the same energy interval amounts to 1.2(2) e^2fm^2 [53], from which by means of eq. (9) the r.m.s. values $\sqrt{\langle r_c^2 \rangle} = 1.12(13)$ fm and $\sqrt{\langle r_h^2 \rangle} = 2.24(26)$ fm were deduced. The deduced value for the root-mean-square distance between the α-particle and the two valence neutrons amounts to $r_{\alpha\text{-}2n} = 3.36(39)$ fm. The theoretical results from different three-body models (see table 3 in ref. [136]) give values for $r_{\alpha\text{-}2n}$ between 3.19 and 4.24 fm.

3.4 Applications to the spectroscopy of exotic nuclei

3.4.1 The $N = 8$ shell closure

Several experimental findings have shown that the shell closure at $N = 8$ vanishes for neutron-rich nuclei. This includes, *e.g.*, the fact that ^{11}Be has a $1/2^+$ ground state

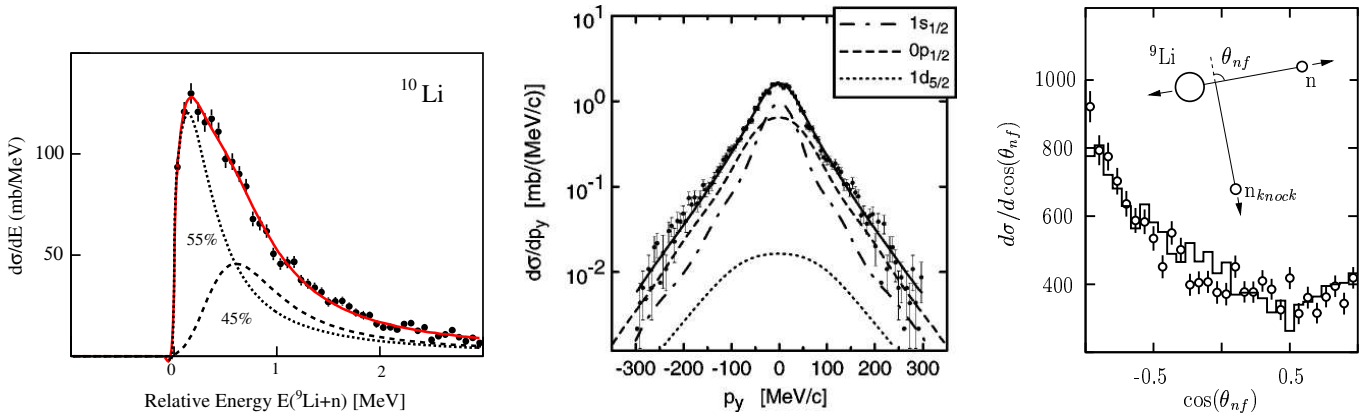

Fig. 16. One-neutron removal reaction from ^{11}Li (287 MeV/nucleon) on a C target measured with the LAND reaction setup at GSI [137,138]. The quantities shown are the ^{10}Li invariant-mass spectrum (left), the ^{10}Li transverse momentum distribution (middle), and the angular correlation in the decay of ^{10}Li (right). The spectra are explained by assuming a mixture of $(s_{1/2})^2$ and $(p_{3/2})^2$ configurations in the ^{11}Li ground state. Figures reproduced with permission from Simon *et al.* [137,138] (Copyright (1999) and (2004) by the American Physical Society and Elsevier, respectively) and Bertulani, Hansen [94] (Copyright (2004) by the American Physical Society).

("parity inversion") with the $p_{1/2}$ single-particle state close by at 320 keV excitation energy. A strong quadrupole deformation of ^{12}Be extracted from an inelastic proton scattering experiment exciting the 2^+ state was reported by Iwasaki *et al.* [139]. A low-lying 1^- intruder state observed in electromagnetic excitation of ^{12}Be [140] provides a consistent picture of the $N = 8$ shell melting. Here, the one-neutron removal reactions of the $N = 8$ nuclei ^{12}Be [68] and ^{11}Li [137] providing spectroscopic factors shall be discussed.

Navin *et al.* measured partial cross-sections for the reaction of a 78 MeV/nucleon ^{12}Be beam on a Be target populating ^{11}Be in its ground and first-excited state (see fig. 6). The momentum distribution recorded in coincidence with the γ-ray of 320 keV from the decay of the excited state in ^{11}Be has a shape characteristic for $\ell = 1$, while the distribution populating the ground state corresponds to a knockout of a neutron from the $(s_{1/2})^2$ configuration. From the partial cross-sections spectroscopic factors were deduced showing that the neutrons occupy the s and p configurations with similar weight. The sum of the spectroscopic factors, however, is close to unity, which leads the authors to the conclusion that the ground-state wave function of ^{12}Be has a strong d component in addition. This component could not directly be seen in the experiment because it involves unbound states of ^{11}Be, not observed in the experiment [68]. It is interesting to compare this result to the ^{11}Li case. Here the knockout reaction populates unbound states in ^{10}Li. The left frame in fig. 16 shows the ^{10}Li invariant-mass spectrum measured by Simon *et al.* [137,138] for a knockout reaction of a 287 MeV/nucleon ^{11}Li beam impinging on a carbon target. The spectrum can be described by assuming two states in ^{10}Li populated with about equal intensity corresponding to the knockout from the $(s_{1/2})^2$ or $(p_{3/2})^2$ components in ^{11}Li, respectively, in good agreement with a relativistic Hartree-Bogoliubov calculation [141]. The interpretation is evident from the transverse momentum distribution of ^{10}Li shown in the middle panel of fig. 16. A fit to the distribution yields $\ell = 0$ and $\ell = 1$ components with similar cross-sections [137]. Bertulani and Hansen [94] extracted corresponding relative spectroscopic factors of 33(2) and 64(5) for the two components, respectively. They also included a d component in the fit, which turns out to be very small (see fig. 16). The angular correlation shown in the right frame gives independent evidence for the s and p mixture in the ^{11}Li wave function: The distribution shows not only an anisotropic but also an asymmetric shape. The asymmetry has its origin in the interference between the two different decay paths populating different-parity states in ^{10}Li, the ground state (virtual s state) and excited states with $\ell = 1$. A similarly consistent picture can be derived from the ^{9}Li-n relative-energy spectrum (left panel), which can be described by assuming two states in ^{10}Li, a s state with scattering length $a_s > -40$ fm, and a p state at resonance energy $E_r = 0.68(19)$ MeV [138].

It is interesting to note that the spectroscopic factor for the $(d_{5/2})^2$ configuration is very small in the ^{11}Li case, see fig. 16. The authors of ref. [94] obtain from the fit shown in fig. 16 a contribution to the ^{11}Li ground-state wave function of 4(3)% only. This is very different from the finding for ^{12}Be and also at variance with the shell-model calculation of Brown predicting a strong admixture of $\ell = 2$ components in both cases [68]. The particle-vibration coupling model [142,143], however, is able to reproduce both experimental results, a mixture of s^2, p^2, d^2 components in ^{12}Be [143] in agreement with the experiment of ref. [68], and very little d^2 admixture in ^{11}Li, namely 2% [142] in accordance with the knockout experiment discussed above.

3.4.2 Continuum states: the first-excited state of ^{7}He

The coincident measurement of fragment and neutrons from the decay of continuum states allows the spectroscopy of unbound nuclei as already discussed in the context of knockout reactions with ^{6}He and ^{11}Li populating

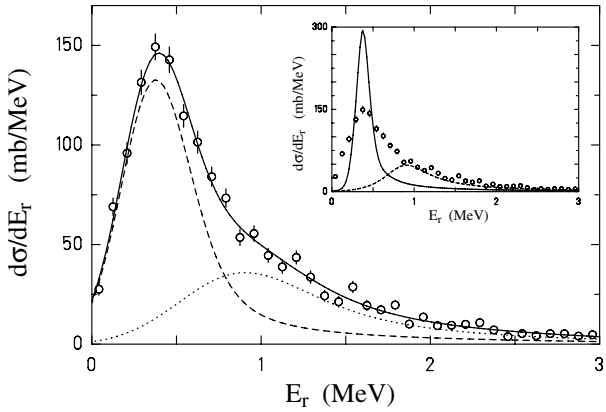

Fig. 17. Relative-energy spectrum of the ^{6}He-n system measured after breakup of a 227 MeV/nucleon ^{8}He beam in a carbon target. The spectrum is described by a fit (solid curve) assuming two resonances. The inset shows the results of the fit without the effect due to the experimental resolution. Figure reprinted with permission from Meister *et al.* [144], Copyright (2002) by the American Physical Society.

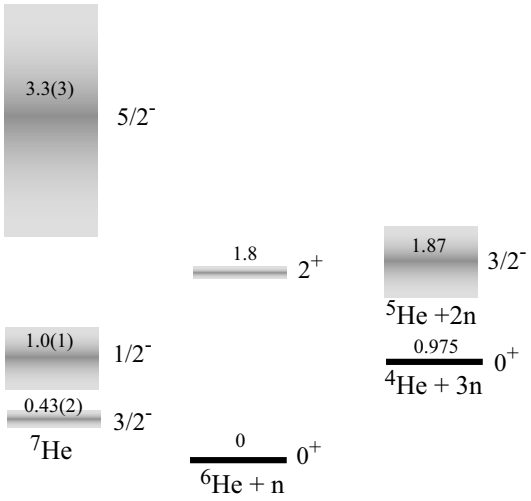

Fig. 18. Proposed level scheme of ^{7}He. Reprinted with permission from [144], Copyright (2002) by the American Physical Society.

states in ^{5}He and ^{10}Li, respectively. A similar experiment was performed at the LAND setup (fig. 7) utilizing a 227 MeV/nucleon ^{8}He beam to study states in the unbound nucleus ^{7}He after one-neutron knockout in a carbon target [144,145]. The ^{6}He-n relative-energy spectrum, shown in fig. 17, exhibits a narrow resonance at around 400 keV corresponding to the known $I^\pi = 3/2^-$ ground state of ^{7}He. The shape of the spectrum reveals an asymmetric shape towards higher excitation energies, which can be well described by a fit assuming a second resonance. The position and width of the ground state obtained from this fit is in agreement with the values from the literature [146].

The second state with resonance energy $E_r = 1.0(1)$ MeV and width $\Gamma = 0.75$ MeV is interpreted as the $p_{1/2}$ spin-orbit partner of the ground state, see the proposed level scheme displayed in fig. 18. This implies a rather small splitting of the $p_{3/2}$ and $p_{1/2}$ states of about 0.6 MeV, which should be compared to the lowest estimate of this energy difference in ^{5}He which is 1.2 MeV [147,148], thus a considerable decrease of the splitting of the two lowest states is found when adding two more neutrons. This reduction might partially be related to the fact that the spin-orbit force, which is proportional to $-(1/r)\mathrm{d}V/\mathrm{d}r$, becomes smaller due to the difference in size and diffuseness between ^{4}He and ^{6}He. The theoretical predictions for the position of the $1/2^-$ state relative to the ground state range from about 3 MeV within the shell-model approach [149] and the resonating group model [107], and 2.2 MeV in large-base shell-model calculations [150], to about 0.9 MeV in quantum Monte Carlo calculations [151] in fair agreement with the experiment. A Green's function Monte Carlo calculation [152] using, *e.g.*, the AV18/IL2 model [152] yields, however, a much larger splitting of 2.7 MeV. The inherent difficulty here is to calculate states in the continuum, in particular wide resonances like the first-excited state of ^{7}He. Recently, calculations within the "recoil-corrected continuum shell model" [153] have been performed for ^{7}He by Halderson [154] finding a splitting of 0.5–0.75 MeV and a width of 0.63 to 0.71 MeV in perfect agreement with the experiment discussed above. The same calculation can also explain the fact that the state was not observed in the experiment studying the ^{6}He(p,n) reaction [155] searching for the isobaric analog states of ^{7}He due to kinematical conditions.

3.4.3 Beyond the neutron dripline

The method of one-nucleon knockout populating continuum states as discussed in the previous section can also be applied to study states in unbound nuclei beyond the dripline. An example is the one-proton removal from ^{6}He populating states in ^{5}H. From the coincident measurement of the momenta of the triton and the two neutrons, the ^{5}H invariant mass E_{tnn} may be reconstructed [156]. The experimental spectrum resulting from the reaction of a 240 MeV/nucleon ^{6}He beam impinging on a carbon target is shown in fig. 19. A broad peak-like structure is observed at around 3 MeV, which is in good agreement with a three-body microscopic calculation [157] assuming a $t+n+n$ structure with a ground-state spin $I^\pi = 1/2^+$. The data have been further analyzed by inspecting the energy and angular correlations in the three-body decay of ^{5}H: The distributions are constructed for two different Jacobi coordinate systems and fitted by theoretical ones derived from a (truncated) series expansion of the final-state wave function into hyperspherical harmonics. From a simultaneous fit of energy and angular distributions in both Jacobi coordinate frames, the probability distributions $\mathcal{W}(\epsilon, \cos(\vartheta))$ are obtained [158]. Figure 20 shows the result for one Jacobi system as indicated in the inset. The n-n relative energy $\epsilon = E_{nn}/E_{tnn}$ is given in units of the total available kinetic energy E_{tnn} in the three-body system. The correlation function exhibits two maxima corresponding to the two configurations where the neutrons are

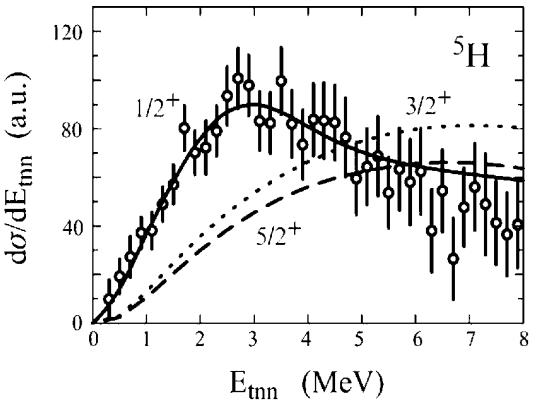

Fig. 19. Invariant-mass spectrum E_{tnn} constructed from the coincident measurement of triton and two neutrons after a one-proton knockout reaction of a 240 MeV/nucleon ^{6}He beam in a carbon target. The curves display microscopic three-body calculations [157] assuming different ground-state spins for ^{5}H as indicated. Reprinted from [156], Copyright (2003), with permission from Elsevier.

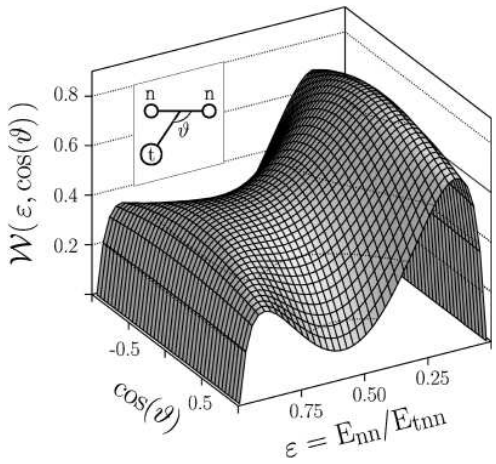

Fig. 20. Probability distribution $\mathcal{W}(\epsilon, \cos(\vartheta))$ with amplitudes resulting from a fit of a series expansion of the final-state wave function to the experimental correlation spectra. The inset sketches the used Jacobi coordinate system. Figure reprinted with permission from Meister *et al.* [158], Copyright (2003) by the American Physical Society.

close together ("di-neutron" configuration) and far apart from each other ("cigar-like" configuration), respectively.

Although the data discussed above seem to be consistent with a $I^\pi = 1/2^+$ ground state as predicted by the three-body model, the situation concerning the ground state of ^{5}H is not clear. The narrow resonance found in a ^{1}H(^{6}He,^{2}He)^{5}H transfer reaction [159] at around 2 MeV is not observed in the high-energy knockout experiment discussed above. The $t(t,p)^5$H reaction was studied by Golovkov *et al.* [160]. A broad structure has been identified above 2.5 MeV, which they interpret as a mixture of $3/2^+$ and $5/2^+$ states. The structure of the extremely neutron-rich nucleus ^{5}H thus remains puzzling, and more experimental investigations are called for.

3.4.4 The near-dripline nucleus ^{23}O and the $N = 14, 16$ shell closures

The heaviest nucleus located at the neutron dripline which has been produced so far is ^{24}O. Although most theoretical calculations predict the isotope ^{28}O to be bound due to its doubly magic character with neutron number $N = 20$, several experiments [161–164,28] have proven that the dripline is located at $N = 16$ for the chain of oxygen isotopes. This observation was interpreted as a weakening of the $N = 20$ shell [27,165,26,30,35,32] and (sub-)shell closures for the oxygen isotopes at neutron numbers $N = 14$ and $N = 16$. Support for such a shell closure came recently from a fragmentation experiment in which the 2^+ state in ^{24}O was not observed in the γ spectrum [166], which leads the authors to the conclusion that the first 2^+ state should have a rather high excitation energy above the neutron threshold of 2.7 MeV. Another interesting observation concerns the large interaction cross-section measured for ^{24}O [18] suggesting a halo-like structure [18]. Kanungo *et al.* proposed in ref. [167] a core enlargement and in ref. [168] a change of the level ordering implying a $(d_{5/2})^{-1}(s_{1/2})^2$ structure of ^{23}O in order to explain this large cross-section. This interpretation caused a controversial discussion and was called into question by Brown *et al.* [169]. Inclusive breakup data [168] are in agreement which such an assumption, while a more conventional shell-model ordering of single-particle levels cannot be excluded, though.

Very recently, two exclusive experiments were performed at GSI investigating the one-neutron removal by nuclear and Coulomb breakup, respectively. Figure 21 displays the results from the nuclear knockout reaction [170], which is a well-established tool for studying the valence-nucleon single-particle configuration of exotic nuclei, as discussed in sect. 3.3. The $A-1$ fragment ^{22}O is momentum analyzed in the Fragment Separator FRS in coincidence with γ-rays identifying the states populated. The resulting Doppler-corrected γ-ray spectrum is shown in the left frame of fig. 21. Several excited states are populated as indicated in the level scheme shown in the inset. About 40% of the cross-section leads to excited states. The right frame of fig. 21 shows the longitudinal momentum distributions, the inclusive one in the left part, and separately for ground and excited states on the right. The distribution populating excited states is much wider than the one for ground-state transitions, in agreement with the assumption that the excited states are associated with the removal of a neutron from a $d_{5/2}$ state, while the ground-state distribution is in much better agreement with a calculation assuming a $\ell = 0$ neutron [170]. From the one-neutron removal cross-section of ^{23}O yielding ^{22}O in its ground state, a spectroscopic factor $S = 0.97(19)$ was extracted for the $2s_{1/2}\otimes^{22}\mathrm{O}(0^+)$ single-particle configuration by comparison with theoretical Glauber calculations in eikonal approximation [170].

A complementary experiment investigating the electromagnetically induced one-neutron removal has been performed with the LAND reaction setup. The method of utilizing Coulomb breakup as a spectroscopic tool similar

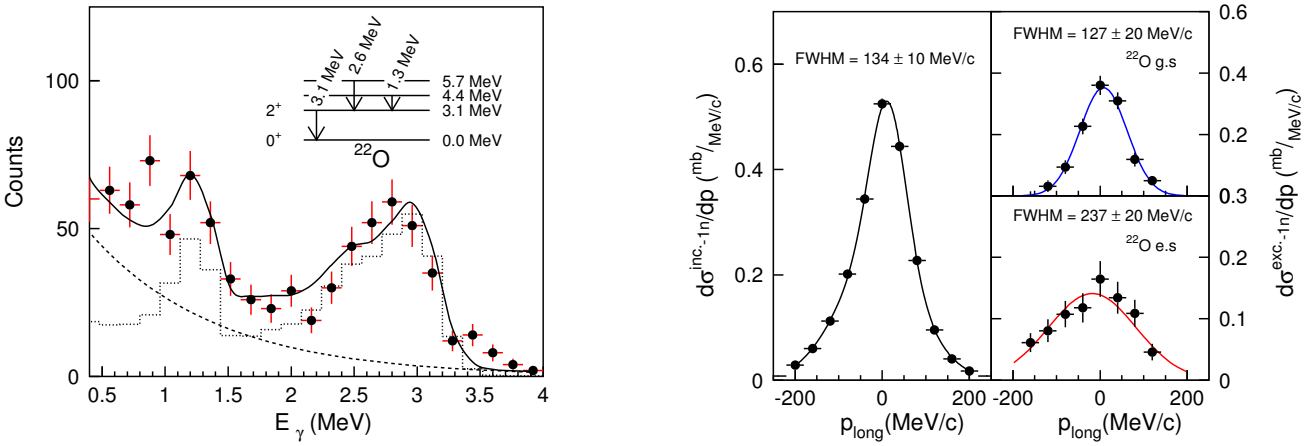

Fig. 21. One-neutron knockout reaction from ^{23}O at 938 MeV/nucleon in a carbon target. Left: Doppler-corrected γ spectrum measured in coincidence with ^{22}O fragments. Right: parallel momentum distributions (in the rest frame of the projectile) of the ^{22}O fragments. The right two panels display the distributions differentiated according to the final state populated, for ground and excited states in the upper and lower rightmost frames, respectively. Figure reprinted with permssion from Cortina-Gil *et al.* [170], Copyright (2004) by the American Physical Society.

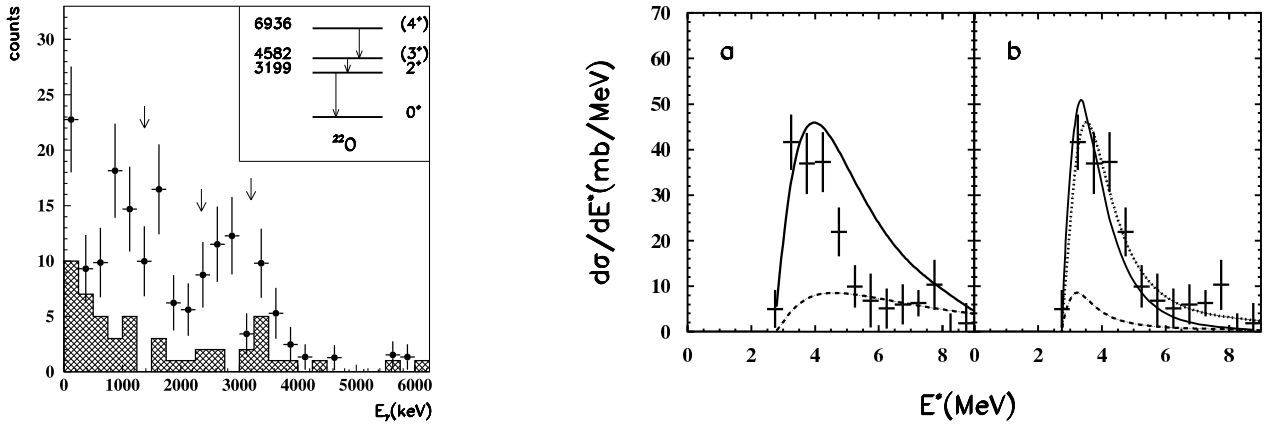

Fig. 22. Coulomb breakup of a 422 MeV/nucleon ^{23}O beam in a lead target. Left: Doppler-corrected γ spectrum recorded in coincidence with ^{22}O fragments and one neutron. The shaded histogram is measured with a carbon target and reflects the nuclear contribution (if scaled) to the spectrum for the lead target (symbols). The arrows indicate the strongest γ transitions as expected from the ^{22}O level scheme (shown in the inset). Right: differential cross-section $\mathrm{d}\sigma/\mathrm{d}E^*$ for electromagnetically induced breakup. The data (error bars) are compared to different calculations assuming ground-state spins of $1/2^+$ (solid and dotted curves) and $5/2^+$ (dashed curves) in a plane-wave approximation (panel a) and for calculations taking into account final-state interaction (panel b) by using an optical potential (solid and dashed) or the effective-range approach (dotted curve). Reprinted from Nociforo *et al.* [62], Copyright (2005), with permission from Elsevier.

to the nuclear one-neutron removal reaction was established recently in studies of the halo nucleus ^{11}Be [57] and the neutron-rich carbon isotopes ^{15,17}C [60]. Here, the method is applied to the case of ^{23}O discussed above. The differential cross-section for electromagnetic excitation has been derived from a kinematically complete measurement of the breakup of a 422 MeV/nucleon ^{23}O beam impinging on a lead target [62]. The Doppler-corrected γ spectrum in coincidence with ^{22}O fragments is shown in the left frame of fig. 22 for measurements with carbon (shaded area) and lead (symbols) targets.

Although the γ spectrum looks similar to the one shown in fig. 21 for the nuclear breakup, only a small fraction of the cross-section populates excited states, which can be mainly attributed to nuclear breakup. This is due to the selectivity of the electromagnetic process for the asymptotic part of the wave function yielding enhanced transition probabilities for large core-neutron distances, *i.e.*, for $\ell = 0$ states [57]. The extracted differential cross-section $\mathrm{d}\sigma/\mathrm{d}E^*$ is compared to model calculations in the right panels of fig. 22. The cross-section distribution is characterized by a sharp rise just above the neutron emission threshold, which can only be reproduced by the calculation assuming a s-wave neutron (solid and dotted curves), while the result from the calculation assuming a $d_{5/2}$ neutron is much broader (dashed curves). The plane-wave calculation (panel a), however, fails to reproduce the data. Calculations taking into account the final-state interaction by an optical potential (solid and dashed curves in panel b) or within the effective-range

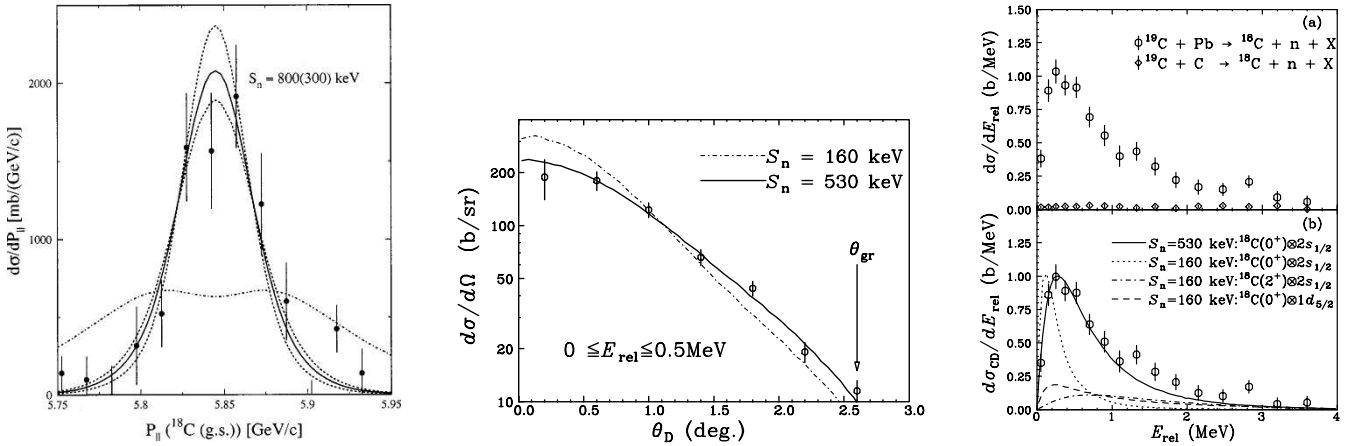

Fig. 23. Breakup of ^{19}C. Left: parallel momentum distribution of ^{18}C measured with the S800 spectrograph after one-neutron removal from 57 MeV/nucleon ^{19}C projectiles in a beryllium target [63]. The curves show calculations assuming knockout from a s state (solid and dotted) and from a d state (dash-dotted). Dotted and solid curves assume different separation energies, the best fit is obtained for S_n = 800 keV (solid curve). From Maddalena *et al.* [63]. The right two panels show results from Coulomb breakup of ^{19}C at 67 MeV/nucleon impinging on a lead target [61]. Middle frame: cross-section as a function of the scattering angle for the low-energy part of the spectrum (see right frame). The large sensitivity of the angular distribution on the separation energy for low relative energies is indicated by the dash-dotted and solid curves. The lower right panel shows a comparison of the experimental relative-energy spectrum to different calculations. Reproduced with permission from Nakamura *et al.* [61]. Copyright (1999, 2001) by the American Physical Society.

approach [120] (dotted curve) reproduce the data very well if again a $2s_{1/2}\otimes^{22}\mathrm{O}(0^+)$ configuration is assumed. The two different approaches yield consistent spectroscopic factors of 0.78(13) and 0.77(10), respectively, which are in good agreement with a recent shell-model prediction of 0.80 [32]. Since the cross-section is associated with transitions to the 0^+ ground state of ^{22}O and the angular momentum $\ell = 0$ is determined by the shape of the differential cross-section, the ground-state spin $I^\pi = 1/2^+$ of ^{23}O is uniquely determined as well.

In summary, both experiments, the nuclear knockout reaction and the Coulomb breakup, provide a consistent picture of the ground-state structure of ^{23}O with a spin assignment $I^\pi = 1/2^+$. A $(d_{5/2})^{-1}(s_{1/2})^2$ structure as suggested earlier in ref. [168] can be excluded. Moreover, the large spectroscopic factors for the $2s_{1/2}\otimes^{22}\mathrm{O}(0^+)$ configuration obtained in both approaches give further support for a shell gap at neutron number $N = 16$ within the chain of oxygen isotopes.

3.5 Discussion

3.5.1 Nuclear versus electromagnetic breakup

Both nuclear and electromagnetic neutron removal reactions were applied at energies ranging from 50 MeV/nucleon to about 1 GeV/nucleon and spectroscopic information on exotic nuclei was deduced even for beams with low intensity. For loosely bound nuclei, the cross-sections become large and thick targets may be used (up to 1 g/cm^2 at high beam energies). Figure 23 shows two impressive examples: The left frame shows the momentum distribution measured by Maddalena *et al.* [63] with the S800 spectrometer (see fig. 5) after breakup of a ^{19}C beam at 57 MeV/nucleon on a beryllium target. From the momentum distribution, which was corrected for contributions from excited levels by means of γ coincidence measurements, and the corresponding cross-section it can be concluded that the valence neutron is dominantly bound in a s state coupled to the ground state of ^{18}C implying a ground-state spin $I^\pi = 1/2^+$. This result was obtained with a beam intensity of around 1 ion/s only. The results obtained at RIKEN by Nakamura *et al.* [61] for the Coulomb breakup of 67 MeV/nucleon ^{19}C projectiles impinging on a lead target are also shown in fig. 23. They were taken with a beam intensity of 300 ions/s [61] again demonstrating the high sensitivity of the reaction. The differential cross-sections as a function of scattering angle and core-n relative energy are shown in the middle and right frames, respectively. From the angular distribution, the neutron separation energy of 530(130) keV was extracted [61] (see solid and dash-dotted curves) providing the presently most precise measurement of the ^{19}C mass. The relative-energy spectrum (right frame) can be well described assuming the removed neutron to be bound in a s state with the separation energy as extracted from the angular distribution. From the cross-section, a spectroscopic factor 0.67 was extracted [61], which is in good agreement with the value of 0.91(31) derived from the nuclear reaction discussed above (the theoretical single-particle cross-section given in ref. [63] of 136 mb for S_n = 0.8 MeV was scaled to 163 mb for a neutron separation energy of 530 keV in order to be consistent with the Coulomb breakup data). Although the Coulomb breakup experiment [61] did not measure γ coincidences, the influence of excited-state contributions should be small since the electromagnetic process is mainly sensitive to the s state.

The sensitivity of the Coulomb breakup reaction is demonstrated in fig. 24. There, the differential cross-section for electromagnetic breakup of ^{17}O [171] (squares)

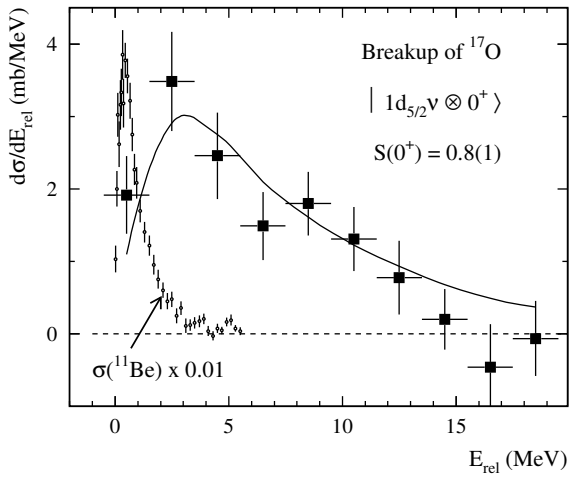

Fig. 24. Differential cross-sections $\mathrm{d}\sigma/\mathrm{d}E_{\mathrm{rel}}$ as a function of the relative energy between $^{16}\mathrm{O}(0^+)$ and the neutron for Coulomb breakup of ^{17}O populating the ground state of ^{16}O. The shape of the experimental spectrum (squares) is well reproduced by a plane-wave calculation for a $1d_{5/2}$ neutron coupled to the ^{16}O ground state with a spectroscopic factor 0.8 (solid curve). For comparison, the cross-section obtained for ^{11}Be Coulomb breakup (multiplied by 0.01) is shown by the circles. Reprinted from [171], Copyright (2004), with permission from Elsevier.

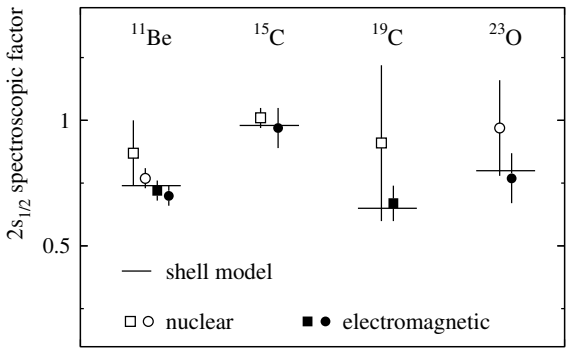

Fig. 25. Spectroscopic factors of the $2s_{1/2} \otimes \mathrm{core}(0^+)$ halo states derived from different reactions. Squares (circles) refer to data taken in the energy regime 50–100 MeV/nucleon (0.4–1 GeV/nucleon). The data are taken from refs. [69,57, 59,120] (^{11}Be), refs. [173,60] (^{15}C), refs. [63,61] (^{19}C), and refs. [170,62] (^{23}O).

is compared to the one obtained for the halo nucleus ^{11}Be [57] (divided by a factor of 100, circles). The fact that the valence neutron of ^{17}O is well bound in a $l = 2$ state, while ^{11}Be has a well-pronounced $\ell = 0$ halo structure, results in a cross-section distribution which is two orders of magnitude smaller in the peak, and much broader. This makes the electromagnetic breakup particularly interesting to study loosely bound systems close to the dripline where the production rates are small. For well-bound states the cross-sections become smaller and the nuclear contribution has to be treated very carefully. The dependence of the nuclear one-neutron removal cross-section on the separation energy and ℓ value is less pronounced, and makes the method more generally applicable. It is interesting to note, however, that the differential cross-section for ^{17}O can be well described by the direct-breakup model within the plane-wave approach as shown by the solid curve in fig. 24. A preliminary analysis of the data by Palit *et al.* [171] results in a spectroscopic factor of 0.8(1) in agreement with the result from an electron scattering experiment of $S = 1.04(10)$ [172].

The question arises of how precise spectroscopic factors deduced from reactions with secondary beams are. In the previous sections, examples were discussed where spectroscopic factors were deduced by different types of reactions studied at different beam energies. A comparison of those results might help in judging derived spectroscopic factors in terms of absolute occupation probabilities, since the uncertainties related to the description of the reaction mechanisms depend on the type of reaction and the beam energy.

Figure 25 summarizes the results obtained for the $2s_{1/2}$ spectroscopic factors for various one-neutron halo nuclei. Included are spectroscopic factors derived from nuclear breakup (open symbols) as well as from electromagnetic induced breakup (filled symbols). The data are further differentiated according to the beam energy: reactions in the energy range of 50–100 MeV/nucleon are depicted as squares, circles show the results from reactions performed at higher energies (400–1000 MeV/nucleon). The shell-model predictions by Brown [69,63,32] are indicated by the solid lines. For this comparison, always the latest measurement and/or analysis was taken from the literature. First it is noted that the values extracted from different reactions at different energies are consistent without showing a clear tendency of systematic differences; although the values derived from Coulomb breakup are always slightly lower, they all overlap within errors with the data from nuclear breakup.

An estimate of the model dependence of the extracted values may be obtained from a comparison of different theoretical treatments in calculating the cross-sections. In case of Coulomb breakup, an important ingredient of the calculation is the treatment of the final-state interaction between the neutron and the core at low relative energies. This can be accounted for by the distorted-wave approach making use of optical potentials for the n-core interaction. Systematic sets of parameters for such potentials have been developed and are available for stable nuclei [119,174]. Even considering symmetry terms in the potential [174] makes the extrapolation to neutron-rich weakly bound nuclei uncertain, a problem very similar to the analysis of transfer reactions. For the Coulomb breakup of ^{11}Be, *e.g.*, a spectroscopic factor of 0.61(5) for the $2s_{1/2}\otimes^{10}\mathrm{Be}(0^+)$ single-particle configuration has been extracted by applying a distorted-wave analysis [57]. Although the shape of the dipole-strength function does not depend much on the optical potential used in case of halo nuclei [57], the absolute strength can be significantly influenced in particular if resonances are close by. In case of ^{11}Be, it is the bound p state. Very recently,

Typel and Baur [120] have developed a new approach to account for the final-state interaction in Coulomb breakup avoiding the above complications. In their effective-range approach, the n-core interaction in the continuum is taken into account by a reduced scattering length, which can be adjusted to reproduce the shape of the experimental transition probability. From a fit to the data of ref. [57], they obtain a spectroscopic factor of 0.70(5) (shown as a filled circle), about 15% larger than the result using the optical potential of ref. [119]. The reduced scattering length obtained from the fit is very large as expected from the existence of the weakly bound $1/2^-$ excited state [120]. The resulting spectroscopic factor is in agreement with the results obtained for Coulomb breakup at lower energies by Fukuda *et al.* [59] (filled squares), as well as with the values derived from nuclear diffractive breakup at 500 MeV/nucleon [57] (open circles) and from the nuclear one-neutron removal at lower incident energy by Aumann *et al.* [69] (open squares). All values are consistent within the range of spectroscopic factors of 0.36 to 0.80 deduced from transfer reactions, see the compilations given in refs. [57,78].

Besides the cases of ^{11}Be, ^{19}C, and ^{23}O discussed already in the previous subsections, ^{15}C is included in fig. 25 for which exclusive data exist for both nuclear [85,173] and electromagnetic breakup [60], the latter being discussed in connection with its astrophysical implications in sect. 5. The ground-state wave function of ^{15}C is dominated by a $2s_{1/2}$ configuration with a spectroscopic factor close to unity (see fig. 25), which causes in conjunction with the small neutron separation energy of only 1.22 MeV a well-developed neutron halo. Different theoretical approaches to the nuclear one-neutron breakup were studied by Tostevin *et al.* [85]. They calculate cross-sections based on the eikonal model using effective nucleon-nucleon interactions and Gaussian density distributions for the core and target as described in ref. [84] and using instead the effective nucleon-nucleus interaction of Jeukenne, Lejeune, and Mahaux [175] (JLM). Alternatively, they calculated the diffraction cross-section within a coupled discretized continuum channels approach. The spectroscopic factors deduced by the different approaches are consistent with each other within 20% for the ^{15}C case [85]. It should be noted that this small uncertainty is mainly related to the treatment of the diffractive cross-section, which can be reliably calculated for higher beam energies, where the process can be described by the (purely) imaginary forward scattering amplitude. The value of $S = 1.01(4)$ given in fig. 25 is the result from a measurement at 103 MeV/nucleon by Terry *et al.* [173]. Spectroscopic factors for the $2s$ single-particle state in ^{15}C were also extracted from (d,p) transfer reactions using enriched radioactive ^{14}C targets [176–178] ranging from 0.76 to 1.03 depending on the model analysis. The values from the reactions discussed above are in agreement with this result.

In conclusion, the spectroscopic factors derived from nuclear and Coulomb breakup reactions are consistent with each other and are also in agreement with the results from transfer reactions within the experimental and model uncertainties. Both methods can be applied to low-intensity radioactive beams. The different model analyses yield spectroscopic factors which typically vary by 10 to 20%, which may be taken as an estimate for the systematic uncertainty of the model analyses.

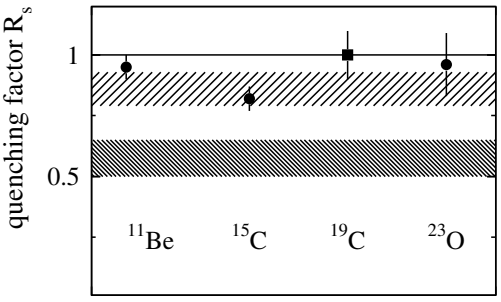

Fig. 26. Reduction factors R_s obtained from electromagnetic induced breakup of halo nuclei. See text.

3.5.2 Absolute single-particle occupancies

The second striking observation is that the experimentally deduced spectroscopic factors are rather close to the shell-model predictions as can be seen in fig. 25. The Warburton-Brown [179] shell-model values of 0.74, 0.98, 0.65, and 0.80 for the nuclei ^{11}Be, ^{15,19}C, and ^{23}O (solid lines in fig. 25) are taken from refs. [69,85,63,169], respectively. A center-of-mass correction of the shell-model spectroscopic factors as proposed, *e.g.*, in ref. [180] was applied. Absolute spectroscopic factors derived from nuclear knockout reactions were discussed in terms of single-particle occupancies by Brown *et al.* [180] and Enders *et al.* [181]. They selected cases where several experimental cross-sections at high energy are available and the nuclear structure is believed to be well understood, *e.g.*, ^{12}C and ^{16}O, but also the one-proton halo nucleus ^{8}B. Since the reduction in single-particle occupancies due to long-range correlations is included in the shell-model spectroscopic factors, the ratio of measured to theoretical spectroscopic factors defined as the quenching factor $R_s = S^{\rm exp}/S^{\rm th}$ might be a measure of the effects related to short-range correlations. For the stable nuclei, they find quenching factors in the range 0.5–0.65 in good agreement with those derived from $(e,e'p)$ reactions [182]. In contrast, for the one-proton halo nucleus ^{8}B, a value of 0.86(7) [181] much closer to unity was derived. In fig. 26 such quenching factors are summarized for the cases discussed above as derived from the electromagnetically induced neutron removal reaction. The three filled circles are from the high-energy data measured at GSI [57,60,62]. If available (^{11}Be, ^{23}O) the theoretical values calculated within the effective-range approach of Typel and Baur [120] were used, which we consider to give the most precise cross-sections. The square refers to the RIKEN ^{19}C measurement of Nakamura *et al.* [61]. For all four one-neutron halo nuclei, the quenching factors are close to unity having a similar value as reported for ^{8}B (indicated by the less dense hatched

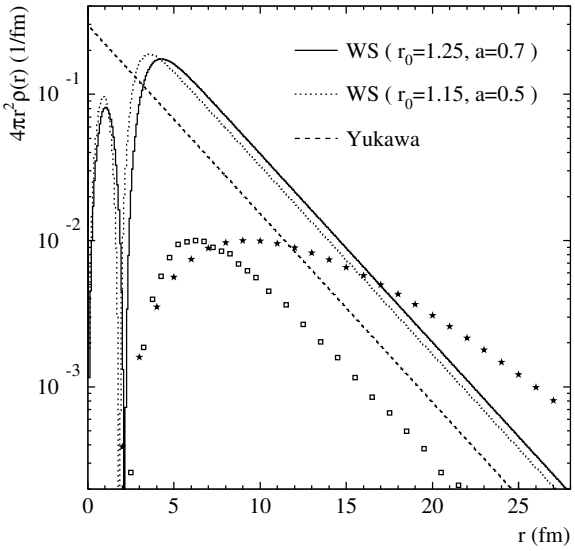

Fig. 27. Density distributions of the $2s_{1/2}$ halo neutron as a function of the neutron-core relative distance, calculated for two Woods-Saxon geometries (solid and dotted curves) and the Yukawa wave function (dashed line). The open squares and stars indicate the region of the density distribution contributing to the breakup reaction induced by nuclear diffraction or Coulomb breakup, respectively. The two breakup probabilities are given in arbitrary units. Reprinted with permission from [57], Copyright (2003) by the American Physical Society.

area) and lie well above the typical value observed for stable nuclei (dense hatched area). The spectroscopic factors derived from the Coulomb breakup thus corroborate the conclusion of Brown *et al.* [180] that the quenching factor is not universal for all nuclei and that in particular halo states approach the limit of $R_s = 1$.

The interpretation of spectroscopic factors as absolute single-particle occupancies as discussed by Brown *et al.* and briefly sketched in the previous paragraph implies an extrapolation of the wave function to the interior part of the nucleus. Both reactions, the nuclear as well as the electromagnetic nucleon removal, sample the wave function at the surface only. This is illustrated in fig. 27, where the density distribution of the s-wave halo neutron in ^{11}Be is displayed. The open squares and the stars indicate the sensitivity of the nuclear and electromagnetic breakup reactions, respectively. The nuclear breakup probability follows the decay of the halo wave function at large relative distances r and drops for smaller r values corresponding also to smaller impact parameters (due to the short-range interaction of the nuclear force, see also fig. 10) when reactions of the target with the core start to become dominant. In case of the Coulomb breakup, the sensitivity to the outer part of the wave function is not related to the impact parameter dependence of the reaction (see fig. 10) but originates from the nature of the dipole transition operator, see eq. (6): In the case of a plane-wave approximation, the dipole-strength function corresponds to a Fourier transformation of the wave function multiplied by the relative distance r. An assumption of the core density distribution, which has to be explicitly taken into account in the calculation for the nuclear breakup to account for the absorption, is not necessary in case of Coulomb breakup. Since both reactions measure the asymptotic normalization of the wave function, the spectroscopic factors depend somewhat on the choice of calculating the single-particle wave function. This is illustrated in fig. 27, where two density distributions are shown, both calculated using Woods-Saxon potentials but with different geometries as indicated in the figure. The "standard" parameters used for the extracted spectroscopic factors in the discussions above were diffuseness $a = 0.7$ and radius $r_0 = 1.25$ (solid curve). A calculation based on the wave function displayed as the dotted line ($a = 0.5, r_0 = 1.15$) would increase the spectroscopic factors deduced from nuclear and electromagnetic breakup, *e.g.*, for the case of ^{11}Be, by 13% and 18%, respectively. Tostevin *et al.* used alternatively a single-particle wave function derived from a Hartree-Fock calculation for ^{15}C yielding a spectroscopic factor being about 20% larger than that obtained using the Woods-Saxon potential with the "standard" [39] geometry ($a = 0.7$, $r_0 = 1.25$).

The necessity of an extrapolation of the wave function thus introduces an uncertainty in the order of 10–20% to the extracted single-particle occupancies. This uncertainty, however, may be further reduced by combining the knowledge from different reactions like, *e.g.*, Coulomb and nuclear breakup, total reaction cross-sections, or elastic scattering. A systematic study of single-particle occupancies in exotic nuclei using the above discussed approaches seems thus very promising. An alternative approach is discussed in the next section.

3.5.3 Perspectives: quasi-free scattering

The ideal reaction to overcome the limitations arising from the surface localization as discussed above is the electron-induced knockout. From such $(e, e'p)$ reactions spectral functions and absolute single-particle occupancies were deduced for stable nuclei [182]. At present, such reactions are not feasible with unstable exotic nuclei. At the future FAIR facility [183], however, electron scattering experiments are planned with short-lived nuclei by means of intersecting electron and heavy-ion storage rings [184]. An alternative approach, which is foreseen to be implemented in the near future at the LAND reaction setup at GSI (fig. 7), is the quasi-free scattering off protons in inverse kinematics using a liquid-hydrogen target and a recoil tracking detector. In case of electrons, the nucleus is transparent for the incoming and outgoing electron and effects due to absorption have only to be taken into account for the outgoing knocked-out nucleon. In order to approach a similar situation in quasi-free scattering, where the incoming and the two outgoing nucleons have to be considered, the beam energy has to be chosen such that all nucleons have energies where the nucleon-nucleon cross-section is minimal. Since this cross-section drops rapidly with increasing energy up to a minimum at about 250 MeV and then rises slowly, a beam energy

of around 700 MeV/nucleon seems ideal since both outgoing nucleons will have energies in the range of 200 to 400 MeV in a wide angular range. Apart from minimizing the effects due to secondary reactions, the inverse kinematics has the advantage that the information on binding energy and intrinsic momentum of the bound nucleon can be measured redundantly: firstly by a reconstruction from the measured angles and energies of both outgoing nucleons, and secondly from a precise measurement of the heavy recoil and coincident γ-rays (similar to the nuclear one-neutron removal reaction using extended targets as discussed previously). It is believed that this further characterization of the final state gives a better handle on the issue of final-state interactions compared to the measurements in normal kinematics, and that such experiments will not only allow to study short-lived nuclei, but also improve the situation significantly for stable beams. Due to the surface localization of the knockout reaction using extended targets, the sensitivity to deeply bound states is rather limited, although first experiments have been performed [185]. With the $(p, 2p)$-type quasi-free–scattering reaction, also deeply bound states can be probed, *i.e.*, the binding energies of proton states in loosely bound neutron-rich nuclei could be tested. First experiments of this kind are planned for the near future [186]. Another interesting aspect which can be studied by such reactions is the cluster structure in nuclei. A first experiment was recently performed at GSI utilizing ^{6,8}He beams at around 700 MeV impinging on a liquid-hydrogen target [187]. It has been demonstrated by Chulkov *et al.* [187] that from a kinematically complete measurement, it is possible to characterize the different knockout processes (in case of ^{6}He the knockout of a neutron or the α core) and deduce spectroscopic factors. In case of α knockout from ^{6}He, for instance, Chulkov *et al.* obtain an alpha spectroscopic factor close to unity [187], as expected from the $\alpha + n + n$ three-body structure of ^{6}He.

4 Inelastic excitations

4.1 Electromagnetic scattering

4.1.1 Electromagnetic excitation at relativistic energies

In peripheral heavy-ion collisions at energies of the order of 1 GeV/nucleon, collective nuclear states at low and at high excitation energies are excited with large cross-sections. Due to the high velocity and due to the Lorentz contraction the mutual electromagnetic field contains high frequencies up to several tens of MeV/$\hbar$, and is of transverse nature. A measure of the maximum excitation energy is the "adiabatic cutoff",

$$E_{\max} = \frac{\hbar}{\tau} = \frac{\hbar c \gamma \beta}{b} \qquad (10)$$

with γ, β being the relativistic Lorentz factor and the velocity, respectively, and b the impact parameter. With a typical minimum impact parameter of $b_{\min} = 14$ fm

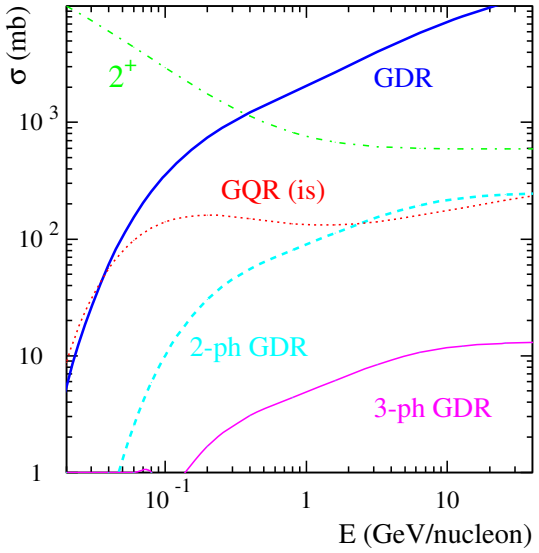

Fig. 28. Cross-sections for electromagnetic excitation of different collective states as a function of beam energy as calculated semiclassically adopting typical nuclear-structure parameters for a medium-mass nucleus impinging on ^{208}Pb.

for a medium heavy nucleus impinging on a lead target, 25 MeV and 6.6 MeV are estimated as maximum excitation energies for beam energies of 1 GeV/nucleon and 100 MeV/nucleon, respectively. Rotational states, surface vibrations and giant resonances can be studied even with moderate beam intensities. The short interaction time, however, suppresses multi-step excitations, so that only the lowest members of a rotational band are excited. Figure 28 gives typical cross-sections for the excitation of collective nuclear states in exotic nuclei on a lead target as a function of beam energy. The cross-sections allow experiments with minimum beam intensities of 1 to 1000 ions/s, provided efficient devices for γ-ray detection (discrete states) or particle detection (giant resonances) are implemented.

As can be seen from fig. 28, the excitation to the giant dipole resonance (GDR) becomes dominant for higher energies around 1 GeV/nucleon reaching cross-sections in the order of 1 b. In the energy range around 100 MeV/nucleon, the first 2^+ rotational state is very effectively excited. The high cross-sections in conjunction with thick targets make it possible to extract $B(E2)$ values with fragmentation beams down to intensities of few particles per second. Measurements at beam energies around 250 MeV/nucleon have been performed at GSI [188], most of the experiments, however, were performed at lower energies around 50 MeV/nucleon at RIKEN, GANIL and MSU, see the review of Glasmacher [189].

The electromagnetic excitation of the giant dipole resonance induced by high-energy beams on targets of high nuclear charge was studied in a series of experiments exploring the multi-phonon states of the dipole resonance, see the review of Aumann *et al.* [41], and refs. [190,191] for recent results. Due to the large excitation probability reaching around 20 to 30% for heavy nuclei at grazing impact,

two-step excitations of the second phonon of the GDR vibration (2-ph GDR) become possible with relatively large cross-sections, see fig. 28. The measurements with stable nuclei also have demonstrated that the (γ, n) cross-section and thus the $B(E1)$ strength distribution can be reliably extracted from the measured cross-sections [41]. It was also shown that the only free parameter entering into the semiclassical calculations [192,113], the minimum impact parameter $b_{\min}$, is well determined from systematics [115, 193]. Alternatively, the calculation can be combined with an eikonal calculation using realistic density distributions, which describes the nuclear absorption and replaces the sharp cutoff (see ref. [115] and fig. 10 for an example). This method can be readily extended to secondary beams of exotic nuclei, and a first measurement of dipole strength in exotic nuclei was performed at GSI recently [52], which will be discussed in the next section.

4.1.2 The dipole response of neutron-rich nuclei

The evolution of the dipole-strength distribution as a function of neutron-to-proton ratio was investigated systematically for the oxygen isotope chain ranging from a neutron excess of $N - Z = 1$ up to $N - Z = 7$. ^{16}O is a strongly bound doubly magic nucleus with a neutron separation energy $S_n = 16$ MeV, while, for the heavier isotopes, the separation energies decrease to $S_n \approx 7$ MeV for the even isotopes with $A = 18$ to 22, and $S_n \approx 4$ MeV for the odd isotopes. Thus, one may expect a decoupling of the valence neutrons from the inert ^{16}O core and the appearance of a collective soft-dipole excitation.

The neutron decay channels after electromagnetic scattering on a lead target at about 600 MeV/nucleon beam energy were investigated. From the coincident detection of charged fragments, neutrons, and gamma-rays, the differential cross-sections $\mathrm{d}\sigma/\mathrm{d}E^*$ were deduced by utilizing the invariant-mass method. The nuclear contribution to the cross-section was determined from a measurement with a carbon target and subtracted to obtain the differential cross-sections for electromagnetic excitation. Figure 29 displays the result [52] for the stable isotope ^{18}O, which was obtained in an experiment under the same conditions as for the radioactive nuclei. The ^{18}O beam with an energy of around 600 MeV/nucleon was produced at the FRS as a secondary beam from fragmentation of a ^{40}Ar primary beam delivered by the SIS. The extracted differential cross-section is compared to the cross-section obtained from photoabsorption measurements after converting to the electromagnetic excitation cross-section by applying semiclassical calculations [113] (grey curve in fig. 29) and after taking into account the experimental response (dashed and solid curves). The results derived from the measurements with real and virtual photons are in good agreement, both concerning the spectral shape and the absolute magnitude.

Figure 30 shows the (γ, n) cross-section for the unstable isotopes ^{20,22}O (left panels) in comparison with that for the stable nucleus ^{16}O [194] (solid curve overlaid to the cross-section for ^{20}O). Evidently, the dipole response

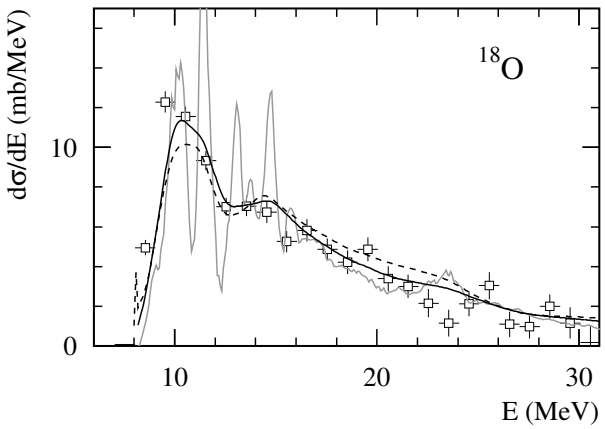

Fig. 29. Differential cross-section for electromagnetic excitation of ^{18}O projectiles impinging with about 600 MeV kinetic energy on a Pb target (symbols). The data are compared with cross-sections resulting from photoabsorption measurements [195] before (grey curve) and after convolution with the experimental response (black curve). The dashed curve is obtained from the data of ref. [196]. Figure taken from Leistenschneider *et al.* [52], Copyright (2001) by the American Physical Society.

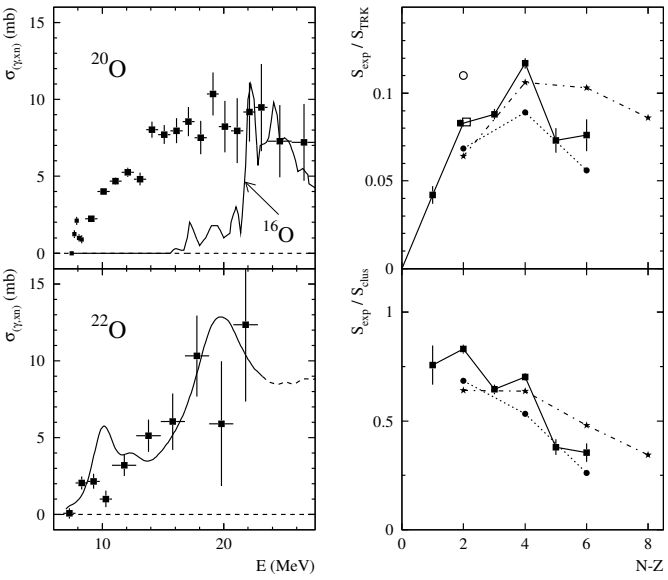

Fig. 30. Left panels: photoneutron cross-sections $\sigma_{(\gamma,xn)}$ for the unstable isotopes ^{20}O (upper panel) and ^{22}O (lower panel) as extracted from the measured electromagnetic excitation cross-section (symbols). For comparison, the photoneutron cross-section for the stable ^{16}O [194] is displayed as the solid curve in the upper panel. Right panels: evolution with neutron excess $N - Z$ of integrated (up to 15 MeV excitation energy) strength S_{exp} in units of the TRK sum rule S_{TRK} (upper panel) and of the cluster sum rule S_{clus} (lower panel) for oxygen isotopes. For the stable isotope ^{18}O, the values extracted from the real-photon absorption experiments are given as the open circle [195] and open square [196]. The values extracted from the electromagnetic-excitation experiment [52] are given by the filled squares. The data are compared to shell-model calculations by Sagawa and Suzuki [45] (stars) and the quasi-particle RPA calculation by Colò and Bortignon [46] (filled circles).

changes significantly due to the presence of the valence neutrons. Most noticeable is the sizeable dipole absorption cross-section below the GDR energy region. A clear separation into two energy domains associated with GDR excitations of the core and a soft-dipole mode involving the valence neutrons is not observed. For ^{22}O, the data are compared to a large-scale shell-model calculation [45] after convolution with the experimental resolution (solid curve in the lower left panel). Qualitatively, the shell-model calculations reproduce the experimental observation of a redistribution of the $E1$ strength towards excitation energies below the GDR.

The right part of fig. 30 shows the energy-weighted experimental low-lying dipole strength $S_{\rm exp}$ (integrated from the particle threshold up to 15 MeV excitation energy) in units of the classical energy-weighted Thomas-Reiche-Kuhn sum rule $S_{\rm TRK} \sim NZ/A$ [129]. While no dipole strength below 15 MeV is observed for the $N = Z$ nucleus ^{16}O, about 10% of the sum rule value is exhausted for the neutron-rich isotopes. The results for the integrated low-lying dipole strength are compared in fig. 30 (right panels) to a large-scale shell-model calculation [45] (stars) and a calculation using the quasi-particle random-phase approximation (QRPA) [46]. Both calculations reproduce the amount (about 5% to 12% of the TRK sum rule value) of dipole strength as found experimentally at low excitation energies. Also, the experimentally observed trend of an increase of the strength as a function of neutron excess up to ^{20}O followed by a decrease for isotopes heavier than ^{20}O is reproduced qualitatively in both calculations. As pointed out in ref. [46], the good agreement between the QRPA calculation and the experiment concerning both the integrated low-lying strength as well as the evolution with neutron excess, was obtained only if coupling to doorway states (phonon coupling) was taken into account. The maximum at $A = 20$ might reflect a shell effect: Both ^{16}O and ^{24}O are doubly-closed-shell nuclei, implying that the low-lying dipole strength is most pronounced for the mid-shell region.

In the lower panel, the same quantity is plotted as fraction of the cluster sum rule $S_{\rm clus}/S_{\rm TRK} = Z_c/A_c \cdot N_\nu/N$ [197], where the indices refer to core (c) and valence (ν) nucleons (^{16}O was assumed as the core). This sum rule results from a decomposition of the dipole strength into excitations of the core, excitations among the valence nucleons (which is zero in the present case), and the dipole strength $S_{\rm clus}$ associated with the relative motion between the core and the valence nucleons. It appears that a large fraction of this sum rule of around 0.5 is exhausted, with a clear tendency of values decreasing with neutron number. The question to which extent the observed low-lying dipole strength involves collective excitations was studied theoretically by Vretenar *et al.* [40] within the relativistic mean-field (RMF) approach. According to this calculation, the low-lying strength in the oxygen isotopes is mainly related to single-neutron particle-hole excitations. For heavier neutron-rich nuclei, *e.g.*, for the tin isotopes, a resonance-like structure at low excitation energy resulting from a coherent superposition

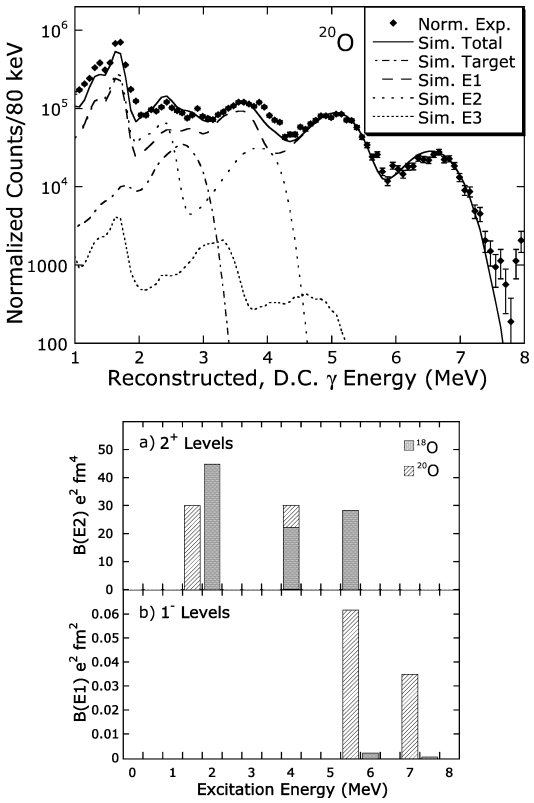

Fig. 31. Electromagnetic excitation of 100 MeV/nucleon ^{20}O projectiles on a lead target [198]. The lower panels show the dipole- and quadrupole-strengths distributions below the neutron separation threshold as extracted from the γ spectrum (upper frame). From Tryggestad *et al.* [198], Copyright (2002), with permission from Elsevier.

of particle-hole excitations is predicted by Paar *et al.* [48]. Similarly, Colò and Bortignon [46] found in their QRPA-plus-phonon-coupling calculation only a small number of components in the wave functions of the low-lying structures in the oxygen isotopes. The low-lying dipole strength observed in neutron-rich oxygen nuclei cannot thus be attributed to a collective soft-dipole ("Pygmy") mode. Contrary to the RMF calculations mentioned above, the QRPA-plus-phonon-coupling model does not predict low-lying collective dipole states even for heavier nuclei, *e.g.*, ^{132}Sn [50].

For ^{20}O, cumulation of dipole strength below the neutron threshold in the energy range from 5 to 7 MeV was extracted from a virtual-photon scattering experiment performed at MSU [199,198]. A radioactive beam of ^{20}O with an energy around 100 MeV/nucleon and an intensity of about 10^6 ions/s was scattered from a lead target. The scattered ions were momentum analyzed in the S800 spectrograph (see fig. 5). Photons from the γ back-decay of the excited states were observed in coincidence in a large BaF array [198]. The upper panel of fig. 31 shows the reconstructed Doppler-corrected γ energy spectrum. The γ decay of higher-lying states, *i.e.*, above the neutron emission threshold (as in the LAND experiment, fig. 30) could not be observed due to two reasons: i) At the lower beam

energy, excitation of dipole states above 8 MeV is suppressed due to the adiabatic cutoff, see eq. (10); ii) above the neutron threshold, the decay is dominated by neutron emission, and the γ back-decay contributes only at the 10^{-2} level [200].

The extracted spectrum displayed in fig. 31 is decomposed into the contributions from different multipolarities [198]. Above 5 MeV, strong excitation of dipole states is observed. The lower frame of the figure displays the extracted strength for quadrupole and dipole transitions. The integrated value of about 0.1 e^2fm^2 [198] for the dipole strength corresponds to much less than 1% of the TRK sum rule, which has to be compared to the low-lying strength above the threshold of about 10%, see fig. 30.

Cumulated dipole strength below the neutron threshold was also observed recently in real-photon scattering experiments on stable nuclei at the S-DALINAC in Darmstadt, *e.g.*, in ^{208}Pb [201] and $N = 82$ isotopes [202], which was discussed in the context of a Pygmy dipole resonance, see also the overview given in the article by Zilges [203]. However, the states observed exhaust only a rather small fraction of the energy-weighted dipole sum rule. In calcium isotopes, for instance, about 0.39% and 0.33% of the energy-weighted dipole sum rule is found below 10 MeV excitation energy for the isotopes ^{44}Ca and ^{48}Ca [204], respectively. This value is close to zero for the $N = Z$ nucleus ^{40}Ca [205]. From the similarity of the integrated strength for ^{44,48}Ca, the authors conclude that a linear dependence between neutron excess and low-lying strength can be excluded, a similar observation as discussed earlier for the oxygen isotopes, see fig. 30. From the fact that the strength below the threshold amounts to only a fraction of the low-lying strength observed just above the threshold (*e.g.* in the case of ^{20}O) one may conclude that the additional dipole strength related to the neutron-proton asymmetry is mainly concentrated at low energies in the continuum.

4.1.3 Perspectives: low-lying collective dipole states and the GDR in medium-mass nuclei

A first experiment investigating the electromagnetic excitation of heavier neutron-rich nuclei was recently performed at GSI utilizing a mixed secondary beam including ^{132}Sn isotopes produced by fission of a ^{238}U beam with an energy of around 600 MeV/nucleon [206]. The experimental method applied is similar to the one discussed for the measurement of the oxygen isotope chain. The differential cross-section for the electromagnetic excitation of ^{130,132}Sn ($\approx$ 500 MeV/nucleon) on a lead target is displayed in fig. 32 (left frames). The right frames display the corresponding photoabsorption (γ, n) cross-sections. The upper right panel shows the result from a real-photon experiment [207] for the stable isotope ^{124}Sn for comparison. The spectrum is dominated by the excitation of the GDR, in contrast to the excitation of lighter nuclei. This is due to the fact that the GDR strength in heavier nuclei is less fragmented, and concentrated at lower excitation energies,

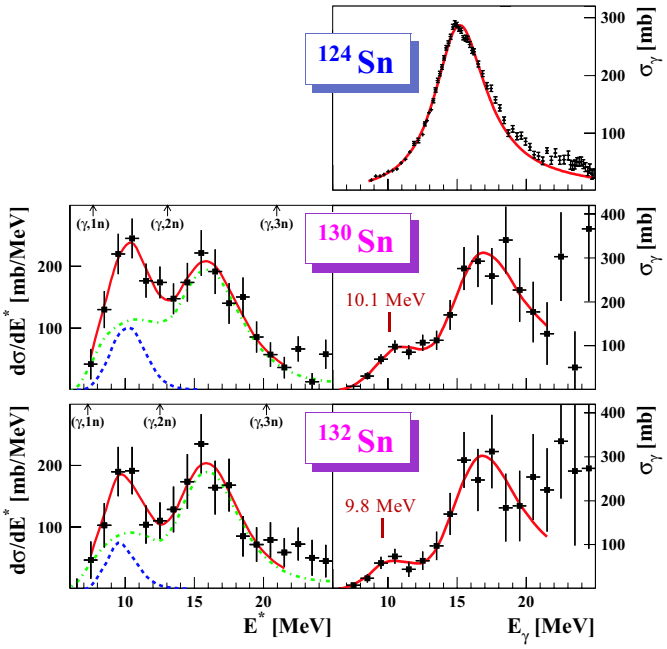

Fig. 32. Left frames: differential cross-section for the electromagnetic excitation of ^{130,132}Sn on a lead target at around 500 MeV/nucleon [206]. Corresponding photoneutron cross-sections are shown in the right panels. The solid curves denote the result from a fit of a Lorentzian (GDR region) plus a Gaussian (low-lying peak) including convolution with the instrumental response. The dash-dotted and dashed curve display the individual contributions. For comparison, photoneutron cross-sections are shown in the upper right frame for the stable isotope ^{124}Sn measured in a real-photon experiment [207]. Reprinted with permission from Adrich *et al.* [206], Copyright (2005) by the American Physical Society.

yielding larger cross-sections for the electromagnetic excitation. A fit of a Lorentzian plus a Gaussian parametrization for the photoabsorption cross-section (solid curves) yields position and width of the GDR comparable to those known for stable nuclei in this mass region. The GDR almost exhausts the energy-weighted dipole sum rule. It should be noted that the spectrum shown in fig. 32 was obtained from a measurement with a rather low beam intensity of about 10 ^{132}Sn ions/s only.

An additional peak structure is clearly visible below the GDR energy region. The position of around 10 MeV is close to the predicted energy of the soft mode (Pygmy resonance) by the relativistic QRPA calculation of Paar *et al.* [48]. The experimentally observed strength in this peak corresponds to about 4% of the TRK sum rule, also in good agreement with the QRPA prediction [48] as well as with the non-relativistic QRPA calculations of Sarchi *et al.* [50]. The collective character of the low-lying structure is, however, still an open question: While the strength is attributed to a few single-particle excitations in the non-relativistic calculation [50], a coherent superposition of many neutron quasi-particle configurations is found in the relativistic approach [48]. Further theoretical and experimental investigations are called for in order to shed light on the nature of the low-lying dipole strength.

4.2 Nuclear scattering to continuum states

The electromagnetic excitation process is mainly selective to dipole transitions, while in the nuclear inelastic scattering, several multipolarities can be excited. Nuclear inelastic scattering was discussed already in the context of spectroscopic studies utilizing the one-neutron removal cross-section, *i.e.*, the diffractive scattering contribution to the cross-section. In kinematically complete experiments, the nuclear inelastic excitation might be used to study resonances in the continuum. As an example, the scattering of ^{6}He from a carbon target shall be discussed.

The upper panels in fig. 33 display the differential cross-section for inelastic excitation of 240 MeV/nucleon ^{6}He on lead (left) and carbon (right) targets as reconstructed from the coincident detection of the α fragment and the two neutrons. In the case of the lead target, the cross-section is dominated by electromagnetic dipole excitations (see also fig. 11). The peak-like structure at 1.8 MeV stems from the excitation of the 2^+ state of ^{6}He. The peak is better visible in the correlation function shown in the lower panels. This function was obtained by dividing the measured spectrum by a randomized spectrum for which the momenta of the three observed particles were taken from different events [53]. It is interesting to note that the excitation of the 2^+ state with the lead target is due to nuclear excitation. The cross-section for electromagnetic excitation is much smaller in this case. This is also evident from a comparison with the measurement using the carbon target (right frames). Here the 2^+ resonance dominates the excitation spectrum. The broad component at higher energies does not reveal any resonant structures, as also seen in the correlation function (lower panel). A second 2^+ state was predicted by three-body models [208] at around 4.3 MeV (indicated by the arrows) but no experimental evidence has been found. The ratio of cross-sections for the 2^+ excitation measured with lead and carbon targets agrees with the prediction from an eikonal calculation for diffractive dissociation, demonstrating the nuclear origin of the excitation also in the case of the heavy target.

Apart from the 1.8 MeV resonance, both the excitation energy spectrum and the correlation function appear to be structureless. This smooth continuum could be composed of various multipolarities. In order to explore the different contributions, the differential cross-section as a function of the scattering angle was inspected [53,209]. In fig. 34 the angular distribution is compared to calculations based on the distorted-wave Born approximation (DWBA) combined with the $t\rho\rho$ approximation [210]. The data correspond to the excitation energy region above the 2^+ resonance, *i.e.*, between 2.5 and 4.5 MeV. This analysis is parameter free since the input quantities (the density distributions of target and projectile and the nucleon-nucleon cross-sections) can be taken from independent experiments. In the left part of fig. 34, calculations for quadrupole (dashed curve) and monopole (dotted curve) excitations are shown, for which low-lying strength is predicted from three-body models [124–126]. The sum of both (solid curve) can account for the experimental spectrum.

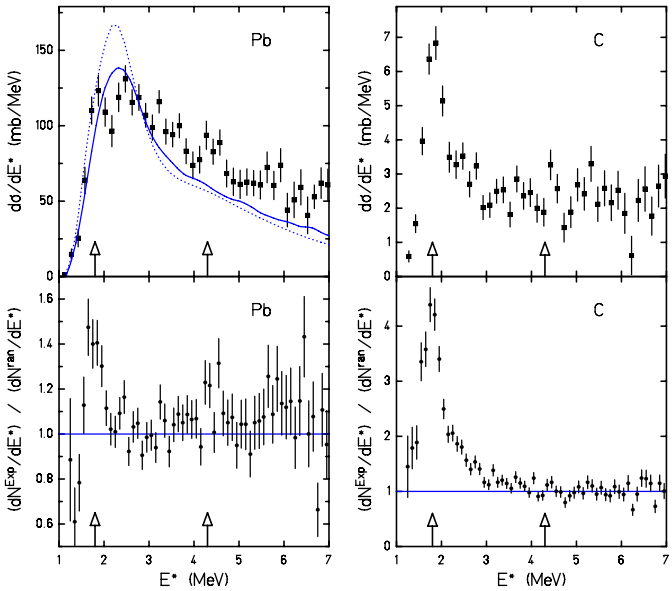

Fig. 33. Continuum excitations of ^{6}He in nuclear and electromagnetic scattering on lead (left frames) and carbon (right frames) targets. The upper parts show the differential cross-sections as a function of excitation energy E^*, the lower parts the corresponding correlation functions (figure reprinted with permission from Aumann *et al.* [53], Copyright (1999) by the American Physical Society).

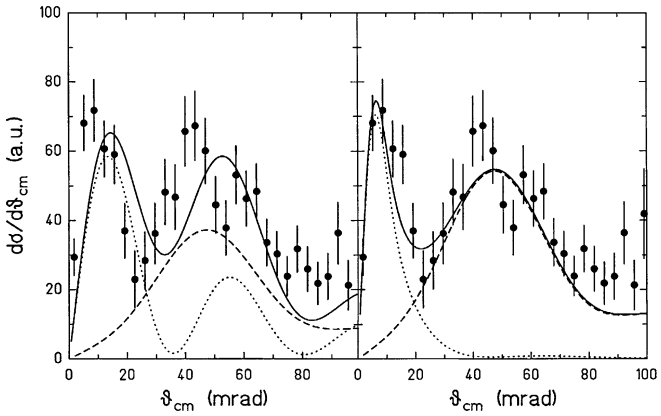

Fig. 34. Differential cross-section with respect to the scattering angle for inelastic scattering on a carbon target. The data correspond to an excitation energy interval of 2.5 to 4.5 MeV (see fig. 33). The curves in the left part show DWBA calculations for monopole (dotted) and quadrupole (dashed) transitions. The right part displays the result for electromagnetic dipole (dotted) and quadrupole (dashed) transitions. Figure taken from Aleksandrov *et al.* [209], Copyright (2000), with permission from Elsevier.

Isovector dipole excitations are expected to be suppressed since the carbon target is a self-conjugate $T = 0$ system, although isoscalar probes may induce isovector transitions, *e.g.*, in nuclei with neutron excess, due to different radial extent of proton and neutron matter distributions.

The strength function $\mathrm{d}B(E1)/\mathrm{d}E$ deduced from the electromagnetic excitation cross-section measured with

the lead target [53] (see fig. 15) allows an estimate of the contribution of Coulomb dissociation in a carbon target for a selected region of excitation energies. The estimated result is 2 mb or about 30% of the total diffractive disintegration cross-section in the excitation energy interval between 2.5 and 4.5 MeV. The contribution from the hadronic $\Delta\ell = 1$ transition is smaller by a factor of ~ 10. The Coulomb dissociation is characterized by a peak close to zero degree. The corresponding differential cross-section, corrected for the experimental angular resolution, is shown in the right panel of fig. 34 by the dotted curve. The solid curve shows the sum of 30% Coulomb dipole and 70% nuclear quadrupole cross-sections.

The good agreement with the experimental data for the angular distribution supports the interpretation that the cross-section close to zero degree is not related to monopole excitations but shows that Coulomb dissociation is important even for a carbon target. A similar conclusion was drawn from a measurement of inelastic excitation of ^{11}Be on a carbon target performed at RIKEN by Fukuda *et al.* [59]. Besides the observation of several resonant structures in the continuum of ^{11}Be, they found an appreciable Coulomb component at small scattering angles [59]. The agreement between the calculations and the data allows to conclude that $\Delta\ell = 2$ dominates at large scattering angles. This conclusion is similar to the one from the ^{6}Li(^{7}Li,^{7}Be)^{6}He charge-exchange reaction [211]. There, the excitation energy spectrum reveals a broad bump with a width of about 12 MeV centered at 5.6 MeV, which is assigned by the authors to a quadrupole transition [211]. In the charge-exchange reaction mentioned above and, more recently, in the ^{6}Li(t,^{3}He)^{6}He reaction [212] also higher-lying states were observed [211,212]. In an inelastic proton scattering experiment [213], a structureless continuum was observed in addition to the first 2^+ resonance in accordance with the result shown in fig. 33.

The method of inelastic scattering from carbon has been applied also to the dripline nucleus ^{8}He and evidence for dipole and quadrupole strength in the low-energy continuum has been found by Markenroth *et al.* [145] utilizing a ^{8}He secondary beam at 227 MeV/nucleon. A broad bump was observed in the continuum excitation spectrum, which was suggested as due to the overlap of two resonances, a 2^+ state at 2.9 MeV ($\Gamma = 0.3$ MeV) and a broader 1^- state at 4.15 MeV ($\Gamma = 1.6$ MeV) [145]. The latter assignment was motivated by the differential cross-section with respect to the scattering angle, which is further supported by the observation of the Coulomb nuclear interference in the angular distribution measured with a lead target [122].

5 Astrophysical aspects

In the previous sections the reactions with radioactive beams were discussed mainly in the context of investigating the nuclear structure of exotic nuclei. Such reactions are also an important tool to obtain information on reactions relevant for astrophysical scenarios. Often, they cannot be studied in a direct way because short-lived nuclei are involved, but the reaction rate of interest may be obtained from a measurement of the inverse process. A prominent example, which was studied extensively using both approaches, is the ^{7}Be$(p,\gamma)^8$B reaction which is important for the production of high-energy neutrinos in the Sun. While results from existing direct measurements of this reaction do not agree with each other, the measurement of the inverse reaction may yield additional insight due to different systematic uncertainties. Coulomb breakup measurements of ^{8}B were performed at different energies at RIKEN [214], MSU [215], and GSI [216], and the zero-energy astrophysical S factor $S_{17}(0)$ was extracted. From the measurement of Schümann *et al.* [216], providing the most precise data with good statistics, a $S_{17}(0)$ value was extracted which is in agreement with a recent precision measurement of the direct reaction by Junghans *et al.* [216–218].

Neutron capture processes on neutron-rich nuclei play an important role in astrophysical processes, *e.g.*, in the nuclear synthesis in stellar helium- and carbon-burning stages as well as in the slow (s-process) and rapid (r-process) neutron capture processes taking place in explosive stellar scenarios [219]. The r-process, for instance, involves short-lived neutron-rich nuclei far away from the β-stability line. A systematic change of the dipole response for neutron-rich nuclei, *e.g.*, the appearance of low-lying strength as discussed in the previous section, would have an impact on the elemental r-process abundances [220]. In the following, two specific examples of Coulomb breakup experiments relevant for astrophysical processes shall be discussed.

The ^{14}C(n,γ) reaction is important in neutron-induced CNO cycles of stellar evolution phases beyond the main sequence [221]. Starting from the most abundant isotope ^{12}C, successive neutron capture reactions and β decays finally yield ^{18}O. The neutron capture on carbon isotopes runs up to ^{15}C, the last one being the slowest reaction in this cycle. The ^{14}C(n,γ) reaction rate is also important in inhomogeneous Big-Bang models. In this scenario, a high neutron flux induces primordial nucleosynthesis which bridges the mass-5 and -8 gaps [222]. Subsequent neutron capture processes on neutron-rich carbon, nitrogen, and oxygen isotopes may bypass the long-lived ^{14}C and trigger a primordial r-process [223]. A direct measurement of the ^{14}C(n,γ) reaction rate is difficult since the cross-section at the low energies of astrophysical interest is small and the experiment involves a radioactive target. Beer *et al.* [224] succeeded in measuring this cross-section with a neutron source approximating a Maxwell distribution with $kT = 23$ keV. The cross-section of 1.10(28) μb from the direct measurement is much lower than the theoretical predictions, see fig. 35. The inverse process was studied in two Coulomb breakup experiments at 35 MeV/nucleon at MSU [225] and at 605 MeV/nucleon at GSI [60]. From the differential cross-section for electromagnetic dissociation in a lead target, the photoneutron cross-section can be obtained, which can be converted into the cross-section for the time-reversed process by the

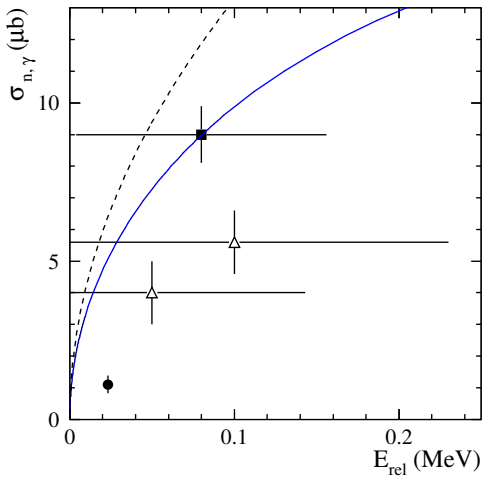

Fig. 35. ^{14}C(n,γ) neutron capture cross-section as a function of ^{14}C-n relative energy $E_{\rm rel}$. The result from the direct measurement of Beer *et al.* [224] is displayed as the circle, the results derived from Coulomb breakup experiments at high (605 MeV/nucleon) [60] and low (35 MeV/nucleon) [225] beam energy are shown as the square and the triangles, respectively. The solid and dashed curves denote the theoretical estimates by Mengoni [226,227] and Descouvemont [228], respectively.

principle of detailed balance [112]:

$$\sigma_{n,\gamma}(E_{\rm rel}) = \frac{(2j_a+1)}{(2j_b+1)(2j_n+1)}\,\frac{1}{\mu c^2}\,\frac{E_\gamma^2}{E_{\rm rel}}\,\sigma_{\gamma,n}, \qquad (11)$$

for a reaction of the type $\gamma + a \rightarrow b + n$ with μ being the reduced mass of the $b+n$ system, *i.e.*, $\mu = \frac{m_b m_n}{(m_b+m_n)}$. The energy E_γ of the photon and the b-n relative energy $E_{\rm rel}$ differ by the neutron separation energy S_n (1.218 MeV in case of ^{15}C): $E_\gamma = E_{\rm rel} + S_n$. As can be seen from the above equation, the cross-section $\sigma_{\gamma,n}$ for the inverse process is favored by the phase-space factor for not too small values of E_γ. As an example, for the electromagnetic dissociation of ^{15}C with 605 MeV/nucleon on a lead target, a cross-section of 39(4) mb/MeV [60] was measured at 80 keV relative energy which translates into a photoneutron cross-section of 0.38(4) mb. By applying the above equation, a capture cross-section of 9.0(9) μb is obtained. The lowest-energy point of this Coulomb breakup measurement [60] is given in fig. 35 (square) together with the values deduced from the MSU Coulomb breakup data (triangles) [225]. The horizontal error bars denote the energy resolutions of the Coulomb breakup experiments ($\pm 1\sigma$). It is evident that better resolution would be helpful for the measurement of such low-energy cross-sections relevant for astrophysical processes. The data are compared to model predictions by Mengoni [226, 227] (solid curve) and Descouvement [228] (dashed curve). A $\sqrt{E_{\rm rel}}$-dependence of the cross-section is observed at low energies as expected for p-wave capture. Good agreement is found between the result from the high-energy Coulomb breakup and the model of Mengoni [226]. The situation is not conclusive, however, since the data taken at lower incident energy are significantly lower, and the direct measurement gives an even lower cross-section. Results from a preliminary analysis of a recent Coulomb breakup experiment performed at RIKEN [229] are consistent with the GSI data [60] showing good agreement with the model prediction of Mengoni down to 50 keV [229,227].

In the following, an example shall be discussed which can only be studied in the inverse reaction since an unbound nucleus is involved, the two-neutron capture on ^{4}He. In the past years, it was discussed that the post-collapse phase in a type-II supernovae may offer the "ideal site" for the r-process, forming the heaviest elements. In the preceding α process, elements up to masses $A \leq 100$ are synthesized. The bottleneck in this nucleosynthesis process is the formation of nuclei with $A \geq 9$ from nucleons and α-particles. Two-step processes such as ^{4}He$(2n,\gamma)^6$He and ^{6}He$(2n,\gamma)^8$He were considered potentially to be relevant in bridging the instability gaps at $A = 5$ and $A = 8$, see refs. [222,230,231] and references cited therein. It is presently believed that the two-neutron capture cannot compete with the $(\alpha n,\gamma)$ process in a type-II supernovae scenario, but other scenarios such as production of r-process elements in the fusion of two neutron stars are still under discussion, for which the relevance of two-neutron capture processes is yet to be explored [232]. In any case, it is certainly of interest to check experimentally the model-dependent assumptions on which such conclusions are based so far. As far as the ^{4}He$(2n,\gamma)^6$He reaction is concerned, the mechanism to contribute most is that of the formation of the ^{5}He ground-state resonance as an intermediate state, followed by radiative capture of a second neutron into the ^{6}He $I^\pi = 2^+$ (1.80 MeV) resonance. Non-resonant mechanisms involving $E1$ photoabsorption, however, were considered as well. The data on the electromagnetic dissociation of ^{6}He [53] discussed in sect. 3.3.4 comprise exactly the inverse process, *i.e.*, absorption of a (virtual) γ quantum followed by two-neutron emission.

First, a value of $B(E2,\ 0^+ \rightarrow 2^+) = 3.2(0.6)\ e^2{\rm fm}^4$ was extracted from the nuclear inelastic scattering [53] which can be compared to the one used in the model calculation of Görres *et al.* [230]. There, a value of 2.85 $e^2{\rm fm}^4$ was adopted, which is confirmed by the data.

In addition, the importance of non-resonant transitions can be estimated on the basis of the Coulomb breakup data. In fact, Efros *et al.* [222] consider the process of a non-resonant electric dipole transition as the main contribution to the second step of the reaction, *i.e.*, the neutron capture leading from ^{5}He to ^{6}He. Relying on $B(E1)$ strength distributions from a three-body model, they conclude that there must be an enhancement of three orders of magnitude of the non-resonant mechanism in comparison to the resonant one via the ^{6}He $I^\pi = 2^+$ (1.80 MeV) resonance. It is straightforward to transform the experimental ${\rm d}B(E1)/{\rm d}E^*$ distribution [53] (fig. 15) into a photoabsorption cross-section, which can be compared to the one used in the calculation of Efros *et al.*, see fig. 3 of ref. [222]. Their photoabsorption cross-section for the ^{6}He$(\gamma,n)^5$He reaction peaks at around 2.3 MeV with a value of 0.12 mb, the photoabsorption cross-section integrated up to 8 MeV

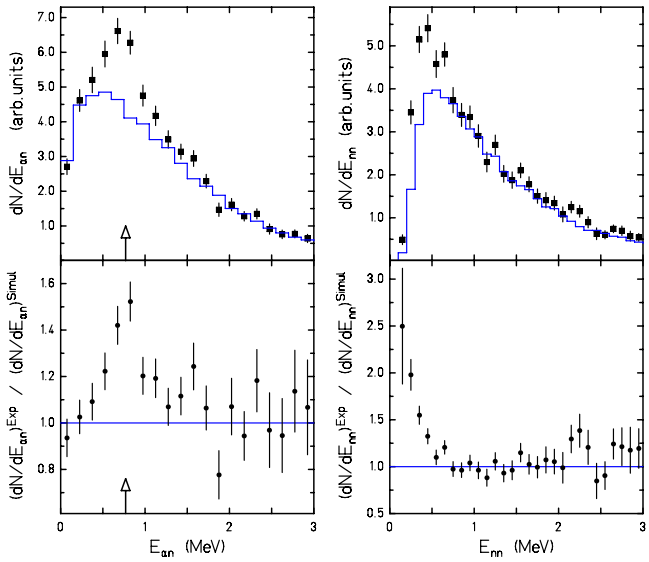

Fig. 36. Two-body correlations in the three-body decay of ^{6}He. The lower panels show the ratio between the measured α-n and n-n relative-energy spectra (upper panels) and the spectra simulated (histograms) according to standard phase-space distributions. Figure reprinted with permission from [53], Copyright (1999) by the American Physical Society.

excitation energy amounts to about 0.4 mb MeV. From the Coulomb breakup data, a total photoabsorption cross-section, integrated up to 8 MeV, of 16(3) mb MeV is deduced [53]. In comparing with the calculation of ref. [222], however, only that fraction of cross-section is relevant which proceeds via the ^{5}He ground-state resonance. One may obtain an estimate of this fraction from the two-body correlation spectra. Figure 36 shows the relative-energy spectra of the α-n and n-n subsystems in the three-body decay of ^{6}He after inelastic scattering on a lead target. The data are compared to simulations starting from the measured excitation energy and distributing the available kinetic energy among the α-particle and the two neutrons according to standard phase-space distributions (histograms). The lower part shows the ratio of the measured two-body relative-energy distributions and the phase-space distributions. In both spectra, deviations from the phase-space distributions are observed. In the neutron-neutron spectrum very low relative energies appear to be enhanced, qualitatively in accordance with the known, very low-lying virtual state in the neutron-neutron channel. In the neutron-α spectrum, the observed excess of cross-section coincides in energy with the ^{5}He ground-state resonance. From this spectrum, it was deduced that about 10% of the cross-section leads to the ^{5}He resonance. Assuming that the ^{5}He formation is independent of the γ energy, a rough estimate of the photoabsorption cross-section for the ^{6}He$(\gamma, n)^5$He reaction amounts to about 1.6 mb MeV. This value is of the same order of magnitude as the one used by Efros *et al.*, given above.

6 Concluding remarks and outlook

In the past years, scattering experiments utilizing relativistic radioactive beams became a major and efficient tool for the investigation of nuclear structure of short-lived nuclei. Experimental approaches utilizing high-energy reactions have been developed coping with the properties of secondary fragmentation beams as, *e.g.*, low intensities and a large momentum spread. Detailed information on nuclear structure and reaction mechanisms involving weakly bound nuclei have been obtained and many new phenomena were found. Several types of reactions and the associated nuclear structure of exotic nuclei were discussed in the present paper.

The advantage of using high beam energies is from the theoretical point of view the simplicity of the reaction mechanisms allowing a clean separation of the reaction and nuclear-structure observables. In conjunction with an elaborated reaction theory, high-energy reactions have been established as a precise spectroscopic tool. From the exclusive measurement of one-neutron removal reactions, for instance, the single-particle structure of exotic nuclei is studied and spectroscopic factors are deduced with a precision on an absolute scale exceeding those of transfer reactions which have been a standard tool for the investigation of stable nuclei.

Another advantage of the high beam energies is the enormous effectiveness due to the kinematical forward focussing of reaction products and the possibility of using thick targets. Experiments with an efficiency close to 100% are feasible making nuclear-structure studies possible with beam intensities of a few ions/s only. The ground-state structure of very neutron-rich nuclei was investigated, for instance, via knockout reactions with beams down to one ion/s. Another example is the study of dipole excitations in the continuum utilizing electromagnetic excitation. The dipole-strength function of, *e.g.*, ^{132}Sn was extracted with a beam intensity of about 10 ions/s and cumulation of dipole strength below the giant dipole resonance was observed, which might be, according to theoretical predictions, associated with a collective soft-dipole excitation of valence neutrons against the core.

So far, reactions with relativistic beams were applied mainly to light nuclei. The neutron dripline has been reached up to oxygen. Higher primary-beam intensities are necessary to explore the dripline for heavier nuclei. New accelerators as planned in RIKEN in Japan, RIA in the United States, and FAIR in Europe will provide the basis for such investigations. Applying the experimental approaches as discussed in the present article to medium-mass and heavier nuclei needs, in addition, experimental developments. A substantially improved setup for kinematically complete measurements of reactions with relativistic radioactive beams (R3B) [233] comprising, in addition, a detection scheme for light recoil particles, is currently being planned for the FAIR [183] facility in Darmstadt. The proposed setup provides significantly higher resolution allowing the investigation of nuclear structure by scattering experiments also for heavier nuclei. The envisaged improvement in invariant-mass resolution will

allow precise studies of reactions at energies relevant for astrophysical scenarios. In addition, new experimental approaches involving storage rings will overcome some limitations presently given by the need of applying inverse kinematics. Scattering experiments of radioactive beams from light hadrons at low momentum transfer, and even electron scattering experiments will become possible in the future [184].

The experiments discussed in the present article are the result of the efforts by large collaborations. The author would like to thank all members of the different collaborations which he has or had the pleasure to be a member of and expresses special thanks to the members of the LAND group, the "Halo Collaboration", and the MSU "knock-out Collaboration".

References

1. A collection of recent review articles can be found in: Nucl. Phys. A **693** (2001), special issue on *Research Opportunities with Accelerated Beams of Radioactive Ions*, edited by I. Tanihata.
2. T.J.M. Symons, Y.P. Viyogi, G.D. Westfall, P. Doll, D.E. Greiner, H. Faraggi, P.J. Lindstrom, D.K. Scott, H.J. Crawford, C. McParland, Phys. Rev. Lett. **42**, 40 (1979).
3. G.D. Westfall, T.J.M. Symons, D.E. Greiner, H.H. Heckman, P.J. Lindstrom, J. Mahoney, A.C. Shotter, D.K. Scott, H.J. Crawford, C. McParland, T.C. Awes, K. Gelbke, J.M. Kidd, Phys. Rev. Lett. **43**, 1859 (1979).
4. I. Tanihata, H. Hamagaki, O. Hashimoto, S. Nagamiya, Y. Shida, N. Yoshikawa, O. Yamakawa, K. Sugimoto, T. Kobayashi, D.E. Greiner, N. Takahashi, Y. Nojiri, Phys. Lett. B **160**, 380 (1985).
5. I. Tanihata, H. Hamagaki, O. Hashimoto, Y. Shida, N. Yoshikawa, K. Sugimoto, O. Yamakawa, T. Kobayashi, N. Takahashi, Phys. Rev. Lett. **55**, 2676 (1985).
6. I. Tanihata, T. Kobayashi, O. Yamakawa, S. Shimoura, K. Ekuni, K. Sugimoto, N. Takahashi, T. Shimoda, H. Sato, Phys. Lett. B **206**, 592 (1988).
7. P.G. Hansen, B. Jonson, Europhys. Lett. **4**, 409 (1987).
8. M.V. Zhukov, B.V. Danilin, D.V. Fedorov, J.M. Bang, I.J. Thompson, J.S. Vaagen, Phys. Rep. **231**, 151 (1993).
9. A.C. Mueller, B.M. Sherrill, Annu. Rev. Nucl. Part. Sci. **43**, 529 (1993).
10. K. Riisager, Rev. Mod. Phys. **66**, 1105 (1994).
11. P.G. Hansen, A.S. Jensen, B. Jonson, Annu. Rev. Nucl. Part. Sci. **45**, 591 (1995).
12. I. Tanihata, Prog. Part. Nucl. Phys. **35**, 505 (1995).
13. I. Tanihata, J. Phys. G **22**, 157 (1996).
14. N.A. Orr, Nucl. Phys. A **616**, 155c (1997).
15. R.F. Casten, B.M. Sherrill, Prog. Part. Nucl. Phys. **45**, 171 (2000).
16. B. Jonson, Phys. Rep. **389**, 1 (2004).
17. A.S. Jensen, K. Riisager, D.V. Fedorov, E. Garrido, Rev. Mod. Phys. **76**, 215 (2004).
18. A. Ozawa, T. Suzuki, I. Tanihata, Nucl. Phys. A **693**, 32 (2001).
19. E. Arnold, J. Bonn, A. Klein, R. Neugart, M. Neuroth, E.-W. Otten, P. Lievens, H. Reich, W. Widdra, Phys. Lett. B **281**, 16 (1992).
20. B. Blank, J.-J. Gaimard, H. Geissel, K.-H. Schmidt, H. Stelzer, K. Sümmerer, D. Bazin, R. Del Moral, J.P. Dufour, A. Fleury, F. Hubert, H.G. Clerc, M. Steiner, Z. Phys. A **343**, 375 (1992).
21. S.R. Neumaier, G.D. Alkhazov, M.N. Andronenko, A.V. Dobrovolsky, P. Egelhof, G.E. Gavrilov, H. Geissel, H. Irnich, A.V. Khanzadeev, G.A. Korolev, A.A. Lobodenko, G. Münzenberg, M. Mutterer, W. Schwab, D.M. Seliverstov, T. Suzuki, N.A. Timofeev, A.A. Vorobyov, V.I. Yatsoura, Nucl. Phys. A **712**, 247 (2002).
22. P. Egelhof, G.D. Alkhazov, M.N. Andronenko, A. Bauchet, A.V. Dobrovolsky, S. Fritz, G.E. Gavrilov, H. Geissel, C. Gross, A.V. Khanzadeev, G.A. Korolev, G. Kraus, A.A. Lobodenko, G. Münzenberg, M. Mutterer, S.R. Neumaier, T. Schäfer, C. Scheidenberger, D.M. Seliverstov, N.A. Timofeev, A.A. Vorobyov, V.I. Yatsoura, Eur. Phys. J. A **15**, 27 (2002).
23. J. Meng, P. Ring, Phys. Rev. Lett. **80**, 460 (1998).
24. J. Meng, H. Toki, J.Y. Zeng, S.Q. Zhang, S.-G. Zhou, Phys. Rev. C **65**, 041302 (2002).
25. M.H. Macfarlane, J.P. Schiffer, in *Nuclear Spectroscopy and Reactions, Part B*, edited by J. Cerny (Academic Press, New York, 1974) p. 169.
26. T. Otsuka, R. Fujimoto, Y. Utsuno, B.A. Brown, M. Honma, T. Mizusaki, Phys. Rev. Lett. **87**, 082502 (2001).
27. Y. Utsuno, T. Otsuka, T. Mizusaki, M. Honma, Phys. Rev. C **60**, 054315 (1999).
28. A. Ozawa, T. Kobayashi, T. Suzuki, K. Yoshida, I. Tanihata, Phys. Rev. Lett. **84**, 5493 (2000).
29. G. Coló, T. Suzuki, H. Sagawa, Nucl. Phys. A **695**, 167 (2001).
30. R. Kanungo, I. Tanihata, A. Ozawa, Phys. Lett. B **528**, 58 (2002).
31. B.A. Brown, Prog. Part. Nucl. Phys. **47**, 517 (2001).
32. B.A. Brown, *Proceedings of the 10th International Conference on Nuclear Reaction Mechanisms, June 9-13, 2003, Varenna, Italy*, edited by E. Gadioli, Ric. Sci. Educ. Perm., Supplemento No. 122 (2003) p. 41.
33. G.A. Lalazissis, D. Vretenar, W. Pöschl, P. Ring, Phys. Lett. B **418**, 7 (1998).
34. J. Dobaczewski, I. Hamamoto, W. Nazarewicz, J.A. Sheikh, Phys. Rev. Lett. **72**, 981 (1994).
35. T. Otsuka, Y. Utsuno, R. Fujimoto, B.A. Brown, M. Honma, T. Mizusaki, Eur. Phys. J. A **13**, 69 (2002).
36. C.A. Bertulani, L.F. Canto, M.S. Hussein, Phys. Rep. **226**, 281 (1993).
37. J. Al-Khalili, F. Nunes, J. Phys. G **29**, R89 (2003).
38. G. Baur, K. Hencken, D. Trautmann, Prog. Part. Nucl. Phys. **51**, 487 (2003).
39. P.G. Hansen, J.A. Tostevin, Annu. Rev. Nucl. Part. Sci. **53**, 219 (2003).
40. D. Vretenar, N. Paar, P. Ring, G.A. Lalazissis, Nucl. Phys. A **692**, 496 (2001).
41. T. Aumann, P.F. Bortignon, H. Emling, Annu. Rev. Nucl. Part. Sci. **48**, 351 (1998).
42. I. Hamamoto, H. Sagawa, Phys. Rev. C **53**, R1492 (1996).
43. F. Ghielmetti, G. Colò, P.F. Bortignon, R.A. Broglia, Phys. Rev. C **54**, R2143 (1996).
44. P.G. Reinhard, Nucl. Phys. A **649**, 305c (1999).
45. H. Sagawa, T. Suzuki, Phys. Rev. C **59**, 3116 (1999).
46. G. Colò, P.F. Bortignon, Nucl. Phys. A **696**, 427 (2001).
47. M. Matsuo, Nucl. Phys. A **696**, 371 (2001); Prog. Theor. Phys. Suppl. **146**, 110 (2002).

48. N. Paar, P. Ring, T. Nikšić, D. Vretenar, Phys. Rev. C **67**, 034312 (2003).
49. N. Tsoneva, H. Lenske, Ch. Stoyanov, Phys. Lett. B **586**, 213 (2004).
50. D. Sarchi, P.F. Bortignon, G. Colò, Phys. Lett. B **601**, 27 (2004).
51. P. Papakonstantinou, J. Wambach, E. Mavrommatis, V.Yu. Ponomarev, Phys. Lett. B **604**, 157 (2004).
52. A. Leistenschneider, T. Aumann, K. Boretzky, D. Cortina, J. Cub, U. Datta Pramanik, W. Dostal, Th.W. Elze, H. Emling, H. Geissel, A. Grünschloß, M. Hellström, R. Holzmann, S. Ilievski, N. Iwasa, M. Kaspar, A. Kleinböhl, J.V. Kratz, R. Kulessa, Y. Leifels, E. Lubkiewicz, G. Münzenberg, P. Reiter, M. Rejmund, C. Scheidenberger, Ch. Schlegel, H. Simon, J. Stroth, K. Sümmerer, E. Wajda, W. Walus, S. Wan, Phys. Rev. Lett. **86**, 5442 (2001).
53. T. Aumann, D. Aleksandrov, L. Axelsson, T. Baumann, M.J.G. Borge, L.V. Chulkov, J. Cub, W. Dostal, B. Eberlein, Th.W. Elze, H. Emling, H. Geissel, V.Z. Goldberg, M. Golovkov, A. Grünschloß, M. Hellström, K. Hencken, J. Holeczek, R. Holzmann, B. Jonson, A.A. Korshenninikov, J.V. Kratz, G. Kraus, R. Kulessa, Y. Leifels, A. Leistenschneider, T. Leth, I. Mukha, G. Münzenberg, F. Nickel, T. Nilsson, G. Nyman, B. Petersen, M. Pfützner, A. Richter, K. Riisager, C. Scheidenberger, G. Schrieder, W. Schwab, H. Simon, M.H. Smedberg, M. Steiner, J. Stroth, A. Surowiec, T. Suzuki, O. Tengblad, M.V. Zhukov, Phys. Rev. C **59**, 1252 (1999).
54. D. Sackett, K. Ieki, A. Galonsky, C.A. Bertulani, H. Esbensen, J.J. Kruse, W.G. Lynch, D.J. Morrissey, B.M. Sherrill, H. Schulz, A. Sustich, J.A. Winger, F. Deák, Á. Horváth, Á. Kiss, Z. Seres, J.J. Kolata, R.E. Warner, D. Humphrey, Phys. Rev. C **48**, 118 (1993).
55. S. Shimoura, T. Nakamura, M. Ishihara, N. Inabe, T. Kobayashi, T. Kubo, R.H. Siemssen, I. Tanihata, Y. Watanabe, Phys. Lett. B **348**, 29 (1995).
56. M. Zinser, F. Humbert, T. Nilsson, W. Schwab, H. Simon, T. Aumann, M.J.G. Borge, L.V. Chulkov, J. Cub, Th.W. Elze, H. Emling, H. Geissel, D. Guillemaud-Mueller, P.G. Hansen, R. Holzmann, H. Irnich, B. Jonson, J.V. Kratz, R. Kulessa, Y. Leifels, A. Magel, A.C. Mueller, G. Münzenberg, F. Nickel, G. Nyman, A. Richter, K. Riisager, C. Scheidenberger, G. Schrieder, K. Stelzer, J. Stroth, A. Surowiec, O. Tengblad, E. Wajda, E. Zude, Nucl. Phys. A **619**, 151 (1997).
57. R. Palit, P. Adrich, T. Aumann, K. Boretzky, B.V. Carlson, D. Cortina, Th.W. Elze, H. Emling, H. Geissel, M. Hellström, K.L. Jones, J.V. Kratz, R. Kulessa, Y. Leifels, A. Leistenschneider, G. Münzenberg, C. Nociforo, P. Reiter, H. Simon, K. Sümmerer, W. Walus, Phys. Rev. C **68**, 034318 (2003).
58. T. Nakamura, S. Shimoura, T. Kobayashi, T. Teranishi, K. Abe, N. Aoi, Y. Doki, M. Fujimaki, N. Inabe, N. Iwasa, K. Katori, T. Kubo, H. Okuno, T. Suzuki, I. Tanihata, Y. Watanabe, A. Yoshida, M. Ishihara, Phys. Lett. B **331**, 296 (1994).
59. N. Fukuda, T. Nakamura, N. Aoi, N. Imai, M. Ishihara, T. Kobayashi, H. Iwasaki, T. Kubo, A. Mengoni, M. Notani, H. Otsu, H. Sakurai, S. Shimoura, T. Teranishi, Y.X. Watanabe, K. Yoneda, Phys. Rev. C **70**, 054606 (2004).
60. U. Datta Pramanik, T. Aumann, K. Boretzky, B.V. Carlson, D. Cortina, Th.W. Elze, H. Emling, H. Geissel, A. Grünschloß, M. Hellström, S. Ilievski, J.V. Kratz, R. Kulessa, Y. Leifels, A. Leistenschneider, E. Lubkiewicz, G. Münzenberg, P. Reiter, H. Simon, K. Sümmerer, E. Wajda, W. Walus, Phys. Lett. B **551**, 63 (2003).
61. T. Nakamura, N. Fukuda, T. Kobayashi, N. Aoi, H. Iwasaki, T. Kubo, A. Mengoni, M. Notani, H. Otsu, H. Sakurai, S. Shimoura, T. Teranishi, Y.X. Watanabe, K. Yoneda, M. Ishihara, Phys. Rev. Lett. **83**, 1112 (1999).
62. C. Nociforo, K.L. Jones, L.H. Khiem, P. Adrich, T. Aumann, B.V. Carlson, D. Cortina-Gil, U. Datta Pramanik, Th.W. Elze, H. Emling, H. Geissel, M. Hellström, J.V. Kratz, R. Kulessa, T. Lange, Y. Leifels, E. Lubkiewicz, G. Münzenberg, R. Palit, H. Scheit, H. Simon, K. Sümmerer, S. Typel, E. Wajda, W. Walus, H. Weick, Phys. Lett. B **605**, 79 (2005).
63. V. Maddalena, T. Aumann, D. Bazin, B.A. Brown, J.A. Caggiano, B. Davids, T. Glasmacher, P.G. Hansen, R.W. Ibbotson, A. Navin, B. Pritychenko, H. Scheit, B.M. Sherrill, M. Steiner, J.A. Tostevin, J. Yurkon, Phys. Rev. C **63**, 024613 (2001).
64. B.M. Sherrill, D.J. Morrissey, J.A. Nolen jr., N. Orr, J.A. Winger, Nucl. Instrum. Methods Phys. Res. B **70**, 298 (1992).
65. H. Geissel, P. Armbruster, K.H. Behr, A. Brünle, K. Burkard, M. Chen, H. Folger, B. Franczak, H. Keller, O. Klepper, B. Langenbeck, F. Nickel, E. Pfeng, M. Pfützner, E. Roeckl, K. Rykaczewski, I. Schall, D. Schardt, C. Scheidenberger, K.-H. Schmidt, A. Schröter, T. Schwab, K. Sümmerer, M. Weber, G. Münzenberg, T. Brohm, H.-G. Clerc, M. Fauerbach, J.-J. Gaimard, A. Grewe, E. Hanelt, B. Knödler, M. Steiner, B. Voss, J. Weckenmann, C. Ziegler, A. Magel, H. Wollnik, J.P. Dufour, Y. Fujita, D.J. Vieira, B. Sherrill, Nucl. Instrum. Methods Phys. Res. B **70**, 286 (1992).
66. B.M. Sherrill *et al.*, unpublished; J.A. Caggiano, PhD Thesis, Michigan State University, 1999.
67. J. Yurkon, D. Bazin, W. Benenson, D.J. Morrissey, B.M. Sherrill, D. Swan, R. Swanson, Nucl. Intrum. Methods Phys. Res. A **422**, 291 (1999).
68. A. Navin, D.W. Anthony, T. Aumann, T. Baumann, D. Bazin, Y. Blumenfeld, B.A. Brown, T. Glasmacher, P.G. Hansen, R.W. Ibbotson, P.A. Lofy, V. Maddalena, K. Miller, T. Nakamura, B. Pritychenko, B.M. Sherrill, E. Spears, M. Steiner, J.A. Tostevin J. Yurkon, A. Wagner, Phys. Rev. Lett. **85**, 266 (2000).
69. T. Aumann, A. Navin, D.P. Balamuth, D. Bazin, B. Blank, B.A. Brown, J.E. Bush, J.A. Caggiano, B. Davids, T. Glasmacher, V. Guimarães, P.G. Hansen, R.W. Ibbotson, D. Karnes, J.J. Kolata, V. Maddalena, B. Pritychenko, H. Scheit, B.M. Sherrill, J.A. Tostevin, Phys. Rev. Lett. **84**, 35 (2000).
70. H. Scheit, T. Glasmacher, R.W. Ibbotson, P.G. Thirolf, Nucl. Instrum. Methods Phys. Res. A **422**, 124 (1999).
71. J. Cub, G. Stengel, A. Grünschloß, K. Boretzky, T. Aumann, W. Dostal, B. Eberlein, Th.W. Elze, H. Emling, J. Holeczek, G. Ickert, J. Holeczek, R. Holzmann, J.V. Kratz, R. Kulessa, Y. Leifels, H. Simon, K. Stelzer, J. Stroth, A. Surowiec, E. Wajda, Nucl. Instrum. Methods Phys. Res. A **402**, 67 (1998).
72. A. Leistenschneider, T. Aumann, K. Boretzky, L.F. Canto, B.V. Carlson, D. Cortina, U. Datta Pramanik, Th.W. Elze, H. Emling, H. Geissel, A. Grünschloß, K. Helariutta, M. Hellström, M.S. Hussein, S. Ilievski,

K. Jones, J.V. Kratz, R. Kulessa, Le Hong Khiem, E. Lubkiewicz, G. Münzenberg, R. Palit, P. Reiter, C. Scheidenberger, K.-H. Schmidt, H. Simon, K. Sümmerer, E. Wajda, W. Walús, Phys. Rev. C **65**, 064607 (2002).
73. T. Blaich, Th.W. Elze, H. Emling, H. Freiesleben, K. Grimm, W. Henning, R. Holzmann, G. Ickert, J.G. Keller, H. Klingler, W. Kneissl, R. Knig, R. Kulessa, J.V. Kratz, D. Lambrecht, J.S. Lange, Y. Leifels, E. Lubkiewicz, M. Proft, W. Prokopowicz, C. Schtter, R. Schmidt, H. Spies, K. Stelzer, J. Stroth, W. Walús, E. Wajda, H.J. Wollersheim, M. Zinser, E. Zude, Nucl. Instrum. Methods Phys. Res. A **314**, 136 (1992).
74. V. Metag, D. Habs, D. Schwalm, Comments Nucl. Part. Phys. **16**, 213 (1986).
75. R.C. Johnson, P.J.R. Soper, Phys. Rev. C **1**, 976 (1970).
76. N.K. Timofeyuk, R.C. Johnson, Phys. Rev. C **59**, 1545 (1999).
77. S. Fortier, S. Pita, J.S. Winfield, W.N. Catford, N.A. Orr, J. Van de Wiele, Y. Blumenfeld, R. Chapman, S.P.G. Chappell, N.M. Clarke, N. Curtis, M. Freer, S. Galès, K.L. Jones, H. Langevin-Joliot, H. Laurent, I. Lhenry, J.M. Maison, P. Roussel-Chomaz, M. Shawcross, M. Smith, K. Spohr, T. Suomijärvi, A. de Vismes, Phys. Lett. B **461**, 22 (1999).
78. J.S. Winfield, S. Fortier, W.N. Catford, S. Pita, N.A. Orr, J. Van de Wiele, Y. Blumenfeld, R. Chapman, S.P.G. Chappell, N.M. Clarke, N. Curtis, M. Freer, S. Galès, H. Langevin-Joliot, H. Laurent, I. Lhenry, J.M. Maison, P. Roussel-Chomaz, M. Shawcross, K. Spohr, T. Suomijärvi, A. de Vismes, Nucl. Phys. A **683**, 48 (2001).
79. E. Sauvan, F. Carstoiu, N.A. Orr, J.C. Angélique, W.N. Catford, N.M. Clarke, M. Mac Cormick, N. Curtis, M. Freer, S. Grévy, C. Le Brun, M. Lewitiwicz, E. Liégard, F.M. Marqués, P. Roussel-Chomaz, M.-G. Saint Laurent, M. Shawcross, J.S. Winfield, Phys. Lett. B **491**, 1 (2000).
80. E. Sauvan, F. Carstoiu, N.A. Orr, J.S. Winfield, M. Freer, J.C. Angélique, W.N. Catford, N.M. Clarke, N. Curtis, S. Grévy, C. Le Brun, M. Lewitiwicz, E. Liégard, F.M. Marqués, M. Mac Cormick, P. Roussel-Chomaz, M.-G. Saint Laurent, M. Shawcross, Phys. Rev. C **69**, 044603 (2004).
81. S. Typel, G. Baur, Phys. Rev. C **64**, 024601 (2001).
82. K. Hencken, G. Bertsch, H. Esbensen, Phys. Rev. C **54**, 3043 (1996).
83. G.F. Bertsch, K. Hencken, H. Esbensen, Phys. Rev. C **57**, 1366 (1998).
84. J.A. Tostevin, J. Phys. G **25**, 735 (1999).
85. J.A. Tostevin, D. Bazin, B.A. Brown, T. Glasmacher, P.G. Hansen, V. Maddalena, A. Navin, B.M. Sherrill, Phys. Rev. C **66**, 024607 (2002).
86. H. Esbensen, G.F. Bertsch, Phys. Rev. C **64**, 014608 (2001).
87. T. Baumann, M.J.G. Borge, H. Geissel, H. Lenske, K. Markenroth, W. Schwab, M.H. Smedberg, T. Aumann, L. Axelsson, U. Bergmann, D. Cortina-Gil, L. Fraile, M. Hellström, M. Ivanov, N. Iwasa, R. Janik, B. Jonson, G. Münzenberg, F. Nickel, T. Nilsson, A. Ozawa, A. Richter, K. Riisager, C. Scheidenberger, G. Schrieder, H. Simon, B. Sitar, P. Strmen, K. Sümmerer, T. Suzuki, M. Winkler, H. Wollnik, M.V. Zhukov, Phys. Lett. B **439**, 256 (1998).
88. T. Aumann, L.V. Chulkov, V.N. Pribora, M.H. Smedberg, Nucl. Phys. A **640**, 24 (1998).
89. J. Hüfner, M.C. Nemes, Phys. Rev. C **23**, 2538 (1981).
90. M.H. Smedberg, T. Baumann, T. Aumann, L. Axelsson, U. Bergmann, M.J.G. Borge, D. Cortina-Gil, L. Fraile, H. Geissel, L. Grigorenko, M. Hellström, M. Ivanov, N. Iwasa, R. Janik, B. Jonson, H. Lenske, K. Markenroth, G. Münzenberg, T. Nilsson, A. Richter, K. Riisager, C. Scheidenberger, G. Schrieder, W. Schwab, H. Simon, B. Sitar, P. Strmen, K. Sümmerer, M. Winkler, M.V. Zhukov, Phys. Lett. B **452**, 1 (1999).
91. H. Esbensen, Phys. Rev. C **53**, 2007 (1996).
92. P.G. Hansen, Phys. Rev. Lett. **77**, 1016 (1996).
93. F. Carstoiu, E. Sauvan, N.A. Orr, A. Bonaccorso, Phys. Rev. C **70**, 054602 (2004).
94. C.A. Bertulani, P.G. Hansen, Phys. Rev. C **70**, 034609 (2004).
95. W. Geithner, S. Kappertz, M. Keim, P. Lievens, R. Neugart, L. Vermeeren, S. Wilbert, V.N. Fedoseyev, U. Köster, V.I. Mishin, V. Sebastian, the ISOLDE Collaboration, Phys. Rev. Lett. **83**, 3792 (1999).
96. E. Garrido, D.V. Fedorov, A.S. Jensen, Phys. Lett. B **600**, 208 (2004).
97. D. Aleksandrov, T. Aumann, L. Axelsson, T. Baumann, M.J.G. Borge, L.V. Chulkov, J. Cub, W. Dostal, B. Eberlein, Th.W. Elze, H. Emling, H. Geissel, V.Z. Goldberg, M. Golovkov, A. Grünschloss, M. Hellström, J. Holeczek, R. Holzmann, B. Jonson, A.A. Korshenninikov, J.V. Kratz, G. Kraus, R. Kulessa, Y. Leifels, A. Leistenschneider, T. Leth, I. Mukha, G. Münzenberg, F. Nickel, T. Nilsson, G. Nyman, B. Petersen, M. Pfützner, A. Richter, K. Riisager, C. Scheidenberger, G. Schrieder, W. Schwab, H. Simon, M.H. Smedberg, M. Steiner, J. Stroth, A. Surowiec, T. Suzuki, O. Tengblad, M.V. Zhukov, Nucl. Phys. A **633**, 234 (1998).
98. L.V. Chulkov, T. Aumann, D. Aleksandrov, L. Axelsson, T. Baumann, M.J.G. Borge, R. Collatz, J. Cub, W. Dostal, B. Eberlein, Th.W. Elze, H. Emling, H. Geissel, V.Z. Goldberg, M. Golovkov, A. Grünschloss, M. Hellström, J. Holeczek, R. Holzmann, B. Jonson, A.A. Korshenninikov, J.V. Kratz, G. Kraus, R. Kulessa, Y. Leifels, A. Leistenschneider, T. Leth, I. Mukha, G. Münzenberg, F. Nickel, T. Nilsson, G. Nyman, B. Petersen, M. Pfützner, A. Richter, K. Riisager, C. Scheidenberger, G. Schrieder, W. Schwab, H. Simon, M.H. Smedberg, M. Steiner, J. Stroth, A. Surowiec, T. Suzuki, O. Tengblad, Phys. Rev. Lett. **79**, 201 (1997).
99. T. Aumann, L.V. Chulkov, in *ENAM98 Exotic Nuclei and Atomic Masses*, edited by B.M. Sherrill, D.J. Morrissey, C.N. Davids, AIP Conf. Proc. **455**, 196 (1998).
100. Y. Yariv, Z. Fraenkel, Phys. Rev. C **20**, 2227 (1979).
101. A.A. Korsheninnikov, T. Kobayashi, Nucl. Phys. A **567**, 97 (1994).
102. F. Barranco, E. Vigezzi, R.A. Broglia, Phys. Lett. B **319**, 387 (1993).
103. F. Barranco, E. Vigezzi, R.A. Broglia, Z. Phys. A **356**, 45 (1996).
104. F. Barranco, E. Vigezzi, in *International School of Heavy Ion Physics, 4th course: Exotic Nuclei*, edited by R.A. Broglia, P.G. Hansen (World Scientific, 1998) p. 217.
105. M. Zinser, F. Humbert, T. Nilsson, W. Schwab, Th. Blaich, M.J.G. Borge, L.V. Chulkov, H. Eickhoff, Th.W. Elze, H. Emling, B. Franzke, H. Freiesleben, H. Geissel, K. Grimm, D. Guillemaud-Mueller, P.G. Hansen, R. Holzmann, H. Irnich, B. Jonson, J.G. Keller, O. Klepper, H. Klingler, J.V. Kratz, R. Kulessa, D. Lambrecht, Y. Leifels, A. Magel, M. Mohar, A.C. Mueller,

G. Münzenberg, F. Nickel, G. Nyman, A. Richter, K. Riisager, C. Scheidenberger, G. Schrieder, B.M. Sherrill, H. Simon, K. Stelzer, J. Stroth, O. Tengblad, W. Trautmann, E. Wajda, E. Zude, Phys. Rev. Lett. **75**, 1719 (1995).
106. E. Garrido, D.V. Fedorov, A.S. Jensen, Nucl. Phys. A **617**, 153 (1997).
107. J. Wurzer, H.M. Hofmann, Phys. Rev. C. **55**, 688 (1997).
108. B.V. Danilin, M.V. Zhukov, A.A. Korsheninnikov, L.V. Chulkov, Yad. Fiz. **53**, 71 (1991), (Sov. J. Nucl. Phys. **53**, 45 (1991)).
109. G. Audi, A.H. Wapstra, C. Thibault, Nucl. Phys. A **729**, 337 (2003).
110. L.V. Chulkov, G. Schrieder, Z. Phys. A **359**, 231 (1997).
111. G. Baur, C.A. Bertulani, Nucl. Phys. A **480**, 615 (1988).
112. G. Baur, C.A. Bertulani, H. Rebel, Nucl. Phys. A **458**, 188 (1986).
113. C.A. Bertulani, G. Baur, Phys. Rep. **163**, 299 (1988).
114. C.J. Benesh, B.C. Cook, J.P. Vary, Phys. Rev. C **40**, 1198 (1989).
115. T. Aumann, C.A. Bertulani, K. Sümmerer, Phys. Rev. C **51**, 416 (1995).
116. F. Ajzenberg-Selove, Nucl. Phys. A **490**, 1 (1999).
117. T. Otsuka, M. Ishihara, N. Fukunishi, T. Nakamura, M. Yokoyama, Phys. Rev. C **49**, R2289 (1994).
118. D. Ridikas, M.H. Smedberg, J.S. Vaagen, M.V. Zhukov, Nucl. Phys. A **628**, 363 (1998).
119. M.B. Chadwick, P.G. Young, Nucl. Sci. Eng. **123**, 1 (1996); M.B. Chadwick, M. Blann, L.J. Cox, P.G. Young, A.S. Meigooni, Nucl. Sci. Eng. **123**, 17 (1996).
120. S. Typel, G. Baur, Phys. Rev. Lett. **93**, 142502 (2004).
121. J. Wang, A. Galonsky, J.J. Kruse, E. Tryggestad, R.H. White-Stevens, P.D. Zecher, Y. Iwata, K. Ieki, Á. Horváth, F. Deák, Á. Kiss, Z. Seres, J.J. Kolata, J. von Schwarzenberg, R.E. Warner, H. Schelin, Phys. Rev. C **63**, 034306 (2002).
122. M. Meister, K. Markenroth, D. Aleksandrov, T. Aumann, T. Baumann, M.J.G. Borge, L.V. Chulkov, D. Cortina-Gil, B. Eberlein, Th.W. Elze, H. Emling, H. Geissel, M. Hellström, B. Jonson, J.V. Kratz, R. Kulessa, A. Leistenschneider, I. Mukha, G. Münzenberg, F. Nickel, T. Nilsson, G. Nyman, M. Pfützner, V. Pribora, A. Richter, K. Riisager, C. Scheidenberger, G. Schrieder, H. Simon, O. Tengblad, M.V. Zhukov, Nucl. Phys. A **700**, 3 (2002).
123. Y. Iwata, K. Ieki, A. Galonsky, J.J. Kruse, J. Wang, R.H. White-Stevens, E. Tryggestad, P.D. Zecher, F. Deák, Á. Horváth, Á. Kiss, Z. Seres, J.J. Kolata, J. von Schwarzenberg, R.E. Warner, H. Schelin, Phys. Rev. C **62**, 064311 (2002).
124. B.V. Danilin, I.J. Thompson, J.S. Vaagen, M.V. Zhukov, Nucl. Phys. A **632**, 383 (1998).
125. A. Cobis, D. Fedorov, A. Jensen, Phys. Rev. Lett. **79**, 2411 (1997).
126. S.N. Ershov, B.V. Danilin, J.S. Vaagen, Phys. Rev. C **64**, 064609 (2001).
127. B.V. Danilin, T. Rodge, J.S. Vaagen, I.J. Thompson, M.V. Zhukov, Phys. Rev. C **69**, 024609 (2004).
128. L.V. Chulkov, H. Simon, I.J. Thompson, T. Aumann, M.J.G. Borge, Th.W. Elze, H. Emling, H. Geissel, L.V. Grigorenko, M. Hellström, B. Jonson, J.V. Kratz, R. Kulessa, K. Markenroth, M. Meister, G. Münzenberg, F. Nickel, T. Nilsson, G. Nyman, V. Pribora, A. Richter, K. Riisager, C. Scheidenberger, G. Schrieder, O. Tengblad, M.V. Zhukov, Nucl. Phys. A **759**, 23 (2005).
129. A. Bohr, B.R. Mottelson, *Nuclear Structure*, Vol. **2** (Benjamin, London, 1975).
130. Y. Alhassid, M. Gai, G.F. Bertsch, Phys. Rev. Lett. **49**, 1482 (1982).
131. H. Sagawa, M. Honma, Phys. Lett. B **251**, 17 (1990).
132. K. Hencken, G. Baur, D. Trautmann, Nucl. Phys. A **733**, 200 (2004).
133. B.V. Danilin, M.V. Zhukov, J.S. Vaagen, J.M. Bang, Phys. Lett. B **302**, 129 (1993).
134. H. Esbensen, G.F. Bertsch, Nucl. Phys. A **542**, 310 (1992).
135. J.M. Bang, L.S. Ferreira, E. Maglione, Europhys. Lett. **18**, 679 (1992).
136. S. Funuda, H. Kameyama, Y. Sakuragi, Nucl. Phys. A **575**, 93 (1994).
137. H. Simon, D. Aleksandrov, T. Aumann, L. Axelsson, T. Baumann, M.J.G. Borge, L.V. Chulkov, R. Collatz, J. Cub, W. Dostal, B. Eberlein, Th.W. Elze, H. Emling, H. Geissel, A. Grünschloß, M. Hellström, J. Holeczek, R. Holzmann, B. Jonson, J.V. Kratz, G. Kraus, R. Kulessa, Y. Leifels, A. Leistenschneider, T. Leth, I. Mukha, G. Münzenberg, F. Nickel, T. Nilsson, G. Nyman, B. Petersen, M. Pfützner, A. Richter, K. Riisager, C. Scheidenberger, G. Schrieder, W. Schwab, M.H. Smedberg, J. Stroth, A. Surowiec, O. Tengblad, M.V. Zhukov, Phys. Rev. Lett. **83**, 496 (1999).
138. H. Simon, T. Aumann, M.J.G. Borge, L.V. Chulkov, Th.W. Elze, H. Emling, C. Forssén, H. Geissel, M. Hellström, B. Jonson, J.V. Kratz, R. Kulessa, Y. Leifels, K. Markenroth, M. Meister, G. Münzenberg, F. Nickel, T. Nilsson, G. Nyman, V. Pribora, A. Richter, K. Riisager, C. Scheidenberger, G. Schrieder, O. Tengblad, M.V. Zhukov, Nucl. Phys. A **734**, 323 (2004).
139. H. Iwasaki, T. Motobayashi, H. Akiyoshi, Y. Ando, N. Fukuda, H. Fujiwara, Zs. Fülöp, K.I. Hahn, Y. Higurashi, M. Hiraia, I. Hisanaga, N. Iwasa, T. Kijima, T. Minemura, T. Nakamura, M. Notani, S. Ozawa, H. Sakurai, S. Shimoura, S. Takeuchi, T. Teranishi, Y. Yanagisawa, M. Ishihara, Phys. Lett. B **481**, 7 (2000).
140. H. Iwasaki, T. Motobayashi, H. Akiyoshi, Y. Ando, N. Fukuda, H. Fujiwara, Zs. Fülöp, K.I. Hahn, Y. Higurashi, M. Hiraia, I. Hisanaga, N. Iwasa, T. Kijima, A. Mengoni, T. Minemura, T. Nakamura, M. Notani, S. Ozawa, H. Sagawa, H. Sakurai, S. Shimoura, S. Takeuchi, T. Teranishi, Y. Yanagisawa, M. Ishihara, Phys. Lett. B **491**, 8 (2000).
141. J. Meng, P. Ring, Phys. Rev. Lett. **77**, 3963 (1996).
142. F. Barranco, P.F. Bortignon, R.A. Broglia, G. Cólo, E. Vigezzi, Eur. Phys. J. A **11**, 385 (2001).
143. G. Gori, F. Barranco, E. Vigezzi, R.A. Broglia, Phys. Rev. C **69**, 041302 (2004).
144. M. Meister, K. Markenroth, D. Aleksandrov, T. Aumann, L. Axelsson, T. Baumann, M.J.G. Borge, L.V. Chulkov, W. Dostal, B. Eberlein, Th.W. Elze, H. Emling, C. Forssén, H. Geissel, M. Hellström, R. Holzmann, B. Jonson, J.V. Kratz, R. Kulessa, Y. Leifels, A. Leistenschneider, I. Mukha, G. Münzenberg, F. Nickel, T. Nilsson, G. Nyman, A. Richter, K. Riisager, C. Scheidenberger, G. Schrieder, H. Simon, O. Tengblad, M.V. Zhukov, Phys. Rev. Lett. **88**, 102501 (2002).
145. K. Markenroth, M. Meister, B. Eberlein, D. Aleksandrov, T. Aumann, L. Axelsson, T. Baumann, M.J.G. Borge, L.V. Chulkov, W. Dostal, Th.W. Elze, H. Emling,

H. Geissel, A. Grünschloß, M. Hellström, J. Holeczek, B. Jonson, J.V. Kratz, G. Kraus, R. Kulessa, A. Leistenschneider, I. Mukha, G. Münzenberg, F. Nickel, T. Nilsson, G. Nyman, M. Pfützner, V. Pribora, A. Richter, K. Riisager, C. Scheidenberger, G. Schrieder, H. Simon, J. Stroth, O. Tengblad, M.V. Zhukov, Nucl. Phys. A **679**, 462 (2001).

146. D.R. Tilley, C.M. Cheves, J.L. Godwin, G.M. Hale, H.M. Hofmann, J.H. Kelley, C.G. Sheu, H.R. Weller, Nucl. Phys. A **708**, 3 (2002).
147. S. Aoyama, Phys. Rev. C **59**, 531 (1999).
148. A. Csótó, G.M. Hale, Phys. Rev. C **55**, 536 (1997).
149. N.A.F.M. Poppelier, A.A. Wolters, P.W.M. Glaudemans, Z. Phys. A **346**, 11 (1993).
150. P. Navrátil, B.R. Barrett, Phys. Rev. C **57**, 3119 (1998).
151. R.B. Wiringa, S.C. Pieper, J. Carlson, V.R. Pandharipande, Phys. Rev. C **62**, 014001 (2000).
152. S.C. Pieper, V.R. Pandharipande, R.B. Wiringa, J. Carlson, Phys. Rev. C **64**, 014001 (2001).
153. D. Halderson, Nucl. Phys. A **707**, 65 (2002).
154. D. Halderson, Phys. Rev. C **70**, 041603 (2004).
155. G.V. Rogachev, P. Boutachkov, A. Aprahamian, F.D. Becchetti, J.P. Bychowski, Y. Chen, G. Chubarian, P.A. DeYoung, V.Z. Goldberg, J.J. Kolata, L.O. Lamm, G.F. Peaslee, M. Quinn, B.B. Skorodumov, A. Wöhr, Phys. Rev. Lett. **92**, 232502 (2004).
156. M. Meister, L.V. Chulkov, H. Simon, T. Aumann, M.J.G. Borge, W. Dostal, Th.W. Elze, H. Emling, H. Geissel, M. Hellström, B. Jonson, J.V. Kratz, R. Kulessa, Y. Leifels, K. Markenroth, G. Münzenberg, F. Nickel, T. Nilsson, G. Nyman, V. Pribora, A. Richter, K. Riisager, C. Scheidenberger, G. Schrieder, O. Tengblad, Nucl. Phys. A **723**, 13 (2003).
157. N.B. Shulgina, B.V. Danilin, L.V. Grigorenko, M.V. Zhukov, J.M. Bang, Phys. Rev. C **62**, 014312 (2000).
158. M. Meister, L.V. Chulkov, H. Simon, T. Aumann, M.J.G. Borge, W. Dostal, Th.W. Elze, H. Emling, H. Geissel, M. Hellström, B. Jonson, J.V. Kratz, R. Kulessa, Y. Leifels, K. Markenroth, G. Münzenberg, F. Nickel, T. Nilsson, G. Nyman, V. Pribora, A. Richter, K. Riisager, C. Scheidenberger, G. Schrieder, O. Tengblad, M.V. Zhukov, Phys. Rev. Lett. **91**, 162504 (2003).
159. A.A. Korsheninnikov, M.S. Golovkov, I. Tanihata, A. M. Rodin, A.S. Fomichev, S.I. Sidorchuk, S.V. Stepantsov, M.L. Chelnokov, V.A. Gorshkov, D.D. Bogdanov, R. Wolski, G.M. Ter-Akopian, Yu.Ts. Oganessian, W. Mittig, P. Roussel-Chomaz, H. Savajols, E.A. Kuzmin, E.Yu. Nikolskii, A.A. Ogloblin, Phys. Rev. Lett. **87**, 092501 (2001).
160. M.S. Golovkov, L.V. Grigorenko, A.S. Fomichev, S.A. Krupko, Yu.Ts. Oganessian, A.M. Rodin, S.I. Sidorchuk, R.S. Slepnev, S.V. Stepantsov, G.M. Ter-Akopian, R. Wolski, M.G. Itkis, A.A. Bogatchev, N.A. Kondratiev, E.M. Kozulin, A.A. Korsheninnikov, E.Yu. Nikolskii, P. Roussel-Chomaz, W. Mittig, R. Palit, V. Bouchat, V. Kinnard, T. Materna, F. Hanappe, O. Dorvaux, L. Stuttg, C. Angulo, V. Lapoux, R. Raabe, L. Nalpas, A.A. Yukhimchuk, V.V. Perevozchikov, Yu.I. Vinogradov, S.K. Grishechkin, S. V. Zlatoustovskiy, Phys. Rev. Lett. **93**, 262501 (2004).
161. D. Guillemaud-Mueller, J.C. Jacmart, E. Kashy, A. Latimier, A.C. Mueller, F. Pougheon, A. Richard, Yu.E. Penionzhkevich, A.G. Artuhk, A.V. Belozyorov, S.M. Lukyanov, R. Anne, P. Bricault, C. Détraz, M. Lewitowicz, Y. Zhang, Yu.S. Lyutostansky, M.V. Zverev, D. Bazin, W.D. Schmidt-Ott, Phys. Rev. C **41**, 937 (1990).
162. M. Fauerbach, D.J. Morrissey, W. Benenson, B.A. Brown, M. Hellström, J.H. Kelley, R.A. Kryger, R. Pfaff, C.F. Powell, B.M. Sherrill, Phys. Rev. C **53**, 647 (1996).
163. O. Tarasov, R. Allatt, J.C. Angélique, R. Anne, C. Borcea, Z. Dlouhy, C. Donzaud, S. Grévy, D. Guillemaud-Mueller, M. Lewitowicz, S. Lukyanov, A.C. Mueller, F. Nowacki, Yu. Oganessian, N.A. Orr, A.N. Ostrowski, R.D. Page, Yu. Penionzhkevich, F. Pougheon, A. Reed, M.G. Saint-Laurent, W. Schwab, E. Sokol, O. Sorlin, W. Trinder, J.S. Winfield, Phys. Lett. B **409**, 64 (1997).
164. H. Sakurai, S.M. Lukyanov, M. Notani, N. Aoi, D. Beaumel, N. Fukuda, M. Hirai, E. Ideguchi, N. Imai, M. Ishihara, H. Iwasaki, T. Kubo, K. Kusaka, H. Kumagai, T. Nakamura, H. Ogawa, Yu. E. Penionzhkevich, T. Teranishi, Y.X. Watanabe, K. Yoneda, A. Yoshida, Phys. Lett. B **448**, 180 (1999).
165. A. Ozawa, O. Bochkarev, L. Chulkov, D. Cortina, H. Geissel, M. Hellström, M. Ivanov, R. Janik, K. Kimura, T. Kobayashi, A.A. Korsheninnikov, G. Münzenberg, F. Nickel, A.A. Ogloblin, M. Pfützner, V. Pribora, H. Simon, B. Sitár, P. Strmen, K. Sümmerer, T. Suzuki, I. Tanihata, M. Winkler, K. Yoshida, Nucl. Phys. A **673**, 411 (2000).
166. M. Stanoiu, F. Azaiez, Zs. Dombrádi, O. Sorlin, B.A. Brown, M. Belleguic, D. Sohler, M.G. Saint Laurent, M.J. Lopez-Jimenez, Y.E. Penionzhkevich, G. Sletten, N.L. Achouri, J.C. Angélique, F. Becker, C. Borcea, C. Bourgeois, A. Bracco, J.M. Daugas, Z. Dlouhý, C. Donzaud, J. Duprat, Zs. Fülöp, D. Guillemaud-Mueller, S. Grévy, F. Ibrahim, A. Kerek, A. Krasznahorkay, M. Lewitowicz, S. Leenhardt, S. Lukyanov, P. Mayet, S. Mandal, H. van der Marel, W. Mittig, J. Mrázek, F. Negoita, F. De Oliveira-Santos, Zs. Podolyák, F. Pougheon, M.G. Porquet, P. Roussel-Chomaz, H. Savajols, Y. Sobolev, C. Stodel, J. Timár, A. Yamamoto, Phys. Rev. C **69**, 034312 (2004).
167. R. Kanungo, I. Tanihata, A. Ozawa, Phys. Lett. B **528**, 58 (2002).
168. R. Kanungo, M. Chiba, N. Iwasa, S. Nishimura, A. Ozawa, C. Samanta, T. Suda, T. Suzuki, T. Yamaguchi, T. Zheng, I. Tanihata, Phys. Rev. Lett. **88**, 142502 (2002).
169. B.A. Brown, P.G. Hansen, J.A. Tostevin, Phys. Rev. Lett. **90**, 159201 (2003).
170. D. Cortina-Gil, J. Fernandez-Vazquez, T. Aumann, T. Baumann, J. Benlliure, M.J.G. Borge, L.V. Chulkov, U. Datta Pramanik, C. Forssén, L.M. Fraile, H. Geissel, J. Gerl, F. Hammache, K. Itahashi, R. Janik, B. Jonson, S. Mandal, K. Markenroth, M. Meister, M. Mocko, G. Münzenberg, T. Ohtsubo, A. Ozawa, Y. Prezado, V. Pribora, K. Riisager, H. Scheit, R. Schneider, G. Schrieder, H. Simon, B. Sitar, A. Stolz, P. Strmen, K. Sümmerer, I. Szarka, H. Weick, Phys. Rev. Lett. **93**, 062501 (2004).
171. R. Palit, P. Adrich, T. Aumann, K. Boretzky, D. Cortina, U. Datta Pramanik, Th.W. Elze, H. Emling, M. Fallot, H. Geissel, M. Hellström, K.L. Jones, L.H. Khiem, J.V. Kratz, R. Kulessa, Y. Leifels, A. Leistenschneider, G. Münzenberg, C. Nociforo, P. Reiter, H. Simon, K. Sümmerer, W. Walus, Nucl. Phys. A **731**, 235 (2004).

172. S. Burzynski, M. Baumgartner, H.P. Gubler, J. Jourdan, H.O. Meyer, G.R. Plattner, H.W. Roser, I. Sick, K.-H. Möbius, Nucl. Phys. A **399**, 230 (1983).
173. J.R. Terry, D. Bazin, B.A. Brown, J. Enders, T. Glasmacher, P.G. Hansen, B.M. Sherrill, J.A. Tostevin, Phys. Rev. C **69**, 054306 (2004).
174. C.M. Perey, F.G. Perey, At. Data Nucl. Data Tables **17**, 1 (1976).
175. J.-P. Jeukenne, A. Lejeune, C. Mahaux, Phys. Rev. C **16**, 80 (1977).
176. G. Murillo, S. Sen, S.E. Darden, Nucl. Phys. A **579**, 125 (1994).
177. J.D. Goss, P.L. Jolivette, C.P. Browne, S.E. Darden, H.R. Weller, R.A. Blue, Phys. Rev. C **12**, 1730 (1975).
178. F.E. Cecil, J.R. Shepard, R.E. Anderson, R.J. Peterson, P. Kaczkowski, Nucl. Phys. A **255**, 243 (1975).
179. E.K. Warburton, B.A. Brown, Phys. Rev. C **46**, 923 (1992).
180. B.A. Brown, P.G. Hansen, B.M. Sherrill, J.A. Tostevin, Phys. Rev. C **65**, 061601(R) (2002).
181. J. Enders, T. Baumann, B.A. Brown, N.H. Frank, P.G. Hansen, P.R. Heckman, B.M. Sherrill, A. Stolz, M. Thoennessen, J.A. Tostevin, E.J. Tryggestad, S. Typel, M.S. Wallace, Phys. Rev. C **67**, 064301 (2003).
182. G.J. Kramer, H.P. Blok, L. Lapikas, Nucl. Phys. A **679**, 267 (2001).
183. *An International Accelerator Facility for Beams of Ions and Antiprotons*, Conceptual Design Report, Publisher GSI (2001), `http://www.gsi.de/GSI-Future/cdr/`.
184. The NUSTAR Letters of Intent, `http://www.gsi.de/forschung/kp/kp2/nustar.html`.
185. A. Gade, D. Bazin, B.A. Brown, C.M. Campbell, J.A. Church, D.C. Dinca, J. Enders, T. Glasmacher, P.G. Hansen, Z. Hu, K.W. Kemper, W.F. Mueller, H. Olliver, B.C. Perry, L.A. Riley, B.T. Roeder, B.M. Sherrill, J.R. Terry, J.A. Tostevin, K.L. Yurkewicz, Phys. Rev. Lett. **93**, 042501 (2004).
186. R. Lemmon *et al.*, *Quasifree Hadronic Scattering Studies of Exotic Nuclei*, GSI Experiment proposal S296 (2004), unpublished.
187. L.V. Chulkov, F. Aksouh, A. Bleile, O.V. Bochkarev, D. Cortina-Gil, A.V. Dobrovolsky, P. Egelhof, H. Geissel, M. Hellström, N.B. Isaev, O.A. Kiselev, B.G. Komkov, M. Matoš, F.N. Moroz, G. Münzenberg, M. Mutterer, V.A. Mylnikov, S.R. Neumaier, V.N. Pribora, D.M. Seliverstov, L.O. Sergeev, A. Shrivastava, K. Sümmerer, S. Yu. Torilov, H. Weick, M. Winkler, V.I. Yatsoura, Nucl. Phys. A **759**, 43 (2005).
188. S. Wan, J. Gerl, J. Cub, J. Holeczek, P. Reiter, D. Schwalm, T. Aumann, K. Boretzky, W. Dostal, B. Eberlein, H. Emling, Ch. Ender, Th.W. Elze, H. Geissel, A. Grünschloß, R. Holzmann, N. Iwasa, M. Kaspar, A. Kleinböhl, O. Koschorrek, Y. Leifels, A. Leistenschneider, I. Peter, H. Schaffner, C. Scheidenberger, R. Schubart, R. Schubert, H. Simon, G. Stengel, A. Surowiec, H.J. Wollersheim, Eur. Phys. J. A **6**, 167 (1999).
189. T. Glasmacher, Annu. Rev. Nucl. Part. Sci. **48**, 1 (1998).
190. K. Boretzky, A. Grünschloß, S. Ilievski, P. Adrich, T. Aumann, C.A. Bertulani, J. Cub, W. Dostal, B. Eberlein, Th.W. Elze, H. Emling, M. Fallot, J. Holeczek, R. Holzmann, C. Kozhuharov, J.V. Kratz, R. Kulessa, Y. Leifels, E. Lubkiewicz, G. Mordechai, T. Ohtsuki, P. Reiter, H. Simon, K. Stelzer, J. Stroth, K. Sümmerer, A. Surowiec, E. Wajda, W. Walus, Phys. Rev. C **68**, 024317 (2003).
191. S. Ilievski, T. Aumann, K. Boretzky, Th.W. Elze, H. Emling, A. Grünschloß, J. Holeczek, R. Holzmann, C. Kozhuharov, J.V. Kratz, R. Kulessa, A. Leistenschneider, E. Lubkiewicz, T. Ohtsuki, P. Reiter, H. Simon, K. Stelzer, J. Stroth, K. Sümmerer, E. Wajda, W. Walus, Phys. Rev. Lett. **92**, 112502 (2004).
192. A. Winther, K. Alder, Nucl. Phys. A **319**, 518 (1979).
193. A. Grünschloß, K. Boretzky, T. Aumann, C.A. Bertulani, J. Cub, W. Dostal, B. Eberlein, Th.W. Elze, H. Emling, J. Holeczek, R. Holzmann, M. Kaspar, J.V. Kratz, R. Kulessa, Y. Leifels, A. Leistenschneider, E. Lubkiewicz, S. Mordechai, I. Peter, P. Reiter, M. Rejmund, H. Simon, K. Stelzer, A. Surowiec, K. Sümmerer, J. Stroth, E. Wajda, W. Walus, S. Wan, H.J. Wollersheim, Phys. Rev. C **60**, 051601 (1999).
194. E.G. Fuller, Phys. Rep. **127**, 187 (1985); B.L. Berman, At. Data Nucl. Data Tables **15**, 319 (1975).
195. J.G. Woodworth, K.G. McNeill, J.W. Jury, R.A. Alvarez, B.L. Berman, D.D. Faul, P. Meyer, Phys. Rev. C **19**, 1667 (1979).
196. U. Kneissl, K.H. Leister, H.O. Neidel, A. Weller, Nucl. Phys. A **272**, 125 (1976).
197. Y. Alhassid, M. Gai, G.F. Bertsch, Phys. Rev. Lett. **49**, 1482 (1982).
198. E. Tryggestad, T. Aumann, T. Baumann, D. Bazin, J.R. Beene, Y. Blumenfeld, B.A. Brown, M. Chartier, M.L. Halbert, P. Heckman, J.F. Liang, D.C. Radford, D. Shapira, M. Thoennessen, R.L. Varner, Phys. Lett. B **541**, 52 (2002).
199. E. Tryggestad, T. Baumann, P. Heckman, M. Thoennessen, T. Aumann, D. Bazin, Y. Blumenfeld, J.R. Beene, T.A. Lewis, D.C. Radford, D. Shapira, R.L. Varner, M. Chartier, M.L. Halbert, J.F. Liang, Phys. Rev. C **67**, 064309 (2003).
200. J.R. Beene, F.E. Bertrand, D.J. Horen, R.L. Auble, B.L. Burks, J. Gomez del Campo, M.L. Halbert, R.O. Sayer, W. Mittig, Y. Schutz, J. Barrette, N. Alamanos, F. Auger, B. Fernandez, A. Gillibert, B. Haas, J.P. Vivien, Phys. Rev. C **41**, 920 (1990).
201. N. Ryezayeva, T. Hartmann, Y. Kalmykov, H. Lenske, P. von Neumann-Cosel, V.Yu. Ponomarev, A. Richter, A. Shevchenko, S. Volz, J. Wambach, Phys. Rev. Lett. **89**, 272502 (2002).
202. A. Zilges, S. Volz, M. Babilon, T. Hartmann, P. Mohr, K. Vogt, Phys. Lett. B **542**, 43 (2002).
203. A. Zilges, Nucl. Phys. A **731**, 249 (2004).
204. T. Hartmann, M. Babilon, S. Kamerdzhiev, E. Litvinova, D. Savran, S. Volz, A. Zilges, Phys. Rev. Lett. **93**, 192501 (2004).
205. T. Hartmann, J. Enders, P. Mohr, K. Vogt, S. Volz, A. Zilges, Phys. Rev. C **65**, 034301 (2002).
206. P. Adrich, A. Klimkiewicz, M. Fallot, K. Boretzky, T. Aumann, D. Cortina-Gil, U. Datta Pramanik, Th.W. Elze, H. Emling, H. Geissel, M. Hellström, K.L. Jones, J.V. Kratz, R. Kulessa, Y. Leifels, C. Nociforo, R. Palit, H. Simon, G. Surówka, K. Sümmerer, W. Walus, Phys. Rev. Lett. **95**, 132501 (2005).
207. S.C. Fultz, B.L. Berman, J.T. Caldwell, R.L. Bramblett, M.A. Kelley, Phys. Rev. **186**, 1255 (1969).
208. B.V. Danilin, J.S. Vaagen, S.N. Ershov, H. Heiberg-Andersen, I.J. Thompson, M.V. Zhukov, Phys. Rev. C **55**, R577 (1997).

209. D. Aleksandrov, T. Aumann, L. Axelsson, T. Baumann, M.J.G. Borge, L.V. Chulkov, J. Cub, W. Dostal, B. Eberlein, Th.W. Elze, H. Emling, H. Geissel, V.Z. Goldberg, M. Golovkov, A. Grünschloß, M. Hellström, K. Hencken, J. Holeczek, R. Holzmann, B. Jonson, A.A. Korshenninikov, J.V. Kratz, G. Kraus, R. Kulessa, Y. Leifels, A. Leistenschneider, T. Leth, I. Mukha, G. Münzenberg, F. Nickel, T. Nilsson, G. Nyman, B. Petersen, M. Pfützner, A. Richter, K. Riisager, C. Scheidenberger, G. Schrieder, W. Schwab, H. Simon, M.H. Smedberg, M. Steiner, J. Stroth, A. Surowiec, T. Suzuki, O. Tengblad, M.V. Zhukov, Nucl. Phys. A **669**, 51 (2000).
210. C.A. Bertulani, H. Sagawa, Nucl. Phys. A **588**, 667 (1995).
211. J. Jänecke, T. Annakkage, G.P.A. Berg, B.A. Brown, J.A. Brown, G. Crawley, S. Danczyk, M. Fujiwara, D.J. Mercer, K. Pham, D.A. Roberts, J. Stasko, J.S. Winfield, G.H. Yoo, Phys. Rev C **54**, 1070 (1996).
212. T. Nakamura, T. Aumann, D. Bazin, Y. Blumenfeld, B.A. Brown, J.A. Caggiano, R. Clement, T. Glasmacher, P.A. Lofy, A. Navin, B. Pritychenko, B.M. Sherrill, J. Yurkon, Phys. Lett. B **493**, 209 (2000).
213. A. Lagoyannis, F. Auger, A. Musumarra, N. Alamanos, E.C. Pollacco, A. Pakou, Y. Blumenfeld, F. Braga, M. La Commara, A. Drouart, G. Fioni, A. Gillibert, E. Khan, V. Lapoux, W. Mittig, S. Ottini-Hustache, D. Pierroutsakou, M. Romoli, P. Roussel-Chomaz, M. Sandoli, D. Santonocito, J.A. Scarpaci, J.L. Sida, T. Suomijärvi, S. Karataglidis, K. Amos, Phys. Lett. B **518**, 27 (2001).
214. T. Kikuchi, T. Motobayashi, N. Iwasa, Y. Ando, M. Kurokawa, S. Moriya, H. Murakami, T. Nishio, J. Ruan (Gen), S. Shirato, S. Shimoura, T. Uchibori, Y. Yanagisawa, T. Kubo, H. Sakurai, T. Teranishi, Y. Watanabe, M. Ishihara, M. Hirai, T. Nakamura, S. Kubono, M. Gai, f, R. France, K.I. Hahn, Th. Delbar, P. Lipnik, C. Michotte, Phys. Lett. B **391**, 261 (1997).
215. B. Davids, D.W. Anthony, T. Aumann, Sam. M. Austin, T. Baumann, R.R.C. Clement, C.N. Davids, H. Esbensen, P.A. Lofy, T. Nakamura, B.M. Sherrill, J. Yurkon, Phys. Rev. Lett. **86**, 2750 (2001).
216. F. Schümann, F. Hammache, S. Typel, F. Uhlig, K. Sümmerer, I. Böttcher, D. Cortina, A. Förster, M. Gai, H. Geissel, U. Greife, N. Iwasa, P. Koczo, B. Kohlmeyer, R. Kulessa, H. Kumagai, N. Kurz, M. Menzel, T. Motobayashi, H. Oeschler, A. Ozawa, M. Posko, W. Prokopowicz, E. Schwab, P. Senger, F. Strieder, C. Sturm, Zhi-Yu Sun, G. Surówka, A. Wagner, W. Walus, Phys. Rev. Lett. **90**, 232501 (2003).
217. A.R. Junghans, E.C. Mohrmann, K.A. Snover, T.D. Steiger, E.G. Adelberger, J.M. Casandjian, H.E. Swanson, L. Buchmann, S.H. Park, A. Zyuzin, Phys. Rev. Lett. **88**, 041101 (2002).
218. K. Sümmerer, private communication.
219. F. Käppeler, F.-K. Thielemann, M. Wiescher, Annu. Rev. Nucl. Part. Sci. **48**, 175 (1998).
220. S. Goriely, Phys. Lett. B **436**, 10 (1998).
221. M. Wiescher, J. Görres, H. Schatz, J. Phys. G **25**, R133 (1999).
222. V. Efros, W. Balogh, H. Herndl, R. Hofinger, H. Oberhummer, Z. Phys. A **355**, 101 (1996).
223. H. Herndl, R. Hofinger, J. Jank, H. Oberhummer, J. Görres, M. Wiescher, F.-K. Thielemann, B.A. Brown, Phys. Rev. C **60**, 064614 (1999).
224. H. Beer, M. Wiescher, F. Käppeler, J. Görres, P.E. Koehler, Astrophys. J. **387**, 258 (1992).
225. Á. Horváth , J. Weiner, A. Galonsky, F. Deák, Y. Higurashi, K. Ieki, Y. Iwata, Á. Kiss, J.J. Kolata, Z. Seres, J. von Schwarzenberg, H. Schelin, S. Takeuchi, S. Typel, R.E. Warner, Astrophys. J. **570**, 926 (2002).
226. A. Mengoni, *Proceedings of the 2nd Japan-Italy Joint Symposium '95 on Perspectives in Heavy Ion Physics*, edited by M. Ishihara, T. Fukuda, C. Signorini (World Scientific, Singapore, 1995) p. 336.
227. A. Mengoni, private communication.
228. P. Descouvemont, Nucl. Phys. A **675**, 559 (2000).
229. T. Nakamura, N. Fukuda, N. Aoi, H. Iwasaki, T. Kobayashi, T. Kubo, A. Mengoni, M. Notani, H. Otsu, H. Sakurai, S. Shimoura, T. Teranishi, Y.X. Watanabe, K. Yoneda, M. Ishihara, Nucl. Phys. A **722**, 301c (2003).
230. J. Görres, H. Herndl, I.J. Thompson, M. Wiescher, Phys. Rev. **52**, 2231 (1995).
231. M. Terasawa, K. Sumiyoshi, T. Kajino, G.J. Mathews, I. Tanihata, Astrophys. J. **562**, 470 (2001).
232. H. Oberhummer, private communication.
233. Letter of Intent of the R3B collaboration, `http://www-land.gsi.de/r3b/`.